Implementation of new reaction pathway determining methods and study of solvent effects on the excited state nature of perylene based dyes

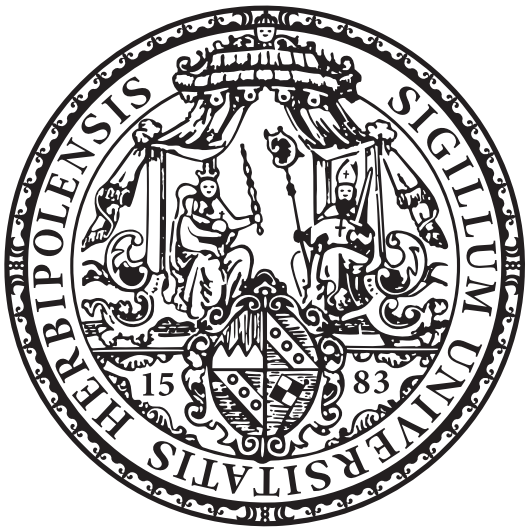

Dissertation zur Erlangung

des naturwissenschaftlichen Doktorgrades

der Julius-Maximilians-Universität Würzburg

vorgelegt von

Daniel Bellinger

aus Lauterbach

Würzburg 2016

Eingereicht bei der Fakultät für Chemie und Pharmazie am

_____

Gutachter der schriftlichen Arbeit

1. Gutachter: _____
2. Gutachter: _____

Prüfer des öffentlichen Promotionskolloquiums

1. Prüfer:_____
2. Prüfer:_____
3. Prüfer:_____

Datum des öffentlichen Promotionskolloquiums

_____

Doktorurkunde ausgehändigt am

_____

Contents

1 Abbreviations **4**

2 Aim of the work **7**

3 Introduction to reaction pathway methods **9**

3.1 Reaction pathways - concepts 9

4 Theory of reaction pathway methods and implementation into CAST **11**

4.1 Nudged elastic band (NEB) methods 11

4.1.1 The standard NEB method 12

4.1.2 The climbing image NEB 12

4.1.3 Doubly nudged elastic band (DNEB) 14

4.1.4 Temperature dependent NEB - description and implementation . . . 15

4.1.5 Image dependent pair potential (IDPP) NEB 25

5 Implementation of new strategies for reaction pathway determination **28**

5.1 Improvements of Pathopt 28

5.1.1 The PO scheme 28

5.1.2 Example calculations 39

5.1.3 Sampling strategies and perpendicular sampling - the tridecaalanine . 59

6 Testing of AMOEBA09 polarizable force field gradients with short-range correction **66**

6.1 Implementation of analytical Spackman gradients 66

6.2 Calculations on benzene dimer and clusters 69

6.2.1 Results on small clusters 69

6.2.2 Benzene dimer calculations with respect to PBE/CCSD(T) dimer . . 78

6.2.3 Global optimization of the cluster dimer configuration 81

6.2.4 Summary 82

7 Study on the flexibility of cyclic PBI derivatives with respect to AFM microscopy - the structure property relationship 83

8 Effects of the environment on photo-physical processes in perylene dyes 92
8.1 Description of environmental effects on excited states 92
8.1.1 The standard polarizable continuum model (PCM) approaches 93
8.2 Excited state properties of PBI and PTCDA with respect to the role of the surrounding 97
8.2.1 Introduction 97
8.2.2 PBI 101
8.2.3 PTCDA 108
8.2.4 Summary 133

9 Summary 134
9.1 Zusammenfassung 136

10 Acknowledgment 139

11 Appendix and References 140
11.1 Appendix 140

Chapter 1

Abbreviations

AA	All Atom
AFM	Atomic Force Microscopy
ADC(2)	Algebraic Diagrammatic Construction of 2^{nd} order
AM1	Austin Model 1
AMOEBA	Atomic Multipole Optimized Energetics for Biomolecular Applications
ASC	Apparent Surface Charges
B3LYP	Becke 3 Parameters Lee-Yang-Parr
BLYP	Becke Lee-Yang-Parr
CAST	Conformational Analysis and Search Tool
CC2	approximate Coupled Cluster singles and double model
CI	Climbing Image
COSMO	Conductor like Screening Model
CT	Charge Transfer
DFT	Density Functional Theory
DNEB	Doubly Nudged Elastic Band
DPS	Discrete Path Sampling
FC	Franck-Condon
FF	Force Field
GO	Global Optimization
GOTS	Gradient based Tabu Search
HF	Hartree Fock
IDPP	Image Dependent Pair Potential
IEFPCM	Integral Equation Formalism Polarizable Continuum Model
IRC	Intrinsic Reaction Coordinate
MCM	Monte Carlo with Minimization
MD	Molecular Dynamics
MEP	Minimum Energy Pathway
MHGP	Metaheuristic Geometrical Perturbation
MO	Molecular Orbital
NEB	Nudged Elastic Band

NTO	Natural Transition Orbital
OPLS-AA	Optimized Potential for Liquid Simulations
PBI	Perylene bisimide
PCA	Principal Component Analysis
PL	Photoluminescence
PCM	Polarizable Continuum Model
PM X	Parametric Model X
PO	Pathopt
PES	Potential Energy Surface
PEC	Potential Energy Curve
PTCDA	Perylene-3,4,9,10-tetracarboxylic dianhydride
QM/MM	Quantum Mechanics / Molecular Mechanics
RMSD	Root Mean Square Deviation
RP	Reaction Pathway
SAPT	Symmetry Adapted Perturbation Theory
SCS	Spin Component Scaling
TD	Time-Dependent
TPS	Transition Path Sampling
TS	Transition State

Chapter 2

Aim of the work

In this work two different topics have been investigated. The first topic comprises the implementation of new reaction pathway determining methods and the testing of existing ones is in the focus. In the second part the treatment of solvent effects on the nature of the excited states of perylene based dyes has been analyzed using state of the art quantum chemical methods.
The work in part one is founded on the beginning studies and implementations of the Pathopt (PO) algorithm within the PhD thesis of Christoph Grebner[1]. It is based on the idea to perform a global optimization with constraints to obtain a network of reaction pathways for a transition between two well defined structures. This was realized by using a constrained optimization strategy based on the Monte Carlo with minimization approach (MCM)[2]. The first test and implementation was based on an optimization starting from one defined structure at the midst between two reactants on a so called "n-1-dimensional" hyperplane which is defined due to the constrained MCM procedure. The construction of the complete pathway was done in an half-automated way. Therefore, within this thesis the automation of the procedure is implemented by using different strategies and evaluate the most fruitful one. In this manner, the optimization on multiple hyperplanes and new automated connection strategies are presented and compared with the first connection strategy. Besides the implementation of the automated routines the testing stands in the focus and was an essential part to evaluate different strategies with respect to the treated systems. Related to this point the implementation of the nudged elastic band (NEB) method was improved and additional features were included like temperature dependent NEB[3] and improved initial guesses for the NEB pathway are made with respect to the image dependent pair potential (IDPP)[4] approach. Besides this main project further side projects in terms of implementation into

the CAST (conformational analysis and search tool) program have been realized. These side projects are the implementation of the gradients of the AMOEBA force field (FF)[5, 6] and improvements related to the Spackman correction for short-range electrostatics. Also the implementation of a principal component analysis (PCA) and an alignment procedure based on the Kabsch algorithm was realized within the bachelor work of Dustin Kaiser[7].
The second part of the work is related to solvent effects on the excited states of perylene based dyes. This work is founded on previous data obtained during my bachelor thesis under the supervision of Volker Settels. The question to deal with was the strength of the influence of a polarizable surrounding on the dimer states of an perylene based dye, like PBI (perylene bisimide) or PTCDA (perylene-3,4,9,10-tetracarboxylic dianhydride). Therefore, we extended our studies for the PBI molecule on explicit solvation as well as implicit solvation by applying different quantum mechanical approaches. Also we included structural relaxation processes to clarify the role of the solvent on the relative position of the excited states. Related to this, it should be mentioned that the energetic order of Frenkel and charge transfer (CT) states is highly discussed in literature and the role of the surrounding is not fully determined. For the PTCDA molecule we also extend our studies and included a QM/MM treatment of the dimer in the field of different cells of the α-PTCDA crystal environment. Besides this we also go further and began to treat larger systems in different configurations as well.

Chapter 3

Introduction to reaction pathway methods

3.1 Reaction pathways - concepts

The understanding of chemistry and ongoing processes is deeply connected to the concept of Potential Energy Surfaces (PES). Therefore, various approaches have been developed in the past decades for the exploration of the PES. Global Optimization (GO) techniques seem to be more and more important, but also local approaches and their investigation schemes are widely used and help to understand chemistry. In the case of GO a wide range of systems are in the focus like clusters, small molecules and even large bio-molecules.[8] One system of interest is e.g the optimization of water clusters due to their important role in biochemistry[9, 10]. Another example is the treatment of subnanonallays by using state of the art GO techniques.[11] Besides the description and analysis of the PES also surface transforming techniques are of great interest in this field.[12]
One part related to explorations of the PES is the investigation of reactions. On the one side reactions can be very simple and a local approach might be quite sufficient. On the other side often the system of interest is more complex and e.g. side reactions or concurring reactions occur or even no product states are known.[13, 14] In consequence, the description of the reactions and kinetics becomes more complex and is not figured out by using one reaction pathway (RP). Therefore, various approaches have been developed in this field. For simple cases, whereas the user might has a prior knowledge about the transition state (TS) local approaches like eigenvector following[15] or the dimer approach[16] are sufficient. These methods belong to the branch of single-ended or surface walking methods and deliver only one

TS structure. Indeed, for larger systems with many degrees of freedom they might be not the best choice and can be computationally very demanding, especially if the second derivative matrix (Hessian) has to be calculated directly. For the dimer method this can be circumvent, because the Hessian is approximated. If no a prior knowledge about the TS is accessible chain of states methods [17] are more recommended. The nudged elastic band (NEB) approach belongs to this class of methods and stands for one possibility of its various adaptations and improvements.[18, 19, 3, 4] The String methods like the growing string[20, 21] variant belongs to this class, too. These are only two examples of the various existing methods. For more complex reactions these approaches might be insufficient. If it is the case that different reaction pathways (RPs) exist and the influence on the global kinetics of such side reactions is hard to estimate global search strategies might be recommended. Therefore, this topic is in the focus of many researchers. One of such approaches is Discrete Path Sampling (DPS)[22] from Wales. The DPS method is founded on the principle to use a large database of minima and TSs and calculate rate constants from this data set. The approach uses the linear master equation for Markovian dynamics. Another approach is the Transition Path Sampling (TPS) approach from Bolhuis et al.[23]. The presented approaches mainly make usage of a RP network and uses it to further analyze and estimate global kinetics. The analysis is founded on different strategies, e.g. graph theory. One of the main questions within the studies is to identify the main contributions to the overall reaction kinetics and to estimate the most important pathways. Pathopt (PO) the newly implemented RP finding method tries to deal with this question and identifies the most important RPs.

Chapter 4

Theory of reaction pathway methods and implementation into CAST

4.1 Nudged elastic band (NEB) methods

The nudged elastic band (NEB) method can be a powerful tool for determining the minimum energy pathway (MEP), whereas the NEB approach belongs to the elastic band methods[24, 17]. The NEB calculation starts from two initial structures and is based on the principle to project structures between these two starting points which built the pathway. These projected structures are minimized with respect to a force projection scheme which distinguishes the NEB approach from other ones. The band built up by the projected structures is coupled through spring forces which couples the minimization process of the band and ensures that the projected structures stay equidistant during the minimization. In this way a continuous band is obtained. The force projection is based on the principle that for each projected structure along the pathway the connecting tangent vectors are calculated and used for estimating the force contributions in different directions. Therefore, it is essential to estimate the tangent vectors τ at each optimization step and to recalculate the force projection. In detail this means that the true force related to the derivatives of the potential energy functions is divided into a perpendicular component with respect to the connecting band and a parallel component defined via the spring constants. This process is called "nudging". By not using this projection scheme problems may arise which would result in pathways for example not going through the curved regions around the TS. This causes a relaxation to low energy regions on the PES and is denoted as "corner cutting" in literature. But by using the proper projection scheme within the NEB method such problems can be circumvent. For example

the choice of the spring force is not very sensible and can be adjusted to a wide variety of values by not changing the obtained RP significantly.

4.1.1 The standard NEB method

The reaction pathway in NEB, called band, is built up by discrete structures, as it was mentioned. The band is defined by $N+1$ structures $\{R_0, R_1, ..., R_N\}$, whereas each structure is built up by the same number of atoms i. The start (R_0) and the final structure (R_N) remain unchanged by the optimization process and are the anchor points of the band. The force which acts on the projected structure is the sum of the perpendicular component with respect to the derivative of the potential energy function $\nabla E(R_i^{\perp})$ and the tangential component $F_i^{||}$[25]. So the force F_i on the projected structure is

$$F_i = F_i^{||} - \nabla E(R_i^{\perp}), \tag{4.1.1}$$

whereas the true force (derived from the potential energy function) can be written as:

$$\nabla E(R_i^{\perp}) = \nabla E(R_i) - \nabla E(R_i) \cdot \hat{\tau}_i. \tag{4.1.2}$$

Within these equations E describes the potential energy of the system which is a function of the atomic coordinates. The normalized tangent vector is denoted by $\hat{\tau}_i$, whereas i stands for the projected structure although the calculation is atom wise defined. The force component along the band (tangential) is the spring force and defined as

$$F_i^{||} = k\left(|R_{i+1} - R_i| - |R_i - R_{i-1}|\right)\hat{\tau}_i, \tag{4.1.3}$$

with k the spring constant. The modified force defined in this way can then be used by an optimizer to find the minimum configurations of the band. In our case the L-BFGS[26, 27, 28, 29, 30, 31, 32] optimizer is used.

4.1.2 The climbing image NEB

Various improvements of the standard NEB approach exist. One example is the climbing image (CI)[33] variant which is only a small correction with respect to the standard approach. The information about the MEP is included as well, as the better convergence to the TS. Within the CI calculation the maximum energy image is calculated within the optimization procedure, whereas the calculation is repeated for each step. This projected structure is then

called $i(MAX)$. For this special structure the force acting on it is computed in a modified approach:

$$F_{i(MAX)} = -\nabla E(R_{i(MAX)}) + 2\nabla E(R^{||}_{i(MAX)}). \tag{4.1.4}$$

In detail this equation can be written as:

$$F_{i(MAX)} = -\nabla E(R_{i(MAX)}) + 2\nabla E(R_{i(MAX)}) \cdot \hat{\tau}_{i(MAX)}\hat{\tau}_{i(MAX)}. \tag{4.1.5}$$

Within the CI variant the maximum energy structure is not influenced by the spring forces during the optimization step. The CI is optimized in the way that energy is minimized in the perpendicular direction with respect to the connecting band and maximized along the reaction coordinate (RC). The RC is defined by the other structures in the band. If the whole CI calculation converges then also the TS should be located properly. The costs of the calculation do not increase because the whole band is handled by one instance of the optimizer and only the forces are updated with respect to the identified CI.

Variable spring constants

The identification of the TS or in general the saddle point of first order is important. Furthermore, the definition of the RC around this point is of big interest, too. Therefore the description around the saddlepoint(s) need(s) to be improved. This can be done using more projected structures around the TS or by crowding the structures within this region. An uneven distribution as described can be reached by using different spring constants at different regions of the pathway. Increasing the strength of the springs around the TS region can afford this. Using the fact that there is no direct interference between the artificial forces and the true forces, the pathway will relax to the same MEP. This is related to the so called nudging. Henkelman et al. applied a linear scheme which adopts the spring constants due to the energy of the projected structure.[33] The criterion for the force constant k_i^{var} is set accordingly to the following assignment:

$$k_i^{var} = \begin{cases} k_{max} - \Delta k \left(\dfrac{E_{MAX} - E_i}{E_{MAX} - E_{REF}} \right) \; if \; E_i > E_{REF} \\ k_{max} - \Delta k \; if \; E_i < E_{REF}. \end{cases} \tag{4.1.6}$$

The projected structures energy E_i is meant to be the maximum energy between two adjacent structures which are connected by the spring with the related constant k_i. The maximum

energy value for the complete band is defined as E_{MAX} and in opposite direction, E_{REF} is an energy value which defines the minimum value of the spring constant. By Henkelman et al. this value is chosen as the higher endpoint in terms of energy of the band. This should lead to a nearly symmetric distribution of the projected structures at the endings of the band, also for asymmetric pathways. Due to these rules the spring constants should be linearly scaled beginning at the maximum value k_{max} and ending up at the lower boundary $k_{max} - \Delta k$. It is the normal case that the two neighboring structures with respect to the CI should be symmetrically arranged. Within their test calculations Henkelman et al. were able to show that it is possible to obtain a crowding around the TS. Therefore, the description of the RC is getting better in the TS region.[33]

4.1.3 Doubly nudged elastic band (DNEB)

The doubly nudged elastic band approach (DNEB)[34, 35] deals with the idea to improve the convergence behavior, as well as reduce corner cutting problems by introducing a second gradient projection for image i. The perpendicular force component (gradient) is constructed in the following way:

$$g_i = g_i^{\perp} + \tilde{g}_i^{||} + \tilde{g}_i^{*}, \tag{4.1.7}$$

whereas the additional component $\tilde{g}_i^{*}$ is defined as

$$\tilde{g}_i^{*} = \tilde{g}_i^{\perp} - \left(\tilde{g}_i^{\perp} \cdot \hat{g}_i^{\perp}\right) \hat{g}_i^{\perp}. \tag{4.1.8}$$

Within these equations $\tilde{g}^{\perp}$ is the spring gradient perpendicular to the connecting band and $\tilde{g}^{||}$ the parallel component. For a better understanding the DNEB gradient can be given in terms of forces obtained after the projection of the spring force components

$$F_i^{DNEB} = \tilde{F}_i^{\perp} - \tilde{F}_i^{\perp} \cdot \hat{F}_i \hat{F}_i, \tag{4.1.9}$$

with the spring force component $\tilde{F}_i^{\perp}$ perpendicular to the true force $\hat{F}_i$ component. This representation is similar to the formulation made in Equation 4.1.8. Despite the fact that the usage of the double nudging improves the stability, the convergence to the MEP is influenced in the manner that a fully converged pathway is not obtained. This is related to the fact, that the additional spring component perpendicular to the band $\tilde{F}_i^{\perp}$ does not disappear during the optimization.

4.1.4 Temperature dependent NEB - description and implementation

Within this part a temperature dependent NEB method accordingly to Crehuet and Field and test calculations are presented. The method implemented in CAST is based on the maximization of the flux related to the Smoluchowski equation[36]. The method applies a differential equation and is directly inherited within the NEB algorithm. Starting from the Smoluchowski equation, Berkowitz and co-workers[37] were able to show how the flux j of an optimal reaction path P can be expressed as follows,

$$j_p = \frac{const}{y \int_p exp(\beta U) ds} \tag{4.1.10}$$

whereas along an ideal pathway (which is assumed to exist) all particles will flow and the friction y is constant for all positions. Hereby U is the potential energy and s the position of the particles along the path. The factor β is equal to $1/k_bT$. One way to optimize the flux is the discretization of the integral, $\int_p exp(\beta U) ds$ given in Equation 4.1.10. This can be done using the Euler formalism leading to the function F:

$$F(R_1 ... R_N) = \sum_{i=0}^{N-1} \frac{1}{2} (e^{(\beta U(R_{i+1}))} + e^{(\beta U(R_i))}) \left| R_{i-1} - R_i \right|. \tag{4.1.11}$$

Within this equation, R_i is the coordinates vector of the i-th image along the pathways. N is the total number of images/configurations. Starting from the discrete function, also gradients can be derived numerically. Still instabilities may arise during the optimization due to the presence of the exponential terms. Crehuet and Field[38] present a different approach to circumvent this issue. They start with the differential equation related to the Euler-Lagrange equation for the above mentioned integral (see Equation 4.1.10). Therefore, one obtains the equation of Berkowitz and co-workers in the following form:

$$\kappa \hat{t} + \hat{n}(\nabla \beta U \cdot \hat{t}) - \nabla \beta U = 0. \tag{4.1.12}$$

Within this equation, the gradient along the reaction pathway is defined as $g = \nabla U$ and the curvature of the RP is κ. The tangent and the normal vectors are $\hat{t}$ and $\hat{n}$. In a next step one can split the gradient into its components along and perpendicular to the band $g = g_{||} + g_{\perp}$. The perpendicular component can be described as follows:

$$g_{\perp} = \frac{\kappa}{\beta}\hat{n}. \tag{4.1.13}$$

Using this equation, the transition between steepest descent pathways and finite temperature pathways is obtained. For $T \to 0K$ the equation is equal to $g_{\perp} = 0$. At infinite temperatures the path is straight, because all existing barriers can be overcome. Also κ must be zero, as $\beta \to 0$ and $g_{\perp}$ is not allowed to be singular. This new scheme for the perpendicular gradient component can be easily applied to the existing NEB scheme using the projection scheme. The force component which defines the perpendicular acting part of the NEB forces can be redefined,

$$F_i^{\perp} = g_i^{\perp} - \frac{\kappa}{\beta}\hat{n} \tag{4.1.14}$$

whereas the force acting on the i-th atom is shown. The curvature of the band is defined by,

$$\kappa_i = \frac{arccos(\hat{\tau}_{i-1} \cdot \hat{\tau}_{i+1})}{|R_i - R_{i-1}| + |R_{i+1} - R_i|} \tag{4.1.15}$$

with τ_i the tangential vector along the band.

Implementation and Testing

Accordingly to the NEB implementation the modifications essential for the minimizer have been included in the *neb* class of CAST. This comprises the inclusion of a new gradient function *g_new_maxflux* and a new instance of the optimizer within the function *lbfgs_maxflux*. The temperature settings were used from the standard configuration options for NEB and PO. For testing the capabilities of the temperature dependent NEB approach our standard set of test systems was used. This test set deals with conformational rearrangments of n-pentane, tridecaalanine, $(H_2O)_{20}$ and ubiquitin (UBQ). For the tests the standard method for calculating τ and applying the optimization for 15 NEB structures defining the band were used. The results for the rotational movement of n-pentane are depicted in Figure 4.1.1. The OPLS-AA FF[39, 40, 41, 42] was used. One can clearly see that two subsets of pathway exist within this figure. The pathways for 1000 and 1500 K are clearly different to the pathways at lower temperature.

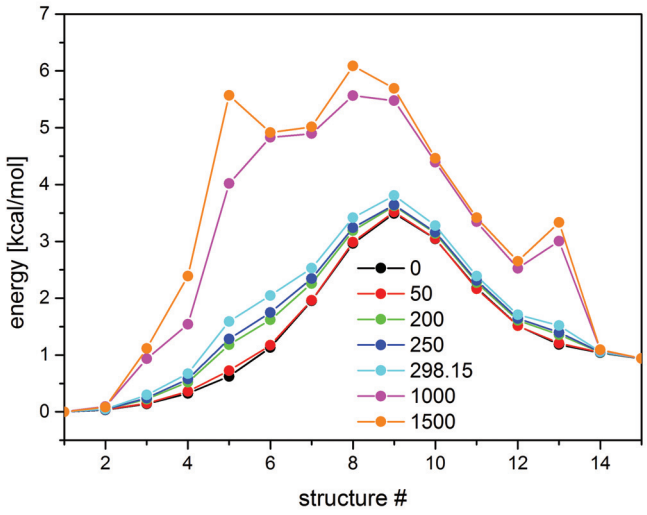

Figure 4.1.1: Temperature dependent reaction pathways for the rotational movement of n-pentane are depicted. The pathways are consisting of 15 structures which define them. The standard OPLS-AA FF was used.

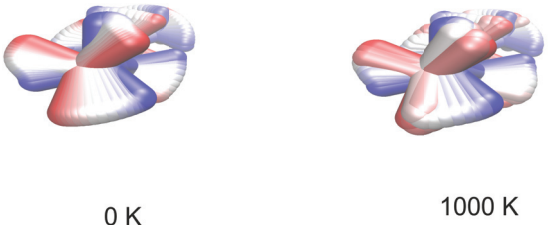

Figure 4.1.2: The rotation of n-pentane around the single bond is shown for 0 and 1000 K. The color-code represents the overlaid motion starting at blue (synklinar) and ending up at the red structure (antiperiplanar).

At 0 and 50 K only one maximum is found for the transition. By slightly increasing the temperature a shoulder is obtained. For the pathway with the highest temperature settings three maxima are obtained which are 3 kcal/mol relatively higher to the barrier found for the lower temperature settings. Therefore, the steps are presented in an overlaid form in Figure 4.1.2. For 0 K a smooth linear transition occurs, whereas for higher temperatures deviations from a smooth rotation are found. One can easily see that at 1000 and 1500 K the pathways are very different that one can state that they might lay above the temperature limit. This

behavior can be visualized by looking at the RMSD (root mean square deviation) change during the rotation for different temperature settings. In Figure 4.1.3 four pathways are depicted. Three of them are distinguishable and one can see that the larger the temperature is, the higher are the deviations to the 0 K pathway and from a "linear"(interpolated) path.

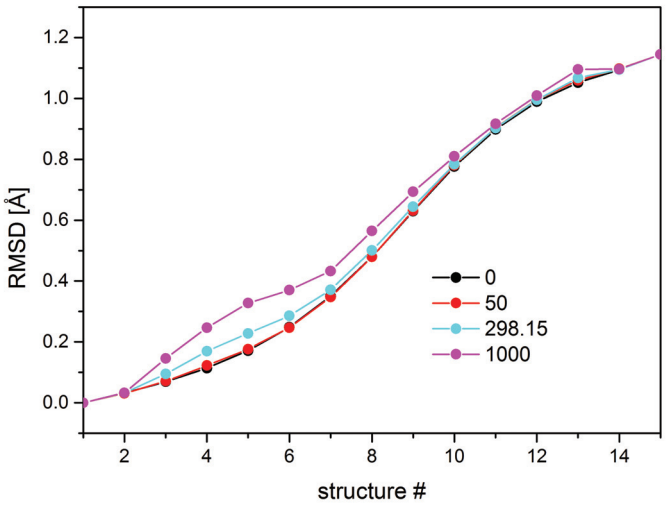

Figure 4.1.3: The RMSD value changes for different temperature dependent pathways (NEB) are shown for the n-pentane rotation.

For the next test system a very similar behavior can be observed. The results for the tridecaalanine transition are given in Figure 4.1.4. The pathways up to 298.15 K show a very similar course and no additional maxima occur. At very high temperatures this changes and for the 1000 K pathways additional features occur, whereas three maxima are obtained. For 1500 K these maxima nearly vanish again and remain only as shoulders from the peak maximum. A similar trend can be found by looking at the transition in the $(H_2O)_{20}$ cluster (see Figure 4.1.5). For the modelled pathway at 0 K and for the lower temperature settings two maxima occur during the transition. By increasing the temperature only on maximum is left. The comparison of the 0 K and 298 K pathway leads to the view that by increasing the temperature up to this point observable differences are visible in the pathways which is also possible to see by looking at the structures building up these ones.

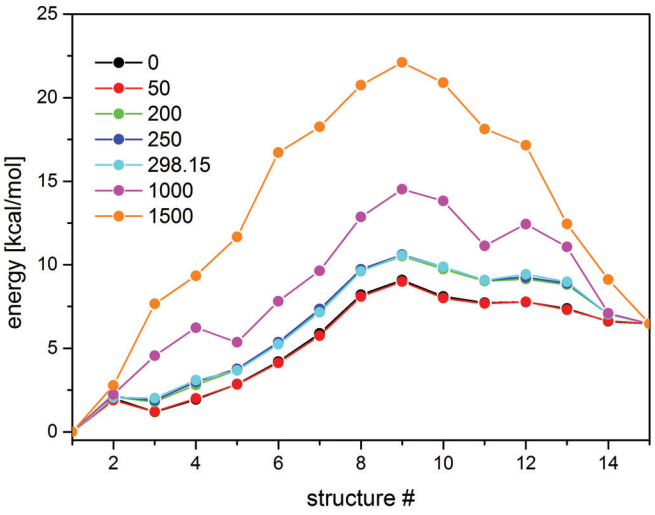

Figure 4.1.4: The temperature dependent NEB pathways of the conformational change between two minima of tridecalanine are shown. The OPLS-AA FF and 15 NEB images were used.

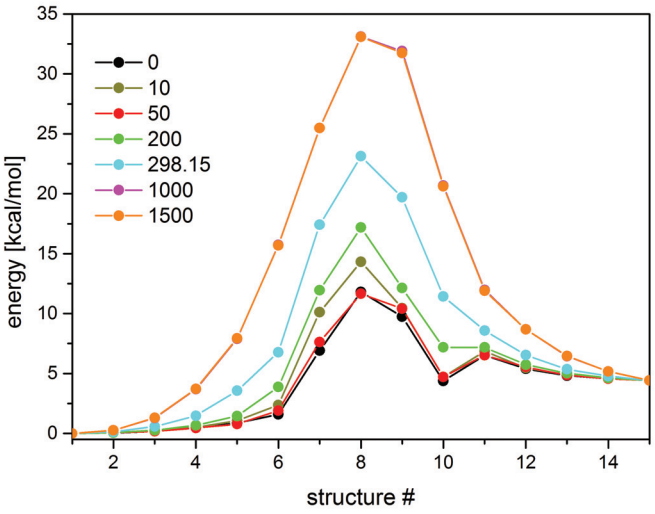

Figure 4.1.5: The temperature dependent NEB pathways are depicted for the cluster transition of a 20 atoms containing water cluster. The transition was described using the OPLS-AA FF and the TIP3P water model.

The RMSD change indicates two different pathways (see Figure 4.1.6). Therefore the

0 K and the 298.15 K pathways are compared. The 298.15 K related RMSD change is observably different from the smooth transition described by the 0 K pathway which can therefore be related to the increase of the barrier for the 298.15 K pathway and by losing the information of the second maximum. The last test system investigated is the UBQ protein (1231 atoms). The results of the temperature dependent NEB calculations are summarized in 4.1.7. In comparison with the other results the changes due to different temperature settings are the smallest. The peak maximum value is only 22% higher for the 1500 K pathway compared with the 0 K one. The peak value differences for the smaller systems are slightly higher ($(H_2O)_{20}$=35%, tridecaalanine=36% and pentane=33%). Besides this fact the obtained pathways are less divergent.

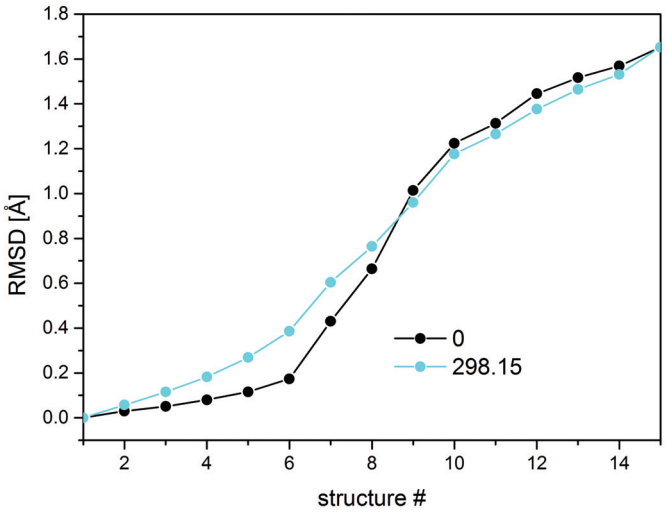

Figure 4.1.6: The RMSD change in Å of two $(H_2O)_{20}$ pathways at two different temperatures is depicted.

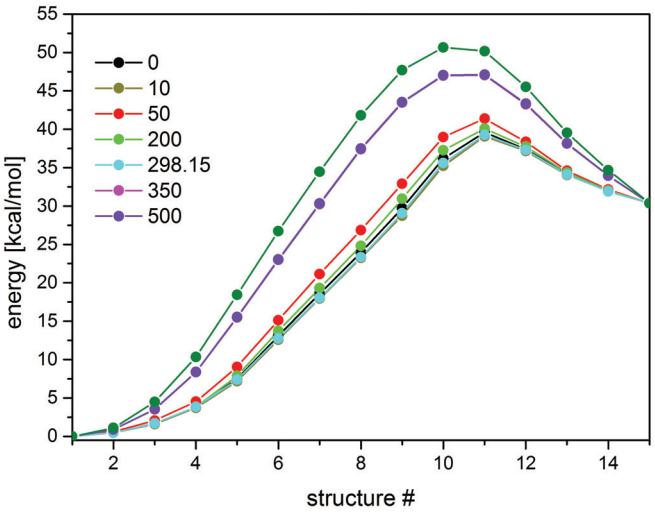

Figure 4.1.7: For the conformational transition of UBQ the temperature dependent NEB pathways are shown, whereas the OPLS-AA FF was used.

For UBQ the increase of the temperature within the NEB simulation leads to a slight downshift in energy compared with the 0 K pathway. This downshift (stabilization) is obtained for 298.15 K as well as for the 10 K temperature conditions. For 50 and 200 K a slight up shift (destabilization) occurred (see Figure 4.1.8). For the simulation of the water cluster and the pentane rotation the trends in shifts show, in the same manner, a continuous behavior for increasing temperatures. For pentane this is illustrated in Figure 4.1.9. As a consequence from these results it might be stated that due to the increasing number of degrees of freedom for the UBQ system the number of accessible minima around a "first guess path" obtained with standard NEB increases. So, the number of possible reaction pathways might also be larger. Therefore, it can be concluded that for different values of the flux additional pathways might occur. Nevertheless, the form of the barrier (parabolic) does not change much and only a single transition is obtained. Also the energy differences are not significant within a reasonable temperature range.

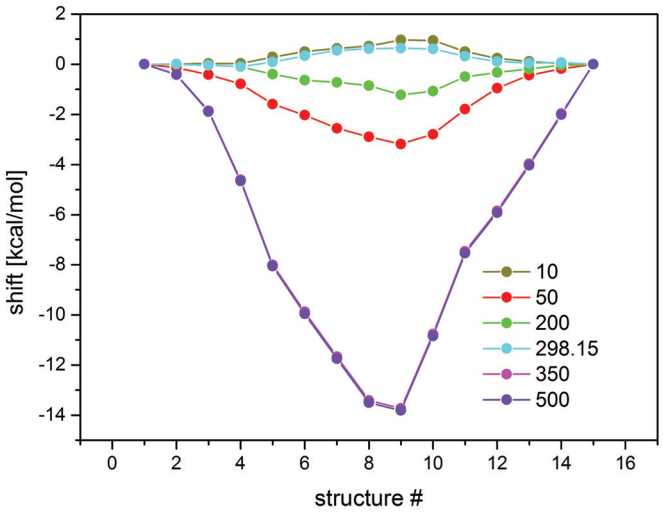

Figure 4.1.8: Relative energy shift in kcal/mol with respect to 0 K NEB pathway for the conformational transition of UBQ is given. Negative shifts indicating a destabilization.

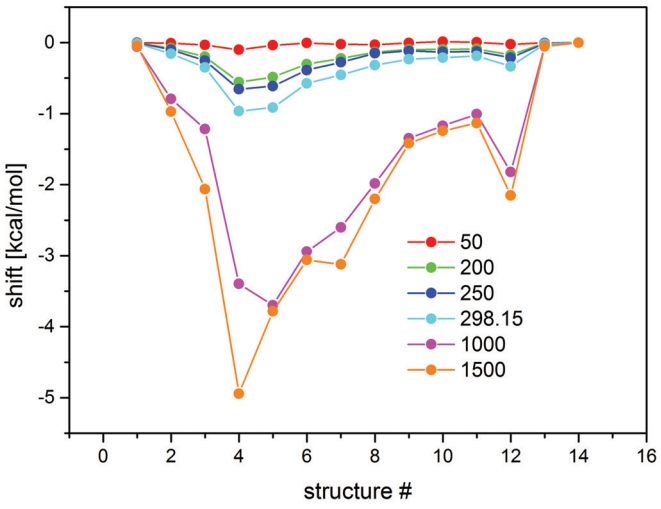

Figure 4.1.9: Relative energy shift in kcal/mol with respect to 0 K NEB pathway for the conformational transition of pentane is given. Negative shifts indicating a destabilization.

To prove this statement one might have a closer look on the differences in the reaction progress at different temperatures. If one computes the total RMSD change for the whole

system, the differences in energy cannot be explained by these terms. Only differences between the high temperature paths and the lower ones are sufficiently large. Therefore, a more thorough full analysis is needed in this context. One way to do this is to divide the analysis in subsystems in terms of an RMSD change visualization. Indeed, for the UBQ system and for atom indices 100 to 200 slight differences between the 0, 200 and 298.15 K paths are obtained (see 4.1.10). But the differences are small and give only limited insight. Therefore, the analysis of bonds, angles and dihedrals which change the most might unleash more details.

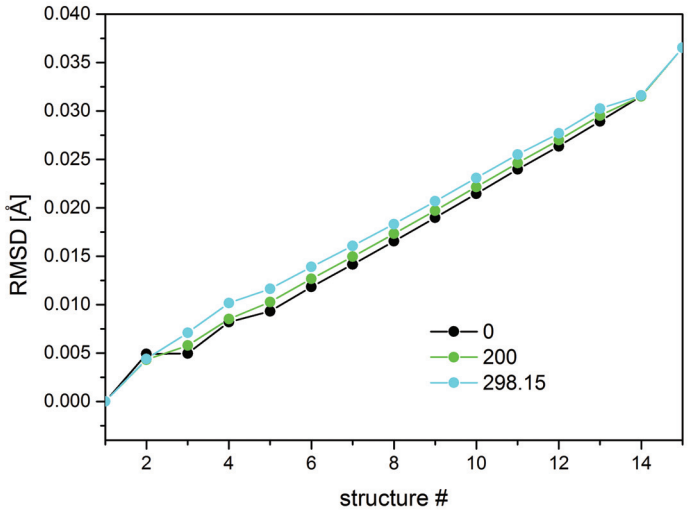

Figure 4.1.10: The RMSD value changes for the UBQ transition are depicted for different temperatures. For the calculations of the RMSD values the index range was set to: 100 to 200.

For this purpose the change of the C-C-O angle built up the indices 378, 379 and 381 was chosen. Compared to other angles the changes during the reaction are a bit larger and differences are better observable. The results for different temperature settings are given in Figure 4.1.11. The presented selection of the UBQ test system and the selected angles are exemplary and additionally other dihedral and angle might be useful to illustrate the differences for various temperature settings. In summary one can say that for the large systems the reduction of the whole process in terms of a RMSD value change is limited and differently chosen reaction coordinates might improve the insight. This closer look for the UBQ systems indeed reveals that for different applied temperatures, with the flux method, more pathways are reached and are accessible.

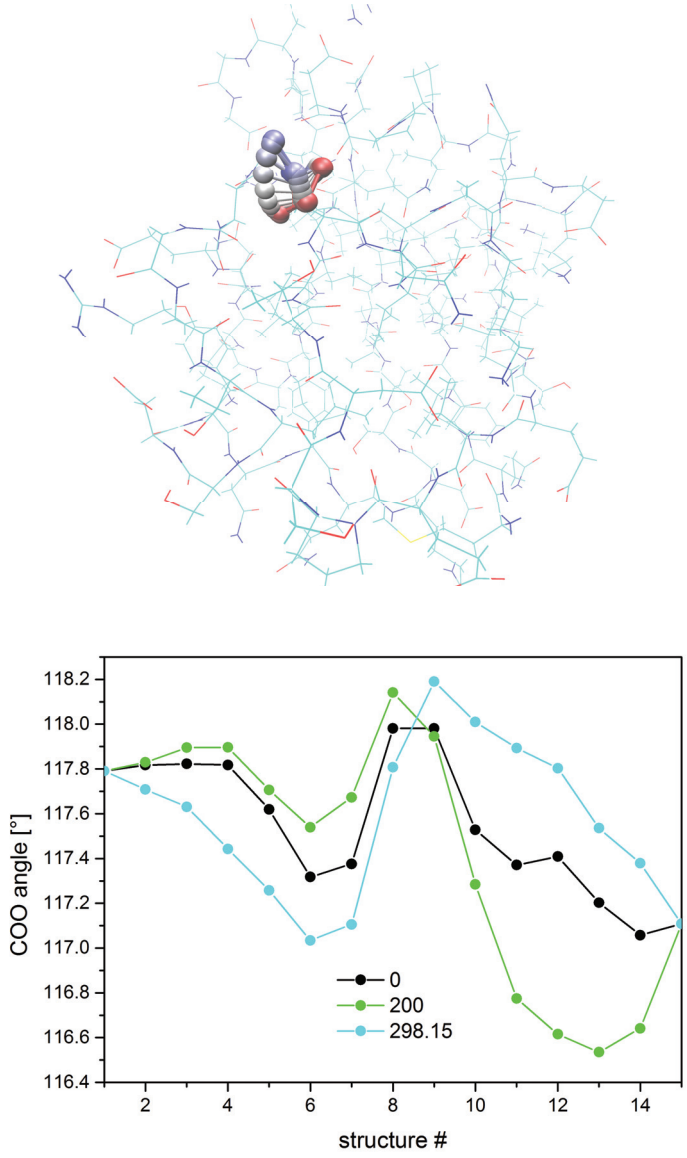

Figure 4.1.11: top: A twisting COO group (indices: 378, 379 and 381) within UBQ is highlighted which changes significantly during the transition between the two minimum structures treated by NEB. bottom: The change of the angle during the reaction of one COO group (378, 379 and 381) which is highlighted on top is given. The change is illustrated for different temperature settings.

4.1.5 Image dependent pair potential (IDPP) NEB

One of the first steps within a NEB calculation is the generation of the initial pathway which is built up by $N-2$ intermediate projected structures. Normally, this initial band is built up using a linear interpolation between the two starting minimum structures. Within this approach the interpolated structures can be far from being reasonable in terms of the internal coordinates (bonds, angles and dihedrals). This would produce large forces acting on the concerned atoms and the convergence behavior can getting worse. Therefore, Smidstrup et al.[4] introduced a new method for the calculation of the initial band of projected structures. This method is based on the interpolation of pairwise distances which are calculated for the whole band and additional acting forces which are deduced from these distances. Due to the additional forces the convergence behavior should be improved, but an additional run has to be carried out beforehand. The linearly projected structures (R_i) can be defined via their position vector (r), whereas each structure is built up by N atoms

$$R_i \equiv (r_1, r_2, ..., r_N)^T, \tag{4.1.16}$$

with $r_n = (x_n, y_n, z_n)$ the atom position in Cartesian representation. The discrete points are calculated for the $i-2$ total number of structures and the projected structures are obtained via the following formula:

$$R_n^i = R_n^{start} + \frac{i\left(R_n^{end} - R_n^{start}\right)}{N}, \tag{4.1.17}$$

where R_n^i is the Cartesian atomic coordinate n of the $i-th$ projected structure. R_n^{end} and R_n^{start} are the related end point (start / final) atomic coordinates.
For the definition of the objective function which is minimized to obtain the improved guess in a first step the Euclidean distances d_{nm} (referenced to Cartesian coordinates σ) between two arbitrary atoms n and m should be defined as:

$$\begin{aligned} d_{nm} &= \sqrt{\sum_{\sigma} (r_n - r_m)^2}, \\ &= \sqrt{(x_n - x_m) + (y_n - y_m) + (z_n - z_m)}. \end{aligned}$$

By using $i-2$ projected structures and the *start* and *end* structure, the interpolated distances between atom n and m at structure i are given as

$$\begin{aligned} d_{nm}^{i} &= d_{nm}^{start} + \frac{i\left(d_{nm}^{end} - d_{nm}^{start}\right)}{N}, \\ &= \sqrt{\sum_{\sigma}\left(r_n - r_m\right)^2} \\ &+ \frac{i}{N}\left(\sqrt{\sum_{\sigma}\left(r_n - r_m\right)^2}^{end} - \sqrt{\sum_{\sigma}\left(r_n - r_m\right)^2}^{start}\right). \end{aligned} \tag{4.1.19}$$

For finding the improved pathway the objective function for a projected structure can be defined as follows:

$$\begin{aligned} S_i^{IDPP}(r) &= \sum_{n}^{N}\sum_{n>m}^{N}\omega(d_{nm})\left(d_{nm}^{i} - \sqrt{\sum_{\sigma}\left(r_n - r_m\right)^2}\right)^2, \\ &= \sum_{n}^{N}\sum_{n>m}^{N}\frac{1}{d_{nm}^4}\left(d_{nm}^{i} - \sqrt{\left(x_n - x_m\right)^2 + \left(y_n - y_m\right)^2 + \left(z_n - z_m\right)^2}\right)^2, \\ &= \sum_{n}^{N}\sum_{n>m}^{N}\frac{\left(d_{nm}^{i} - d_{nm}\right)^2}{d_{nm}^4}, \\ &= \frac{1}{2}\sum_{n}^{N}\sum_{m}^{N}\frac{\left(d_{nm}^{i} - d_{nm}\right)^2}{d_{nm}^4}. \end{aligned} \tag{4.1.20}$$

Therefore, the objective function $S_i^{IDPP}(r)$ can be described as the square deviation of the interpolated distances d_{nm}^{i} with respect to the Euclidean distances d_{nm}. So it acts like the pairwise potential that is related to an effective energy surface. This function is then applied to the NEB method for finding the optimal initial pathway. The function $\omega(d_{nm}) = 1/d_{nm}^4$ is a weight function which takes into account that shorter distances within the overall description stronger contribute. The resulting force acting on atom n in structure i can be assigned to

$$
\begin{aligned}
F_n^i(r) &= -\nabla_n S_i^{IDPP}, \\
&= -\begin{pmatrix} \frac{\partial}{\partial x_n} \\ \frac{\partial}{\partial y_n} \\ \frac{\partial}{\partial z_n} \end{pmatrix} \sum_n^N \sum_{n>m}^N \frac{1}{d_{nm}^4} \left(d_{nm}^i - \sqrt{(x_n - x_m)^2 + (y_n - y_m)^2 + (z_n - z_m)^2} \right)^2 .
\end{aligned}
\tag{4.1.21}
$$

The force on atom n in the projected structure i can be written as the sum of all forces derived from IDPP along the bonds n, m, whereas $n \neq m$ and $n \in \{1, ..., N\}$:

$$
\begin{aligned}
F_n^i(r) &= \sum_{n \neq m}^N \left[\frac{\mathbf{d_{nm}}}{d_{nm}} \frac{\partial}{\partial d_{nm}} \left(\frac{\left(d_{nm}^i - d_{nm}\right)^2}{d_{nm}^4} \right) \right], \\
&= -2 \sum_{n \neq m}^N \left[\frac{\mathbf{d_{nm}}}{d_{nm}} \left(\frac{\left(d_{nm}^i - 2d_{nm}\right)\left(d_{nm}^i - d_{nm}\right)}{d_{nm}^5} \right) \right].
\end{aligned}
\tag{4.1.22}
$$

within this equation the $\mathbf{d_{nm}}$ is the given vector for an atom pair nm. By describing the force acting on the projected structure i one obtains the following:

$$
\begin{aligned}
F^i(r) &= \sum_{n=1}^N F_n^i(r), \\
&= -2 \sum_n^N \sum_{n \neq m}^N \left[\frac{\mathbf{d_{nm}}}{d_{nm}} \left(\frac{\left(d_{nm}^i - 2d_{nm}\right)\left(d_{nm}^i - d_{nm}\right)}{d_{nm}^5} \right) \right].
\end{aligned}
\tag{4.1.23}
$$

The forces accordingly to Equation 4.1.22 and 4.1.23 can be applied in an optimization procedure within the NEB procedure. This resulting initial pathway should be closer to the real MEP than a linear interpolated one. The implementation into the CAST program was done within a practical course of Michael Prem.

Chapter 5

Implementation of new strategies for reaction pathway determination

5.1 Improvements of Pathopt

The implementation of Pathopt (PO) is founded on a constrained global optimization scheme. PO belongs to the chain of state methods and uses two structures which define the endpoints of the reaction as an input. The first step within the PO procedure is to built up a linear pathway which connects these two structures. The main idea of the algorithm and its first implementation is founded on work of Grebner et al.[43]. The presented implementation in this thesis is describing the improvements and implementation into the current version of the CAST program and also includes further test sets. In the first implementation the linear interpolated structures have been directly used within the global optimization. But tests have shown that already converged structures are more useful. In this manner we applied NEB in a first step to generate the initial pathway. The more detailed description of the NEB method can be found in chapter 4.1. The main idea of PO is to apply a constrained global optimization which will be described in the following.

5.1.1 The PO scheme

In a first step two minimum structures which define the endpoint of the initial pathway are needed. These two structures should be aligned beforehand which is also possible directly with the CAST program. Due to the alignment (Kabsch algorithm [44]) the translations and rotations are excluded. In a next step the NEB calculation is started. Therefore, different

types of NEB approaches can be used to generate the initial path.

NEB options and implementation

The *neb* class and its implementation focuses on that way that it works in principal with all existing energy interfaces (energy methods) available in the CAST program. But it is also designed to work together with the PO class. The main ingredients of the *neb* class are on the one side the standard NEB method from Henkelman and its improved tangents estimate, as well as the climbing image variant. Furthermore, temperature dependent NEB[3] and the improved initial guess for linear pathways based on the image dependent pair potential (IDPP) [4] are included. Further information can be found in the NEB chapter (4.1).

PO implementation

After the successful run of the NEB calculation the *pathx* class is initialized by generating an object of this class which initializes with references to the *coordinates* and the *neb* objects. Both are needed because the *coordinates* object in CAST handles everything related to the actual coordinate set and implemented energy and gradient calculations and within the *neb* object the information related to the starting pathway is included. The main information which is used by the *pathx* class are the starting structures generated within the preprocessed NEB calculation and the information about the connecting tangent vectors τ. The two most important functions within the *pathx* class are *MCM_PO* and *proof_connect*. After initialization of the *pathx* class the calculation starts by calling the *pathx_ini* function. Within this function for each structure, out from the total number of $N-2$ projected structures, the *MCM_PO* function is called for the respective structure. It carries out the constrained search. The starting point of the loop is defined by the first projected structure $i = 1$, whereas $i = 0$ is the input starting structure and the last MCM optimization is called for $i = N - 1$. Beforehand the Cartesian coordinates are updated with respect to the *Coordinates* object. The *MCM_PO* function applies the constrained MCM scheme which will be explained in detail.

MCM scheme

The function *MCM_PO* is based on the implementation of a Metropolis Monte Carlo simulation strategy with applied local optimization step. The two main modifications of the MCM scheme in our case are related to the move steps and the optimization procedure. The implementation of the procedure into the current CAST version is founded on the first

proposed approach by Grebner et al.[43]. In consequence only a short introduction to the basics is given and new features are presented. To realize the constraint the optimization steps are restricted to be perpendicular to the tangent vectors obtained from the initial NEB pathway. For the realization of the constraint two different approaches are implemented, the first one refers to the original idea of applying a projection scheme for the gradients. In fact, that we obtain a global optimization on a $k-1$ dimensional PES ("hyperplane"). The projection scheme of the gradients is described in Figure 5.1.1 on three example hyperplanes. The resulting gradient $\vec{p_i}$ from the projection scheme is perpendicular with respect to the connecting band and defined as,

$$\vec{p_i} = \vec{g}_i - \vec{g}_{i||\vec{\tau}_i} \tag{5.1.1}$$

whereas the parallel gradient component along the tangent is calculated as follows:

$$\vec{g}_{i||\vec{\tau}_i} = \frac{\vec{g}_i \vec{\tau}_i}{|\vec{\tau}_i|^2} \vec{\tau}_i. \tag{5.1.2}$$

In the second option, the constraint is realized through an applied bias potential. This potential is quadratic and applies an additional force component perpendicular to the intervening hyperplanes. For the first method no additional force component is used, whereas for the biased optimization the magnitude of the force constant can have significant influence. Therefore it has to be chosen carefully.

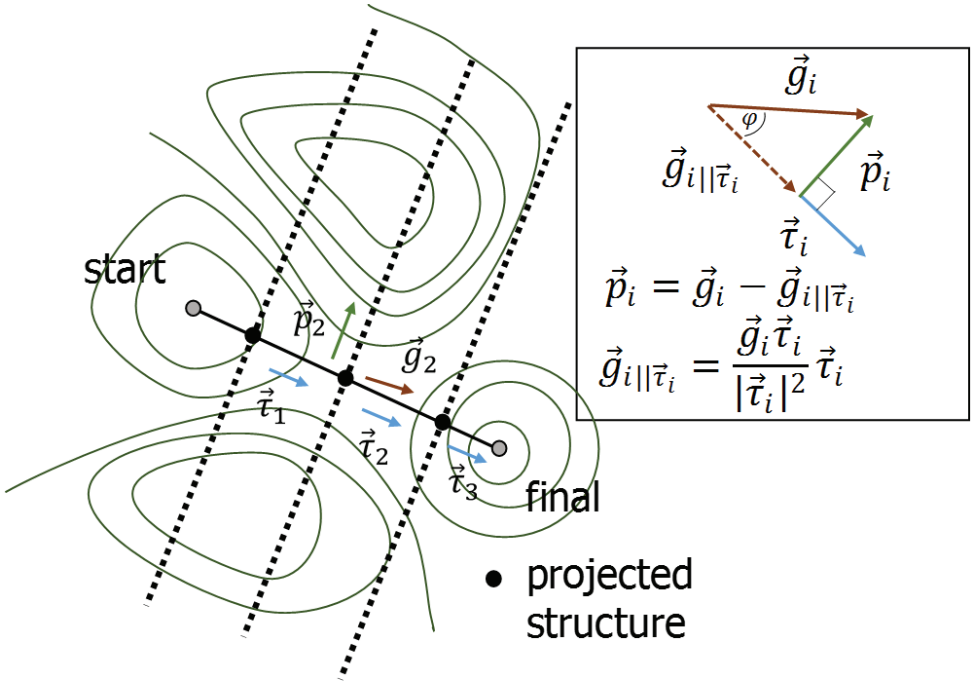

Figure 5.1.1: The schematic representation of the MCM gradient projection within the PO algorithm is shown. Three hyperplanes are shown which were generated for the projected structures. The perpendicular projected gradients $\vec{p}_i$ are shown with respect to the tangent vectors $\vec{\tau}_i$ which define the band.

The gradient modifications are carried out by using a modified instance of the L-BFGS[26, 27, 28, 29, 30, 31, 32] optimizer in CAST. This is realized within the *lbfgs* function. Within this function an object of the lbfgs type is generated which needs a gradient call back function. Normally, the unmodified gradient function is called within the optimization procedure. In this case, the function *g_new* is used instead. Within this function the normal gradient calculation via the energy interfaces is modified by applying either the projection scheme or the bias potential. Besides the modification of the optimization step within the MCM scheme also the random move steps are adopted to fulfill the constraint. The standard move steps are carried out in Cartesian coordinates, whereas the structure is distorted perpendicular with respect to the connecting band. This scheme was already adopted in the first implementation of the algorithm. Within this implementation an additional move type was included. First test calculations showed that a Cartesian move strategy is not sufficient for all cases and would cause longer computations to get all the desired RPs. In fact a new search strategy based on the idea of changing the dihedrals at some point to enhance the diversification of

the search was implemented. In the new strategy the main dihedrals are randomly changed perpendicular with respect to the connecting band defined by the τ vectors. The move step is illustrated in Figure 5.1.2, whereas the change of the dihedrals is carried out at every 10th MCM step (adjustable). This move strategy should be called "mix-move" strategy.

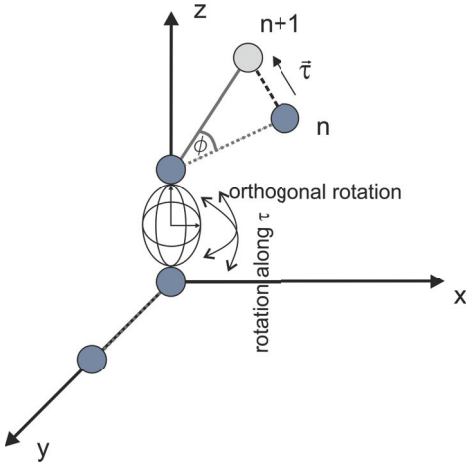

Figure 5.1.2: Schematic illustration of the dihedral move step within the PO routine. The move steps are carried out perpendicular with respect to the connecting band.

After the optimization step the obtained structures are checked if they are lower in energy than the previous one or for satisfying the Metropolis criterion which is given by

$$P_i < e^{-\frac{(E_{ref}-E_i)}{RT}}, \tag{5.1.3}$$

for the actual point. In addition, the structure is checked if reasonable or not and if the displacement(in Å) is within the defined maximum allowed displacement referenced to Cartesian coordinates. The accepted minima are saved with respect to the hyperplane they are related to. Energies and structures are saved in separated files.

Connection schemes

The connection of the structures is carried out after the GO on the $N-2$ total number of hyperplanes to obtain complete RPs. In relation to the first implementation and in doing further tests, within this work, the strategy has been gradually refined.

Old connection strategy

The first proposed connection strategy (see Figure 5.1.3) based on the principle to carry out the constrained MCM only on one hyperplane, as mentioned before. The obtained structures should serve as first guesses for the TS and be refined. This refinement is carried out by using the dimer or the eigenvector following approach.

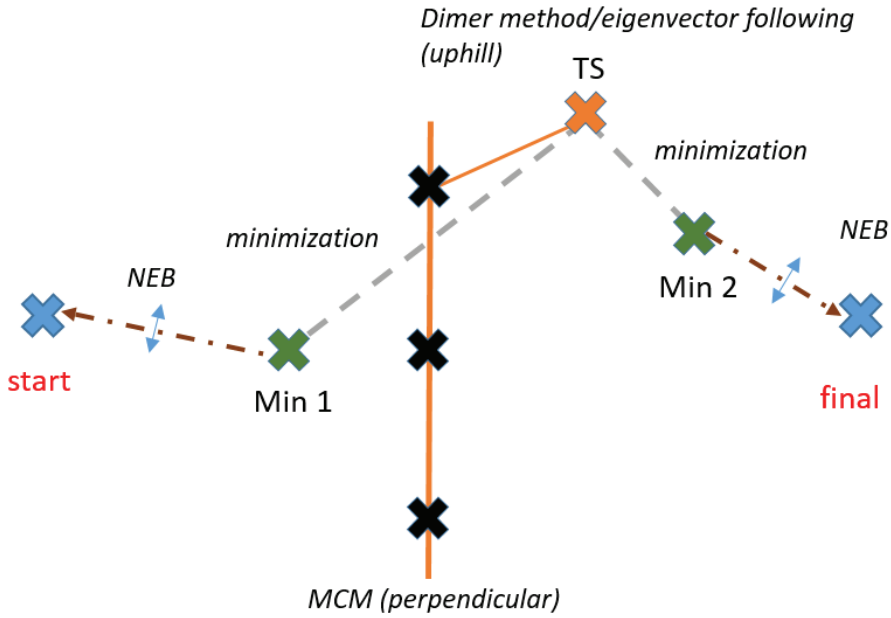

Figure 5.1.3: The representation shows the *old connection strategy* for PO. Within the old approach the MCM search was carried out on one hyperplane. The obtained minima were further refined to obtain TS structures which are then connected with the start and final structure by applying additional PO cycles or NEB calculations.

After optimization to the TS a relaxation step along the first imaginary mode should yield the directly connected minima. The obtained path segments should then serve as starting points for building up complete reaction pathways. For realization of this procedure an interface to the Tinker 5.x/6.x[45, 46, 47, 48, 6] program was implemented. Tinker is used to calculate the Hessian and carry out the relaxation steps along the first imaginary displacement coordinate. The TS optimization was implemented using the dimer approach. The main idea was to obtain an automated procedure for determining complete pathways in CAST. Therefore, the calculation was extended to multiple planes within this scheme. For each global optimization on a hyperplane a TS optimization was carried out and in a next step the vibrate module from the Tinker package is called. From the Tinker calculation it is

possible to extract the structures which are displaced along the first imaginary mode. For testing and locating the structures in relation to the generated hyperplanes the angle between the gradient vector $\vec{g}$ and $\vec{\tau}$ is calculated. In the ideal case this angle is 90°. In addition to proof the angle, the distance D of a structure with respect to the concerning plane was calculated,

$$D = |proj_{\tau} w| \tag{5.1.4}$$

where w is the atomic coordinate vector. The expression can be written in detail,

$$D = \frac{ax + by + cz - ax_0 - by_0 - cz_0}{\sqrt{a^2 + b^2 + c^2}} \tag{5.1.5}$$

with the vectors and the components:

$$\vec{\tau} = \begin{pmatrix} a \\ b \\ c \end{pmatrix}, \vec{w} = \begin{pmatrix} x \\ y \\ z \end{pmatrix}, \vec{i} = \begin{pmatrix} x_0 \\ y_0 \\ z_0 \end{pmatrix} \tag{5.1.6}$$

In our case $\vec{i}$ is the vector of the initial image. The distance is calculated for every atom and then the geometric weighted distance is calculated. This calculation is also used to identify the relative position of the obtained pathsegments with respect to the hyperplanes generated. Test calculations for the *old connection scheme* are presented in the following. In principle, the more planes are created the better the representation of the surface between start and final structure should get. The difference between simulating on three planes is compared with the results for the simulation on 10 planes for the Ar_4 cluster (see Figure 5.1.4). In the depicted diagrams also the side views (slices) are prepared. This side views show the energy landscape on every simulated perpendicular hyperplane.

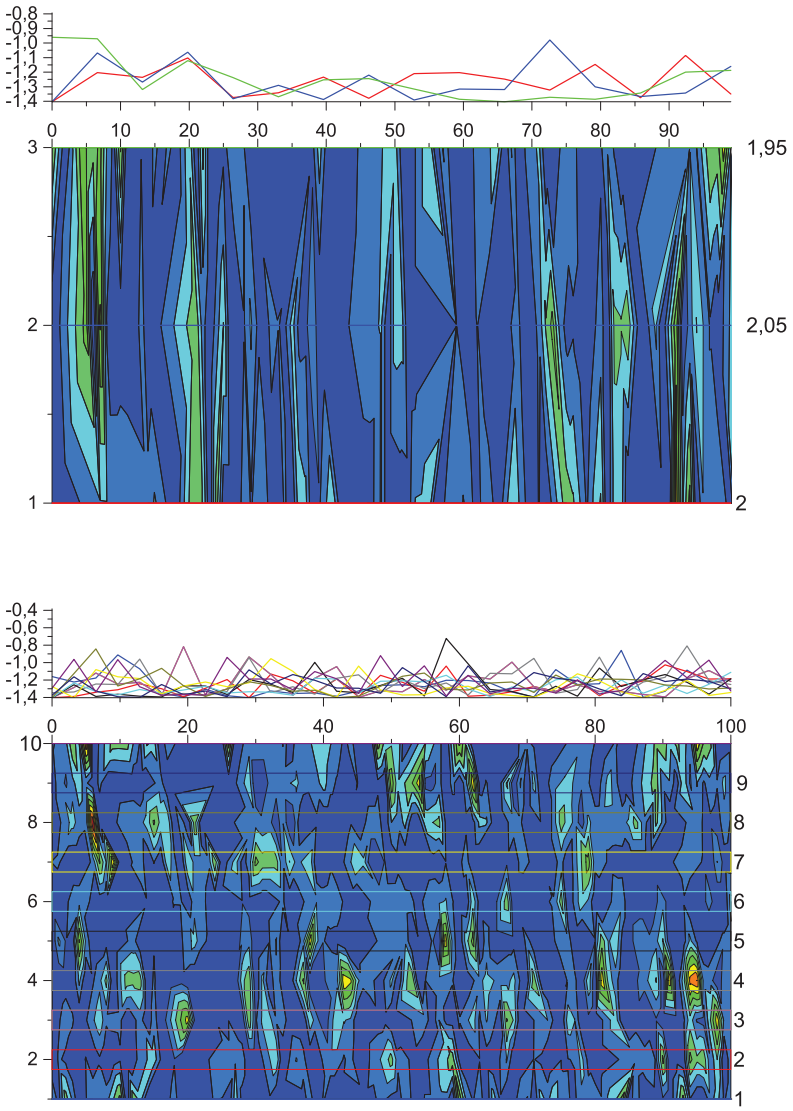

Figure 5.1.4: The inter-sectional paths for the Ar_4 cluster are shown. On top side the results for 3 planes are shown and on the bottom side the 10 plane results. In the upper part of each representation the energies are plotted against the MCM steps.

After obtaining these slices along the surface in a next step the path segments were calculated which are shown in Figure 5.1.5. These path segments can be analyzed for their positions in relation to the created hyperplanes to obtain a better insight. In the case of the Ar_4 cluster all segments found lay close to the first plane which is located near the global minimum. There is also no large difference if the number of hyperplanes is increased up to

three or ten. For larger systems like the Ar_{12} cluster this is quite different.

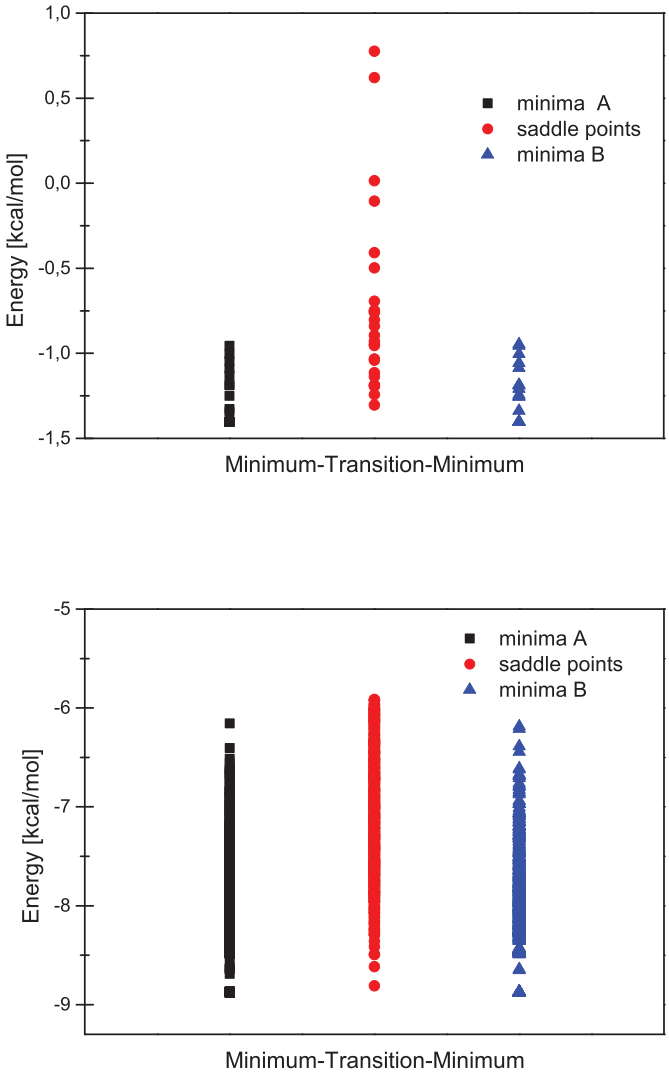

Figure 5.1.5: The path segements within the *old connection scheme* and the concerning energies are shown. On top the Ar_4 and on the bottom the Ar_{12} results are depicted.

The distribution of the minima is getting larger and also the possible number of pathsegments is increased due to larger degrees of freedom. In Figure 5.1.6 the energy distribution for a simulation on 3 hyperplanes is shown for the Ar_{12} cluster. Also the sorting to nearest hyperplane is depicted. In consequence of these first results which are related to the multiple

hyperplane calculations within the *old connection scheme* we were able to show that indeed a constrained optimization can be carried out and path segments can be located according to their relative position with respect to the hyperplanes. Up to this point the methodology of obtaining path segments seems to be a good alternative to increase the number of pathways and improve the description of the transitions or reactions, but already at this point it was getting obvious that a multiple number of TS optimizations and the call of the Tinker program to obtain the relaxed minimum structures would be inefficient for the description of more complex and larger systems or by using more elaborate methods besides Molecular Mechanics. In a next step a new strategy was developed by keeping the multiple hyperplane simulations in mind.

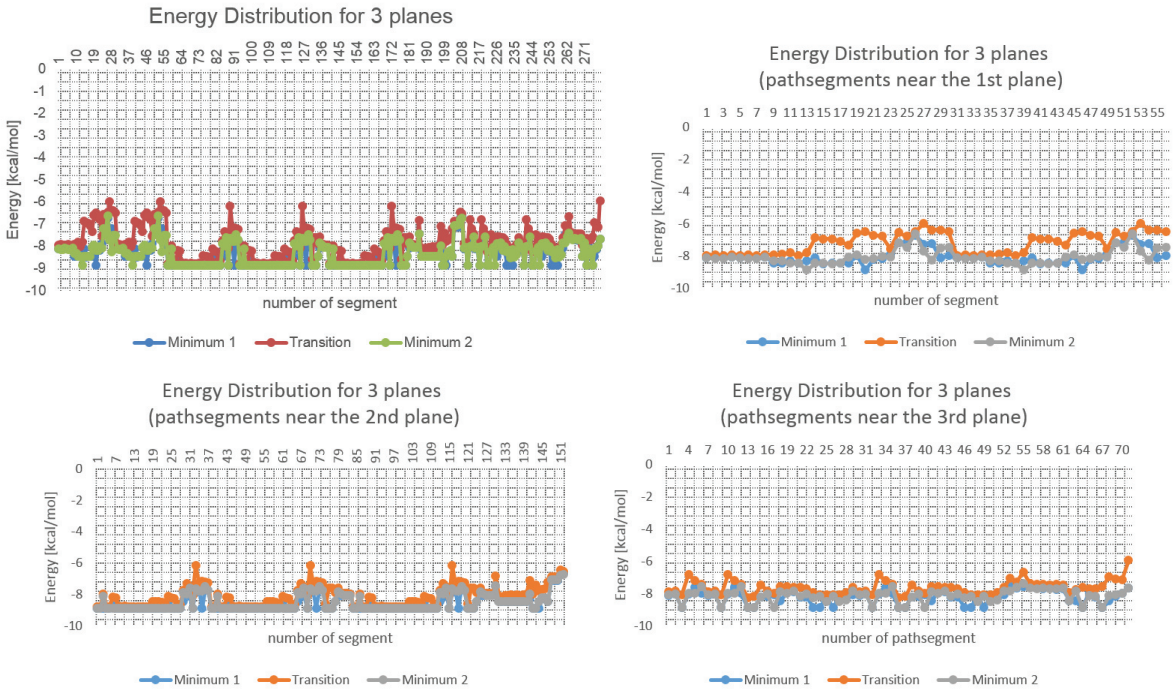

Figure 5.1.6: The energy distribution for different path segments of the Ar_{12} is shown. The first diagram shows the distribution for all segments, in the following representations the results are depicted and sorted due to the position of the minima and transition states related to the constructed hyperplanes.

New connection strategies

As mentioned in the previous section the *old connection scheme* is time consuming and depends on the accuracy of the uphill optimization as well. Within the new scheme the

extension to Tinker is no longer needed and the uphill optimization is also excluded. The minima found on the intervening hyperplanes are directly connected to built the reaction pathways. Therefore, the minima saved within *MCM_PO* are aligned by a center of mass alignment procedure within the function *proof_connect*. In a next step, the RMSD values between the structures of one and the next hyperplane are calculated. From a built list of next nearest neighbors a directly connected pathway is constructed. Besides the next nearest neighbors also the second- and third-nearest partners are connected. The obtained pathways are saved in separated folders. The energies and structures are printed in separated files, whereas also the TS energy is given. This connection scheme is referred as *new I* and is depicted in Figure 5.1.7. Besides this direct connection a possibility exist to interconnect the hyperplanes by using the NEB method. This connection procedure is described in Figure 5.1.8 and is called *new II*.

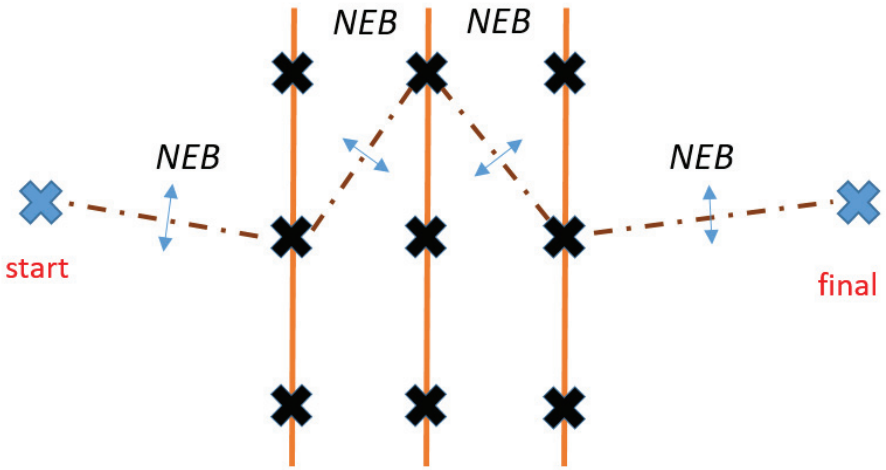

Figure 5.1.7: The connection strategy *new I* is presented. The number of hyperplanes is increased and the found minima on the hyperplanes are directly connected with each other to obtain pathways which connect start and final structure.

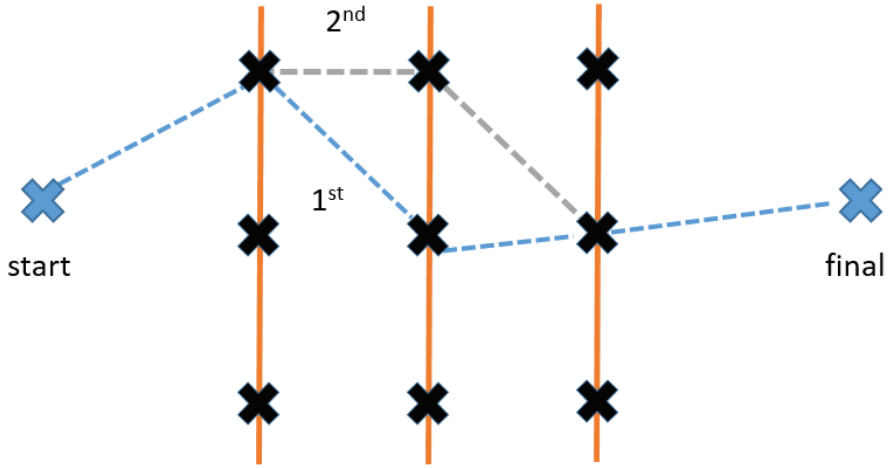

Figure 5.1.8: The connection strategy *new II* is presented. Within this procedure the number of hyperplanes can be increased, as well and the connection between start and final structure or intervening hyperplanes is obtained by carrying out NEB optimizations.

5.1.2 Example calculations

Ar_{38} and $(H_2O)_{20}$

Argon clusters are the ideal test systems for showing the capabilities of new global optimization algorithm. Therefore, they serve as test candidates for this study. As already mentioned in the introductory part small clusters of Argon already have been used for this purpose and were discussed by Grebner et al.[43]. Besides the results of the Ar_{38} cluster the PO results of a water cluster optimization $(H_2O)_{20}$ are discussed within this part. All calculations were carried out with the CAST program except the frequency calculations which were done with the Tinker 6.2[45, 46, 47, 48, 6] program. Both cluster systems were calculated using the OPLS-AA FF[39, 40, 41, 42], whereas the water cluster was investigated applying the TIP3P water model within the FF description. To generate reasonable starting structures a global optimization was carried out for both systems. In both cases a MCM optimization was performed. For the Argon cluster 500 steps at 298.15 K and with a step size in Cartesian space of about 1.4 Å were searched. This was quite sufficient to generate a reasonable amount of starting structures for the PO search. In the case of the water cluster 5000 MCM steps were used. The temperature and step size settings were the same as for the Argon cluster. In all calculations no cutoff radius was applied for the non-bonded interactions. As already mentioned in the introductory part of the PO method the alignment was the first step for all calculations and was carried out by using the method of Kabsch[44] implemented in the

VMD 1.9.1[49] program.

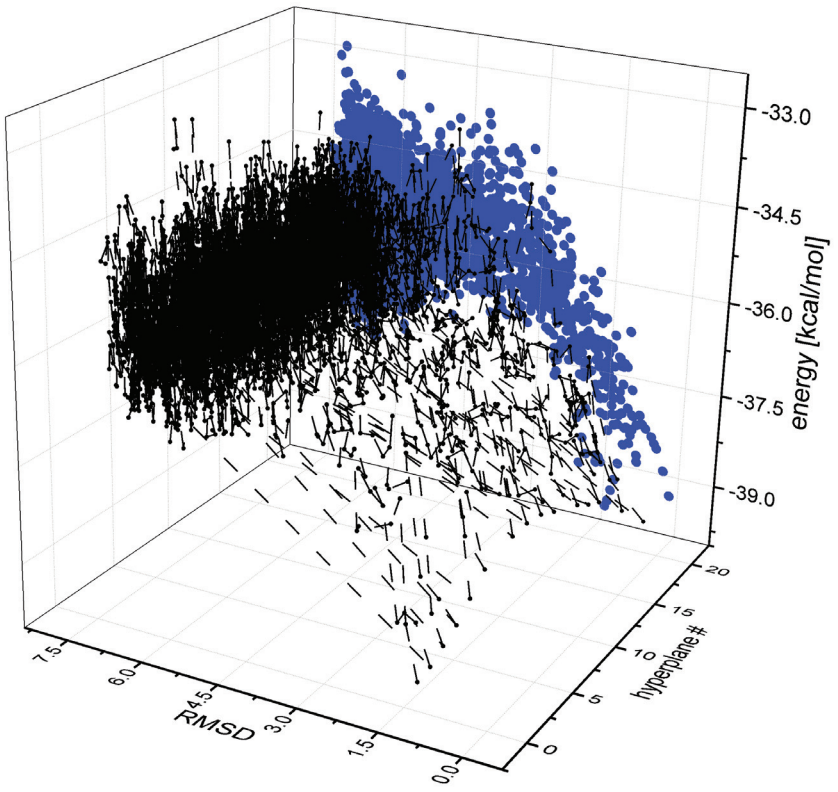

Figure 5.1.9: The minima from a constrained optimization on 20 hyperplanes are depicted. The energies are given in kcal/mol. The RMSD values are shown in Å, referenced to the NEB starting structures.

The Ar_{38} system is an ideal test candidate, because it is a relatively small system but possesses a complex and flat PES with multiple minima. Consequently, this cluster is often used in benchmarking global optimization routines. As a start structure we used the global minimum obtained from our global optimization run. The final structure was randomly chosen. In Figure 5.1.9 the results from a PO run are depicted. The PO simulation was carried out for 20 intervening hyperplanes, whereas 2000 MCM steps were performed on each hyperplane. For this calculation the gradient projection scheme was used. From the presented results one can see that the obtained minima span up a wide range in RMSD values (referenced to the starting structure) and energies. Having a closer look at the energies obtained the question might arise, which minima to choose for building meaningful RPs,

or which pathways contribute the most to the description of the transition between two arrangements. In the automatic connection procedures the RMSD criterion is chosen as one way to obtain meaningful pathways. In addition, the energy of the TS can be used as a criterion as well. So one can use the Arrhenius equation by calculating relative barrier heights compared to the NEB TS. Therefore, the relative effect on the rate constant can be estimated. In this manner, pathways with TS within a range of 2 kcal/mol with respect to the NEB barrier are chosen. Such a TS criterion would result in a lowering of the rate constant by a factor of 7.4, relatively. From this example it can be seen that often only a small number of pathways contribute to the overall description of a reaction.

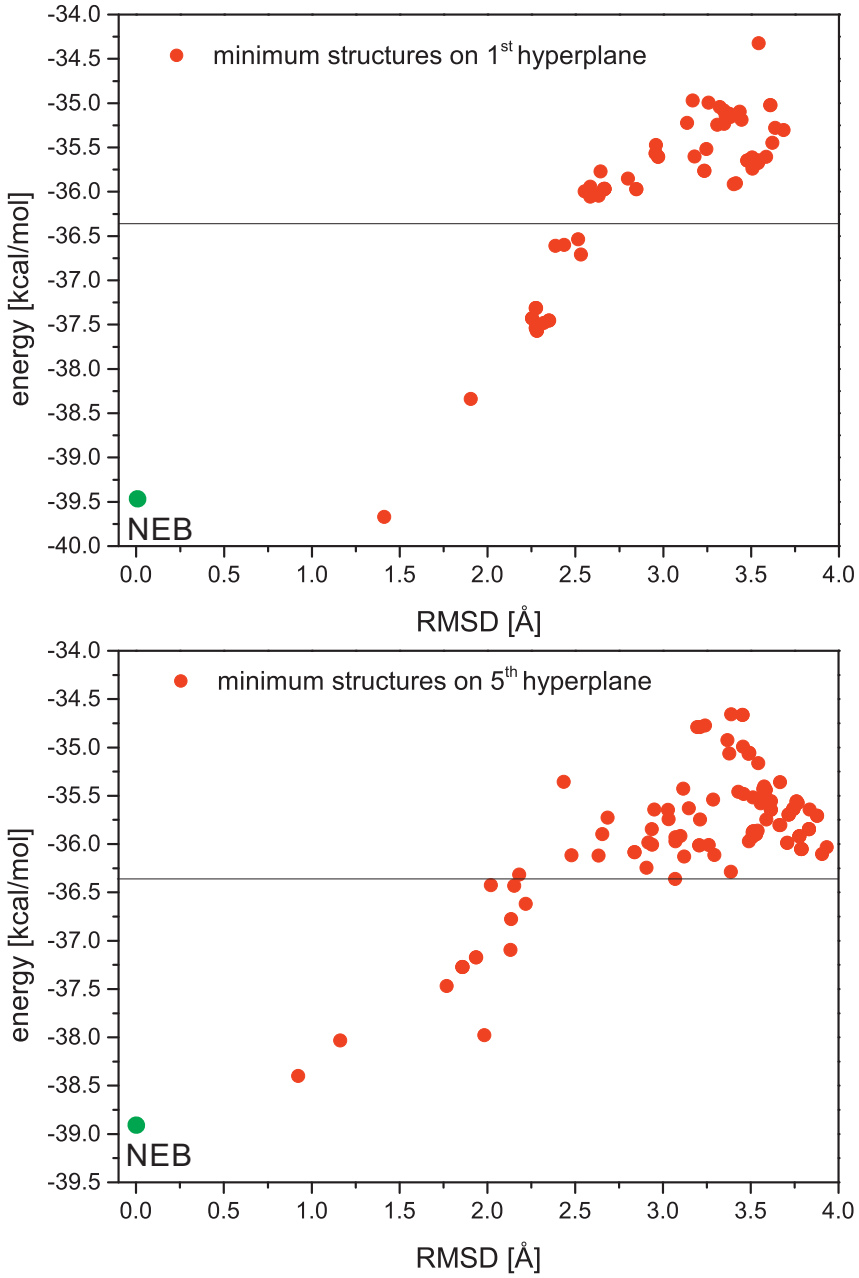

Figure 5.1.10: The minima on the 1^{st} and the 5^{th} hyperplane found for a simulation on ten hyperplanes for the Ar_{38} arrangement are given. The energies in kcal/mol are given with respect to the RMSD value in Å (referenced to NEB structure). The NEB reference structures are highlighted by green points.

By the representation of the minima found on one hyperplane this can be illustrated. For the 1^{st} and the 5^{th} hyperplane such a representation is given in Figure 5.1.10. For the

optimization on the first hyperplane it can be shown that additionally one minimum can be found which is lower in energy compared with the related structure from the initial NEB pathway. This is not always the case as it can be seen for the optimization on the 5^{th} hyperplane.

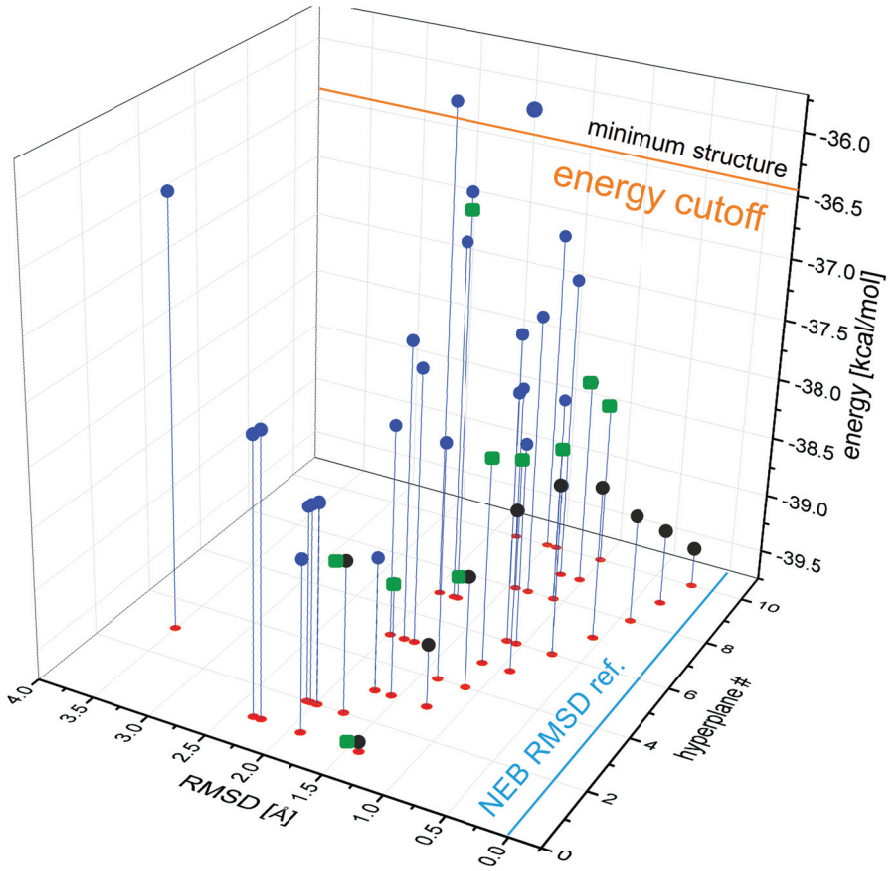

Figure 5.1.11: The excerpt which stems from a PO simulation on ten hyperplanes on the Ar_{38} cluster is depicted. The found minimum structures which are the lowest in energy are given by their energies (kcal/mol) and RMSD values in Å (blue points). The energy "cutoff" by about 2 kcal/mol is highlighted by the orange line. The green squares and black dots represent two possible pathways stemming from the PO optimization.

By applying the energy criterion the number of pathways might also be significantly reduced which is good illustrated by the per plane view with indicated cutoff (see Figure 5.1.10). Besides the classification of the found minima the next step is to look at the obtained pathways. Therefore, a closer look on a 10 hyperplane simulation with the same

settings applied as for the 20 hyperplane calculation should be made. The excerpt of minima with respect to RMSD and hyperplane is given in Figure 5.1.11. Within this representation two possible pathways are depicted. The black dots represent the minimum RMSD pathway found by starting at the first minimum on the first hyperplane. The green squares symbolize an additional pathway. The pathway represented by the black dots is only at a few points significantly different with respect to the initial NEB pathway, whereas the second PO pathway varies much stronger. For having a closer look at the differences between these three pathways (NEB, PO1 and PO3) the RMSD and energy profile can be compared. This representation is given in Figure 5.1.12. By looking at the RMSD change for the pathways, it can be seen that indeed for NEB a mostly linear change is obtained. For the PO1 pathway one significant outlier is obtained, but for the PO2 pathways a more or less complete different pathway is found. Besides the differences in RMSD values the energy changes mirroring the RMSD differences. The differences between the PO1 pathway and the NEB one can be illustrated by looking at the structural representation of the found pathways which is illustrated in Figure 5.1.13. Here the structures are overlaid represented which shows the transition between the two arrangements. The most significant difference which is also observable by looking at the RMSD change (see Figure 5.1.12) is related to the third structure which is highlighted. In consequence, it can be stated that the new connection procedure and the simulation on multiple hyperplanes offers additional pathways which exhibit new features. The different applied criteria help to identify and distinguish between the new pathways and also make it possible to confirm the importance for the overall description of a transition.

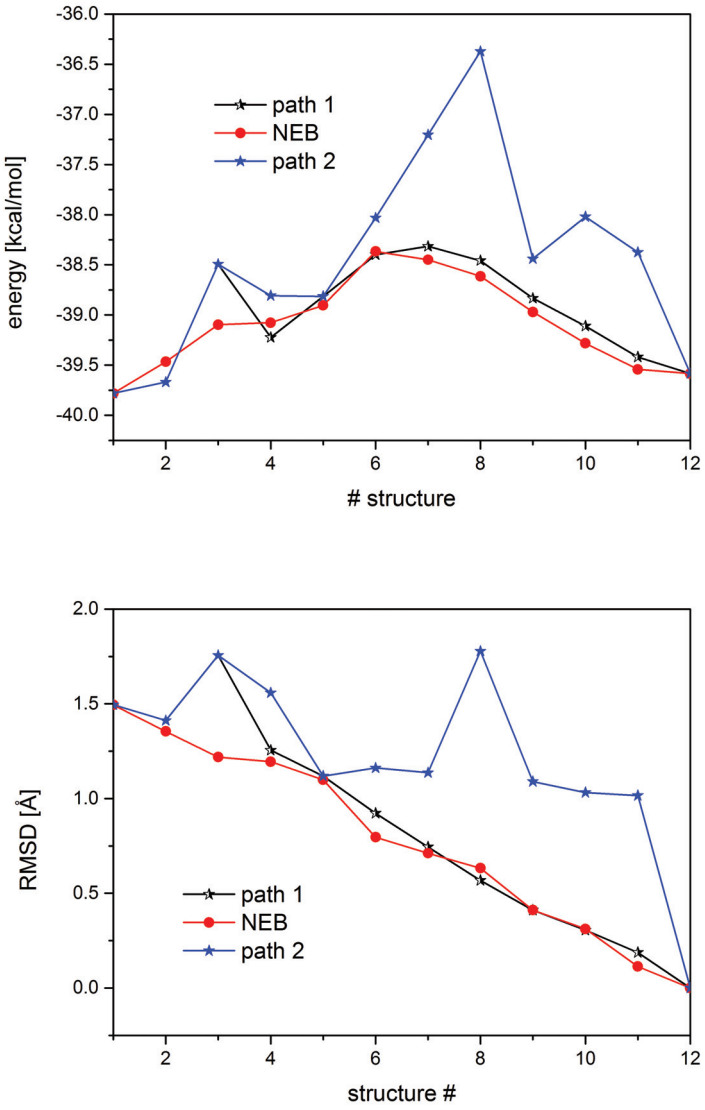

Figure 5.1.12: On the top the energy profile of two PO pathways and the concerning NEB pathway is given. On the bottom the RMSD value changes for the depicted pathways are shown. The first (1) and the last (12) points are the starting and the final structure.

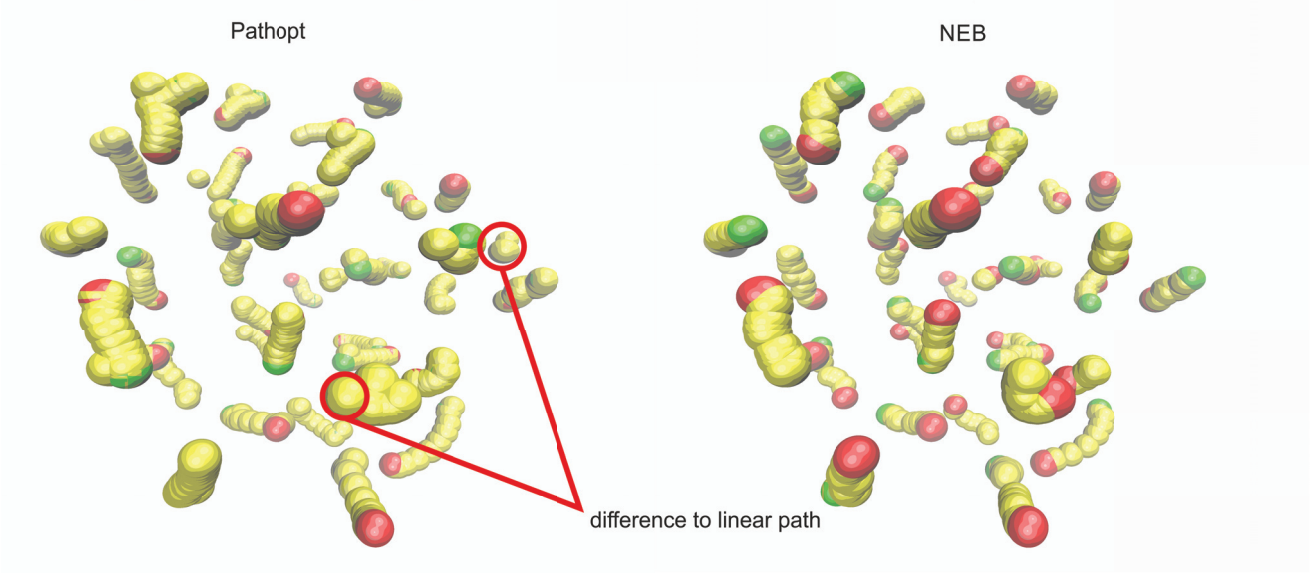

Figure 5.1.13: The explicit pathways for the Ar_{38} rearrangement are depicted. On the left side the PO path 1 is shown and on the right side the NEB pathway. Two points which are different between the depicted patwhays are highlighted by the red circles. The starting structure is given in green and the final one in red.

The second cluster system which has been investigated is the water cluster which consists of 20 monomers. The directionality of the interactions within the water cluster is the main difference to the vdW cluster described beforehand. Hence, the water test system can be referred as the logical next candidate to prove the ability of PO. For the PO optimization the same strategy was used as for the argon clusters which means Cartesian steps only and gradient projection scheme applied. For the water optimization also a few pathways were obtained and to show the capabilities of PO one pathway is depicted. To prove the results which one obtains from a PO optimization the last step after a successfully applied criterion for building the complete pathway (RMSD / energy) would be the characterization of the pathways by calculating the vibrational frequencies along the pathway. This was done and is shown in Figure 5.1.14. Two TSs are found along this PO pathway, whereas the first one is located for the ninth structure. The frequency for the first mode of this structure is $21.17cm^{-1}$. The frequency modes of the second and third modes are zero. The frequency of the second TS is of about $-6.03cm^{-1}$. For the other structures of the pathway smaller imaginary frequencies or zero values for the minima are found. These results might indicate

that a realistic pathway is found by using the PO algorithm without any further refinement applied. Compared with the found NEB TS the PO one is of about 1 kcal/mol lower in energy.

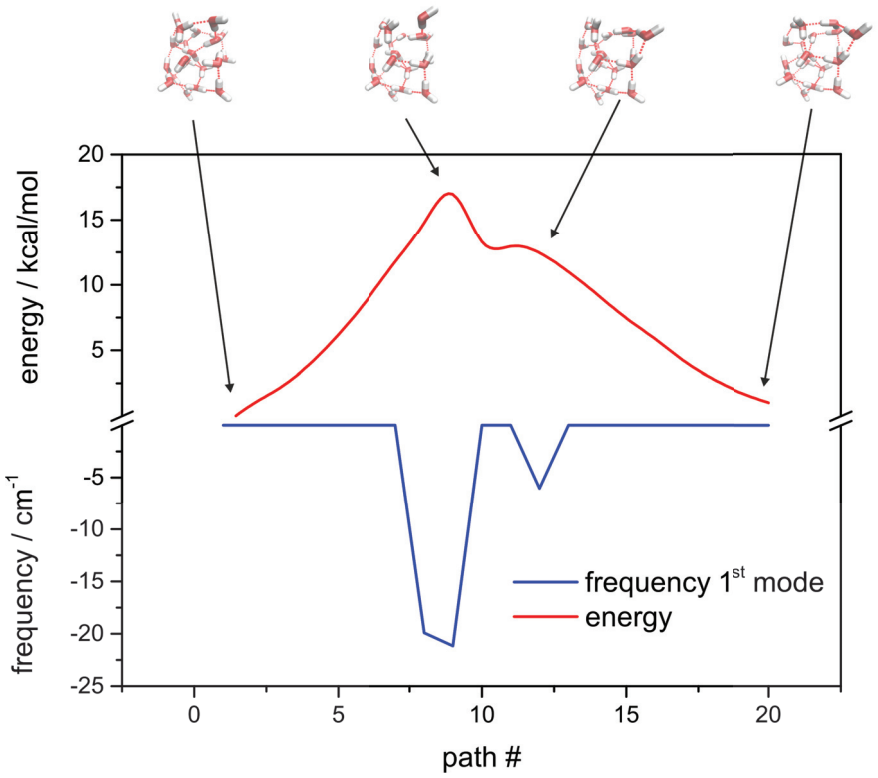

Figure 5.1.14: The minimum energy pathway for the transition of the $(H_2O)_{20}$ cluster is depicted. The pathway stems from a PO optimization on 18 intervening hyperplanes. In the upper panel the energies (kcal/mol) and in the lower panel the frequencies of the first mode in cm^{-1} are given.

Radical polymerization reactions

Within this section we want to widen the focus on chemical reactions instead of arrangements. The reaction which are in the focus are start reactions within a polymeric chain reaction. For the presented systems the choice of the move strategy and coordinate representation can be important. The first reaction which is described takes place between pyrrolidin-2-on-propyl radical and acrylic acid. The reaction is shown within Figure 5.1.15. To characterize the reaction the PO methodology was applied by using different move strategies and different optimization settings. In addition to the PO and NEB calculations re-

laxed PES scans were conducted to prove the results obtained and to identify the reaction coordinates. The energies and gradients were calculated using the CAST interface with the semi-empirical code implemented in MOPAC2012[50]. Therefore, the AM1[51]- and the PM6[52]/PM6-DH2/PM6-D3[53, 54]-Hamiltonians were used and will be referenced to the respective method applied. All calculations were UHF based ones. The semi-empirical methods were chosen because of the existing interface within the CAST program and the fact that they are relatively cheap and a multitude of global optimizations on various number of hyperplanes is getting feasible within an acceptable time span. For the obtained minimum pathways B3LYP[55, 56, 57, 58, 59]/TZVP[60] (Turbomole 6.6[61]) single points calculations were carried out for validation.

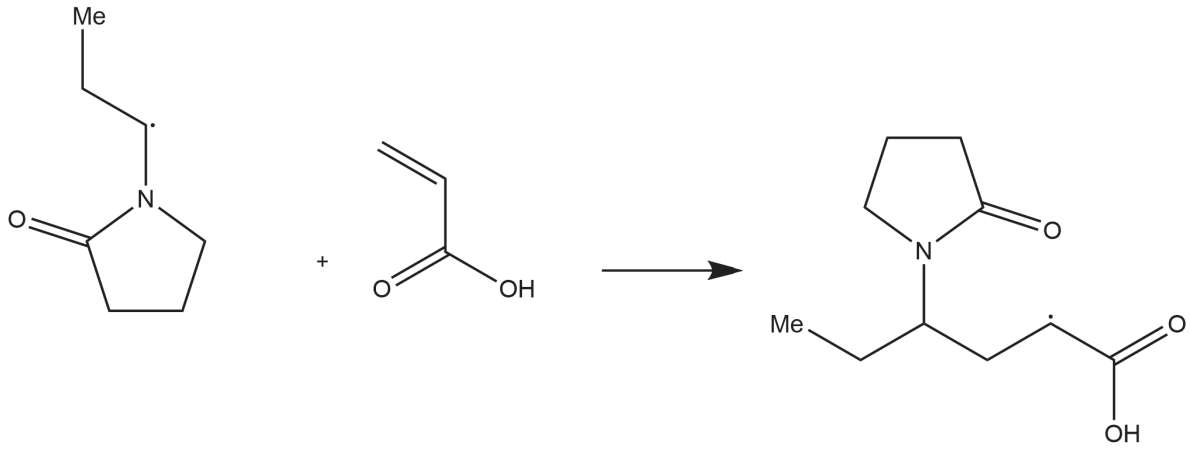

Figure 5.1.15: The start reaction for the radical polymerization between acrylic acid and the pyrrolidin-2-on-propyl radical is depicted.

In the first step a global optimization for the start and final structure was carried out. In our case we applied the MCM scheme, whereas 100 MCM steps were carried out using the dihedral move strategy at 298.15 K temperature for the Metropolis criterion. The structures obtained for both runs are depicted in Figure 5.1.16. For a more or less linear arrangement of starting and final structure a pathway is obtained which can be seen as the MEP. The resulting pathway by using the PM6-D3 approach is shown in Figure 5.1.17. The parameters for the first test run were set as follows: 12 intervening hyperplanes, 200 MCM steps per plane, gradient projection scheme, a step size of 0.7 Å and T = 298.15 K. In addition to the PM6-D3 pathway also on the AM1-level pathways were calculated. Therefore, also for- and backward reaction were optimized. In Figure 5.1.21 the NEB forward and backward pathways and two PO pathways are depicted. Up to this point the results obtained seem

to be promising, but the ability to find multiple pathways which are sufficiently different to the linear pathways was not tested so far. Therefore, the RPs obtained with different move strategies were analyzed. The pathways obtained by small step sizes and Cartesian only steps were all very similar to the linear pathway and no large variations occur, especially no rotations. By analyzing PES scans for the main degrees of freedom we concluded that by describing the rotation around the newly formed bond (rotation of the acrylic acid), additional pathways can occur. Therefore, the PES scans are depicted in Figure 5.1.19 and 5.1.20. At least three additional pathways might be obtained by rotating around the newly formed bond.

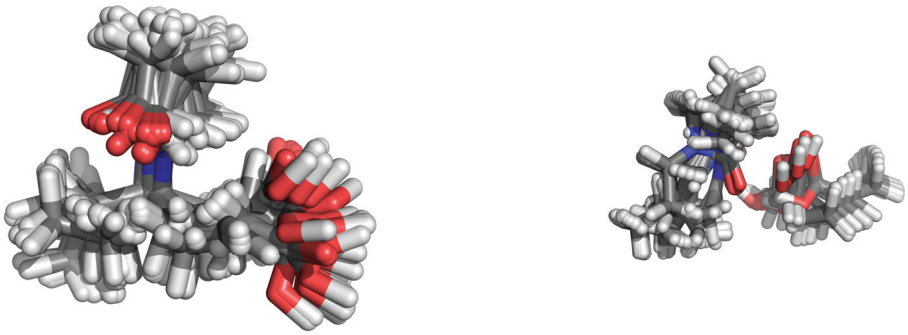

Figure 5.1.16: Left: The results of the MCM optimization on PM6-D3 level of theory are depicted which are related to the bonded species of the reaction between pyrrolidin-2-on-propyl and acrylic acid. Right: Results of the MCM optimization on PM6-D3 level of theory which are related to the starting structure of the reaction between pyrrolidin-2-on-propyl and acrylic acid are shown.

Besides the rotation around the newly formed bond the pyrrolidin-2-on-ring rotation can be important and offers in principle additional pathways. This rotation was not described with the standard move strategy which has been fruitful applied for the cluster systems. Therefore, we applied the mix-move strategy as well. For the rotation of the pyrrolidin-2-on-ring we were able to find additional minima on the hyperlanes with different angles for the pyrrolidin-2-on-ring rotation. The results for a PO run on ten hyperplanes are depicted in Figure 5.1.18. Besides these results, the pathway obtained from the first PO run with "normal" move strategy seems to be the minimum energy pathway. The parameters for the TS are in a good agreement with the PES scan results. For the scan the TS occurs at an inter-monomer distance (newly formed C-C bond) of about 2.1 Å and PO predicts the same value. The C=C double bond distance is also very similar described by both approaches. PO predicts a distance at the TS of about 1.36 Å and for the PES scan 1.37 Å are obtained.

The NCCC angle is of about 60°, whereas the angle can slightly vary depending on the parameters changed within a PES scan carried out. In this manner for example one can vary the inter-monomer distance (C-C) and the bending angle defined by the atoms of the new bond and the C=C bond (C-C=C) and obtains an NCCC angle of about 63°.

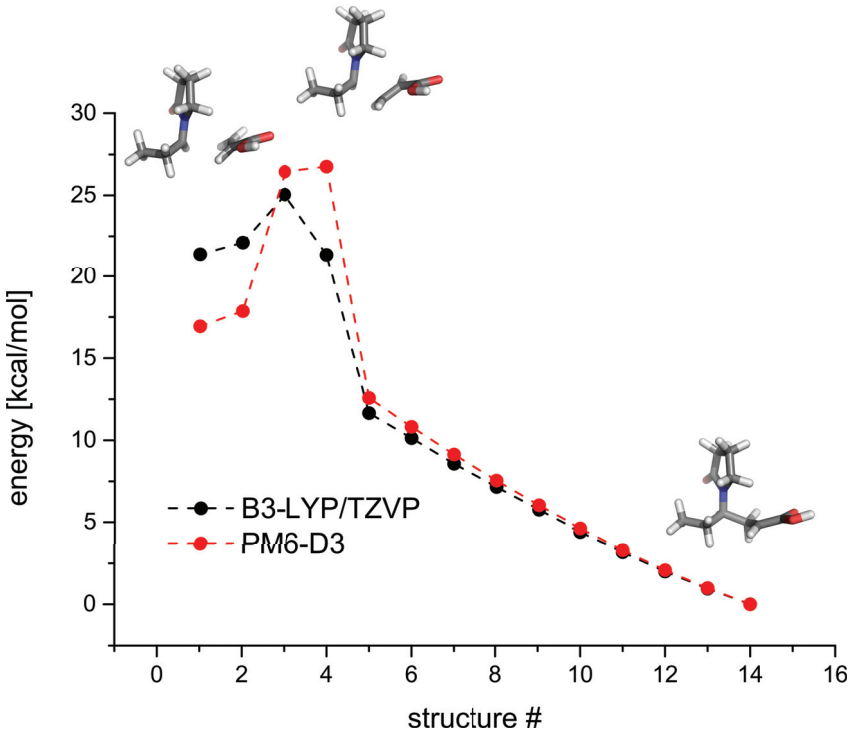

Figure 5.1.17: Reaction pathways for the polymerization start reaction between pyrrolidin-2-on-propyl radical and acrylic acid obtained with the PO procedure (on 12 intervening hyperplanes). The starting structure was set to be the bonded species. The PM6-D3 Hamiltonian was used. The B3LYP pathway refers to single point calculations on the PM6-D3 pathway.

In addition, the single point calculations on B3LYP/TZVP-level of the obtained PO pathway confirm the results and the prediction of the barrier height of the reaction by using PO. The barrier height predicted is of about 9.8 kcal/mol for the PM6-D3 approach. The single point calculations starting from these structures would predict an even lower barrier-height of about 3.7 kcal/mol. The latest AM1-calculations with PO predict a barrier-height for the forward reaction of about 6.1 kcal/mol. The predicted barrier-heights with NEB, which are essentially larger are of about 11.9 kcal/mol.

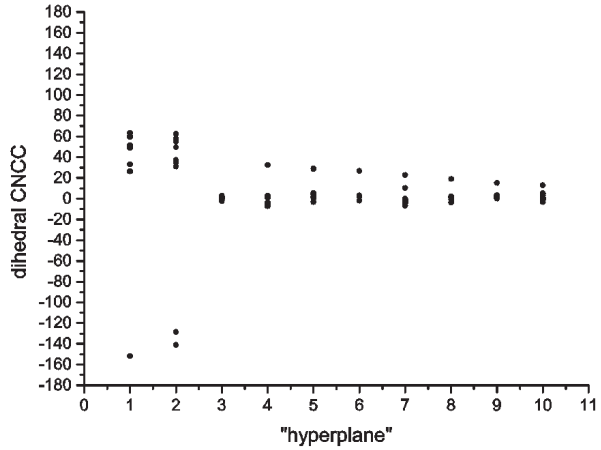

Figure 5.1.18: The values for the dihedral angle, which defines the rotation of the Pyrrolidin-2-on ring (CNCC) are plotted for each hyperplane.

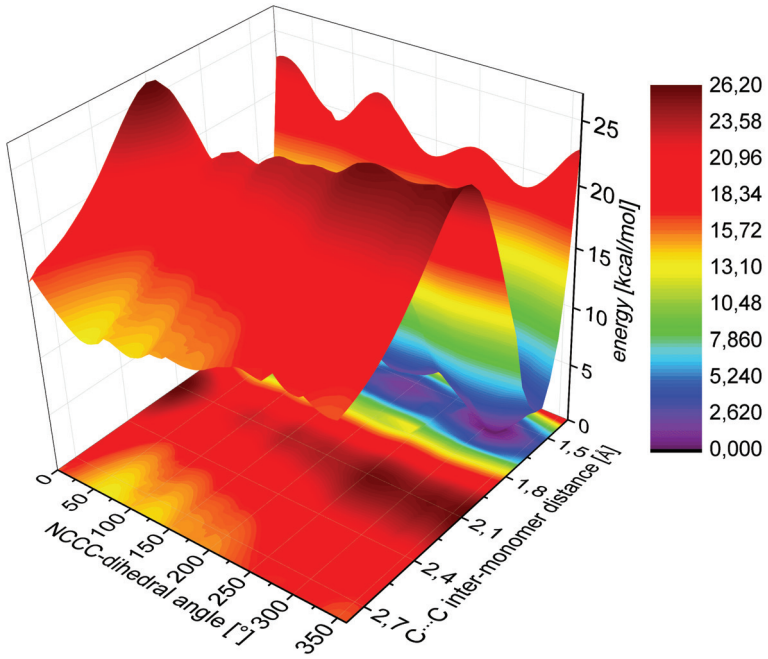

Figure 5.1.19: PES scan for the reaction between pyrrolidin-2-on-propyl radical and acrylic acid. The relative energies in kcal/mol are depicted for the variation of the bond distance C-C that is formed during the reaction and the dihedral angle NCCC, which defines the rotation around the newly formed bond. The PM6-D3 Hamiltonian was used.

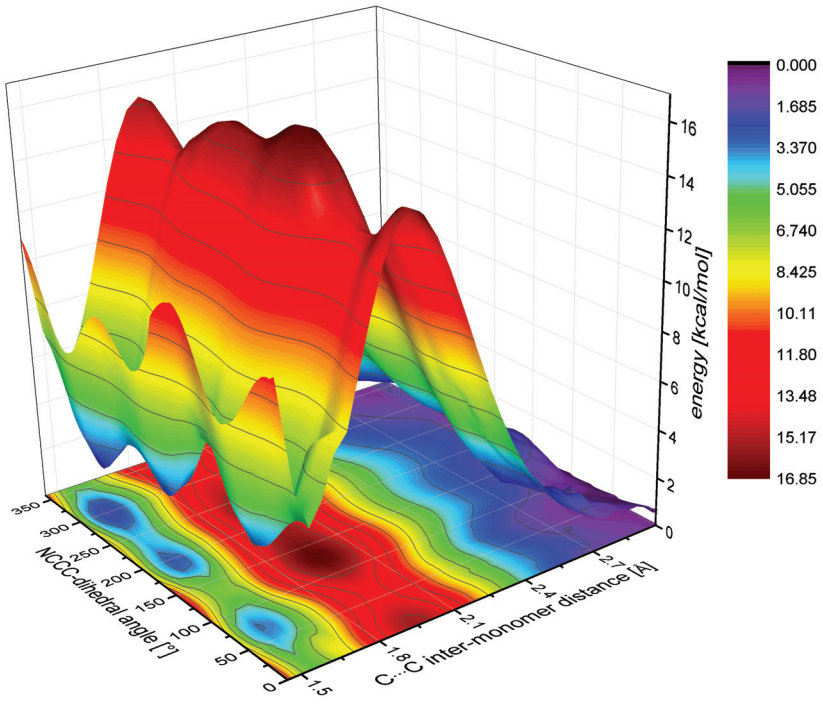

Figure 5.1.20: PES scan for the reaction between pyrrolidin-2-on-propyl radical and acrylic acid. The relative energies in kcal/mol are depicted for the variation of the bond distance C-C that is formed during the reaction and the dihedral angle NCCC, which defines the rotation around the newly formed bond. The AM1 Hamiltonian was used.

In consequence we can state that the barrier for the reaction can be described by using the PM6-D3 approach in a quite good manner using the PO methodology, while the TS predicted by the NEB approach is in the same range for the heights but may slightly overestimate the barriers. The same holds for the improved NEB implementation within the CAST program by using the whole band within the minimization process and the climbing image variant. Up to this point the IDPP approach was not tested on this system. The usage of "global" NEB in comparison of a local approach quite improves the convergence for the radical polymerization test systems. Besides the discussion of the minimum energy pathway also the additional found pathways should be mentioned. Therefore, a special focus is set on the description of rearrangements. In Figure 5.1.21 one of the "non"-mininum pathways is depicted which involves a 1,2-rearrangement. In fact, to obtain such rearrangements within one PO run and additionally other side reactions is interesting and makes it possible to obtain a deeper understanding of the possible reaction space, although they are of minor importance in this case. The presented second PO pathway offers three TSs, whereas the first one is described by

a rotation of the hydroxy-group out of plane with respect to the carbonyl-oxygen. The second TS occurs for the 1,2-rearrangment which can be described by a structure with a slightly pyramidal nitrogen within the pyrrolidin-2-on ring and the shifted hydrogen atom. For this structure the hydroxy-group is rotated back in plane. The third TS can be characterized by a different configuration of the acrylic acid ($C_3H_4O_2$) which can be described by the formation of 3-hydroxy-propenal ($C_3H_4O_2$), whereas the formation might not be very likely.

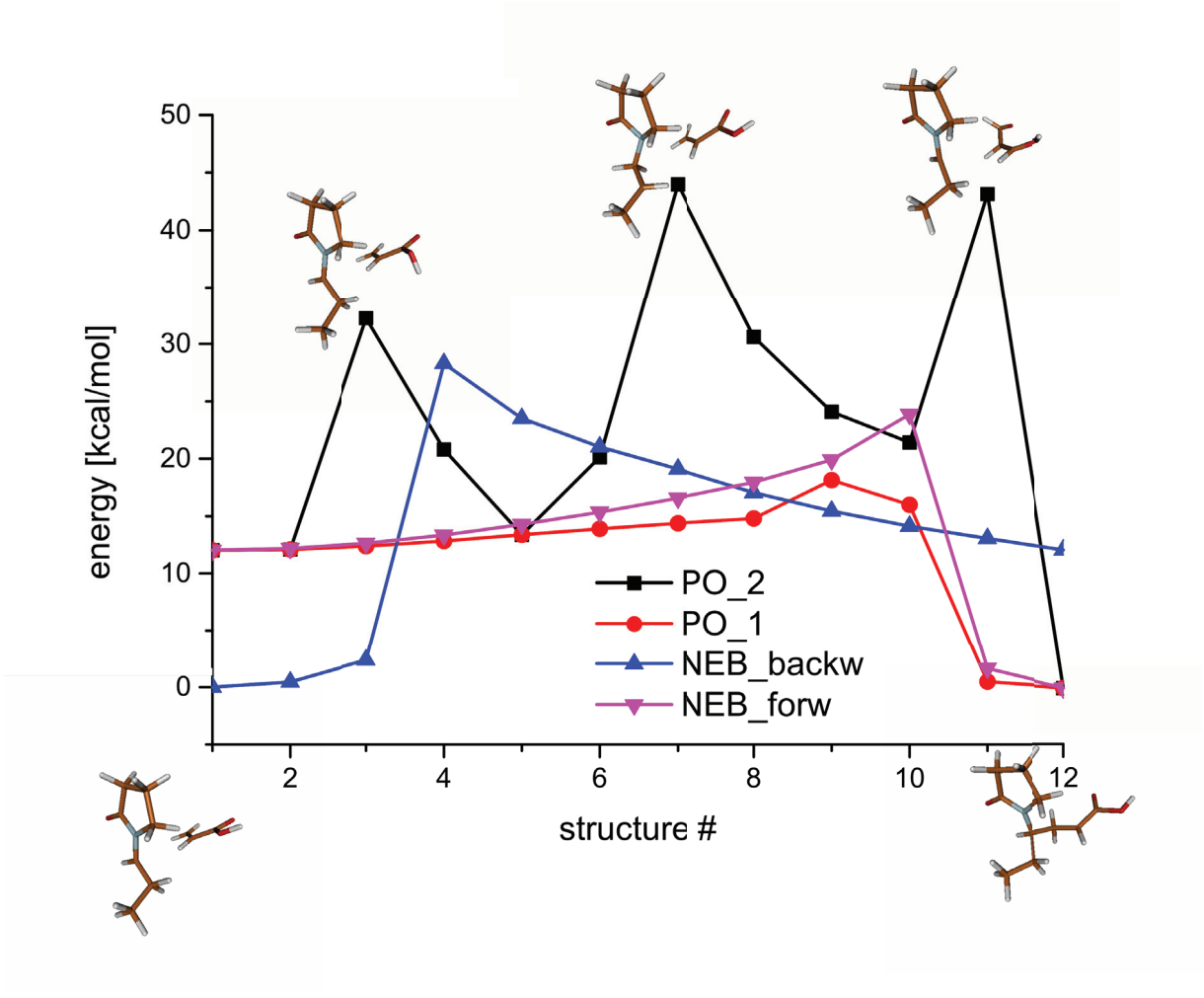

Figure 5.1.21: Reaction pathways for the polymerization start reaction between pyrrolidin-2-on-propyl radical and acrylic acid obtained with the PO procedure (on 12 intervening hyperplanes). The starting structure was set to be the non-bonded species. The AM1 Hamil- tonian was used.

In the following, the start reaction of the polymerization between vinyl chloride and n-

propyl chloride should be shortly presented (see Figure 5.1.22). In comparison to the first presented reaction it is simpler to describe. Beforehand, we carried out a MCM optimization to generate starting structures for the bonded and the non-bonded system which defines the edges of the band. The results for the MCM search with 100 MCM steps applied by using the dihedral move strategy at 298.15 K temperature for the Metropolis criterion, are given in Figure 5.1.23. Within the first test calculations on this system we had problems to identify the TS correctly. Therefore, two PO connections were applied. This means that the start calculation was defined by the start and final structure of the band using 10 intervening hyperplanes. Then in a second step a PO run was carried out between the last one and the final structure of the pre-calculated path. In this manner it was possible to get a smooth description of the minimum energy pathway. The excerpt of the refined pathway is given in Figure 5.1.25.

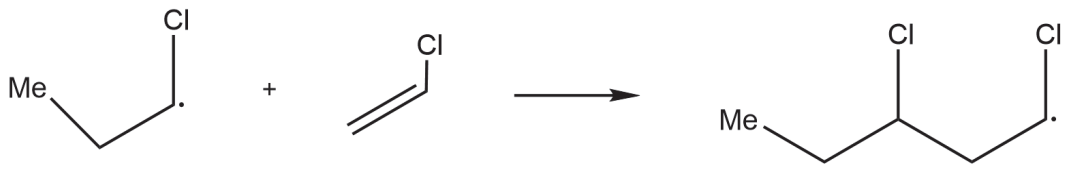

Figure 5.1.22: Radical polymerization start reaction between vinyl chloride and n-propyl chloride.

In combination with the PO pathway the NEB one which stems from the implementation of a local variant of the NEB optimizer is presented. The method for calculaitng energy and gradients was in this case the PM6-DH2 approach. The overall reaction is described well by using the inter-monomer and the C=C double bond distances. Therefore, also the PES scan is given in Figure 5.1.26. The distances describing the pathway obtained for the PO and NEB pathways are also given for a comparison of both in Figure 5.1.24. From the analysis of the pathways it can be seen that PO predicts a linear and smooth change for both distances.

Figure 5.1.23: Left: The results of the MCM optimization on PM6-DH2 level of theory are depicted which are related to the bonded species of the reaction between vinyl chloride and n-propyl chloride (final structure). Right: Results of the MCM optimization on PM6-DH2 level of theory which are related to the starting structure are shown.

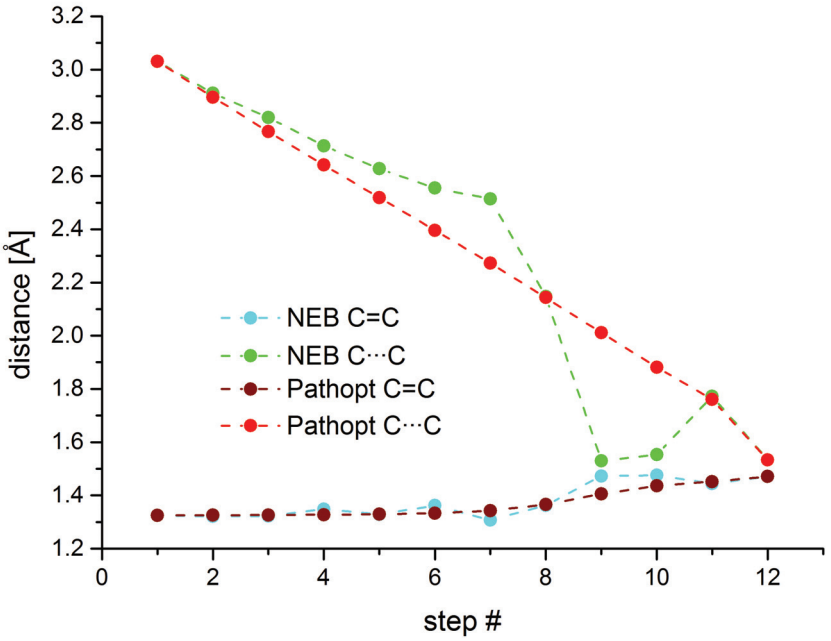

Figure 5.1.24: The inter-monomer and C-C distances for the start reaction between vinyl chloride and n-propyl chloride are shown. The distances are related to the NEB and one PO pathways.

The relative barrier obtained from the PES scan is of about 8.3 kcal/mol. In comparison with PO this is in a good agreement which delivers a barrier of about 8.9 kcal/mol and is in a better agreement than the NEB predicted barrier of about 10.5 kcal/mol.

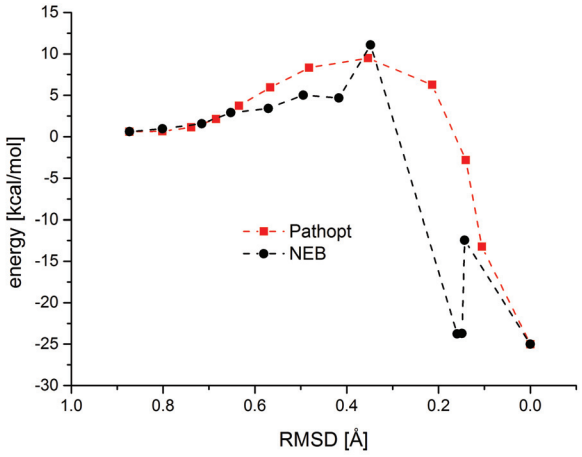

Figure 5.1.25: The energy profiles for start reaction between vinyl chloride and n-propyl chloride are given for the NEB and the PO method. The change of the reaction is related to the RMSD value change. The method of choice is the PM6-DH2 semi-empiric approach.

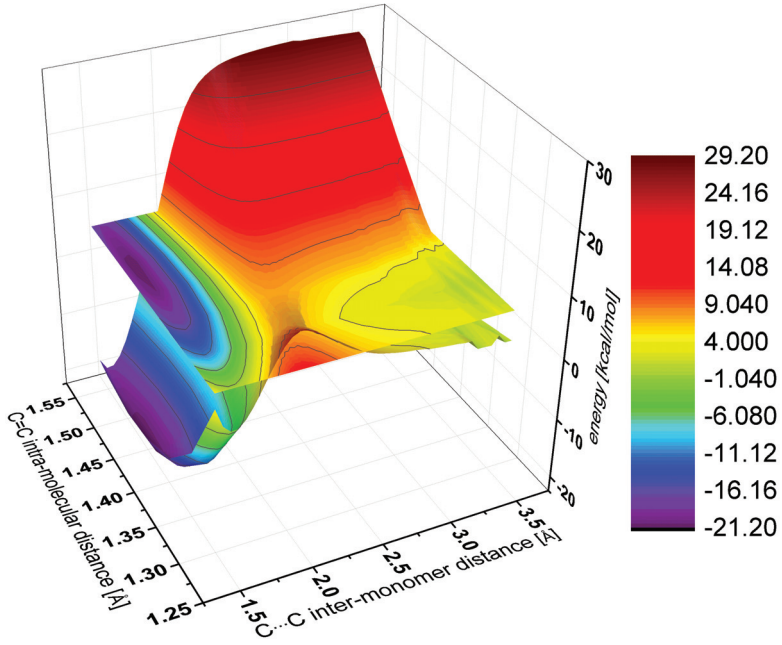

Figure 5.1.26: The PES scan of the reaction between vinyl chloride and n-propyl chloride is given by varying the inter-monomer (C-C) and the double bond distance (C=C). The energy calculation was carried out by using the PM6-DH2 Hamiltonian.

In summary with respect to the described polymeric start reactions we can state that

in principle PO is able to deal with such problems by using the interfaces to QM programs delivered by CAST. In some cases it gives even better results than the NEB methodology (improved method by Henkelman/climbing image). Nevertheless, the description of such reactions can be unexpectedly demanding. As it was mentioned the choice of the move strategy can be important to obtain most of the reasonable pathways in a reasonable time. Therefore, the mixed-move strategy was introduced. Also an optimization with applied bias potential instead of the gradient projection scheme can lead to good results, but by formally leaving the strict constraint.

Ubiquitin PO simulations

Within this section the results of the optimization of ubiquitin protein (UBQ) are presented. We want to show that it is possible to leave the smaller test systems and begin to treat larger molecules with the PO approach. Therefore, we investigated the conformational transition of one stable UBQ conformation to another more unstable minimum which lays 30.4 kcal/mol higher in energy. The general approach to treat this system was to perform a MCM search beforehand to generate minima which can then be used for the RP search. The energy describing method was in this case the OPLS-AA FF[39, 40, 41, 42]. The PO simulation was carried out on 15 intervening hyperplanes, the mix-move strategy was applied and the Cartesian step size was set to 0.8 Å (energy range of accepted minima was set 60 kcal/mol). One total search by using 100 MCM steps per plane took 4.4h on a single CPU (Desktop) system. For the case of the UBQ also NEB calculations with different temperature settings were applied, like in the section 4.1.4 described.

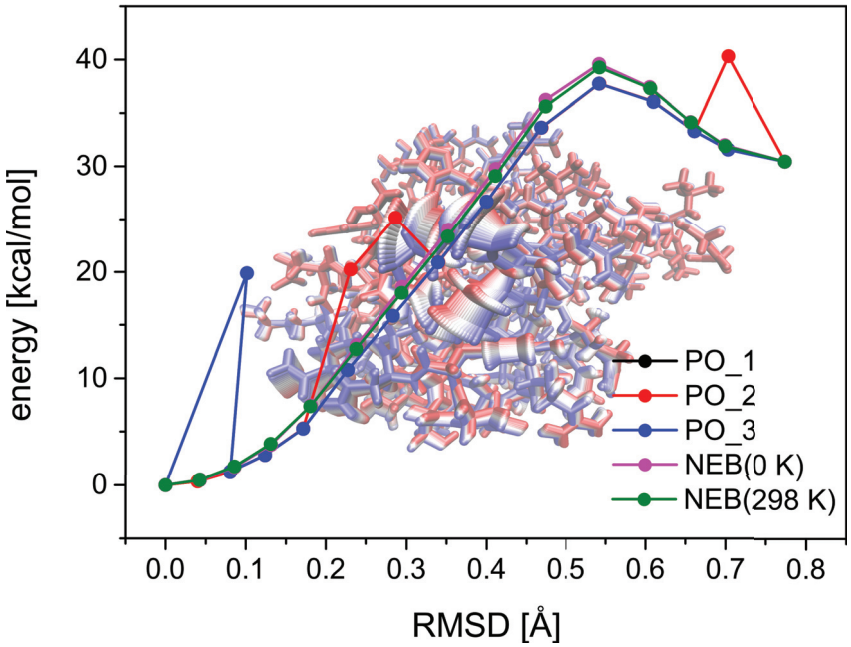

Figure 5.1.27: Pathways which describe conformational transition between two UBQ conformers are given. The 0 and 298 K pathways obtained from a NEB optimization are given besides three obtained PO pathways. The energies are related to the OPLS-AA FF and the reaction progress is described via RMSD value change, whereas the path is built up by 15 structures (13 intervening hyperplanes within the PO procedure). In the background the transition in a molecular picture is given by overlaid frames for the minimum energy pathway.

In Figure 5.1.27 two NEB pathways for 0 and 298 K and three possible PO pathways are shown. The differences between the 0 and 298 K NEB pathways remain small and also the differences between the PO minimum pathway and the NEB ones are not very large. The minimum PO pathway and its TS is slightly lower in terms of energy compared to the NEB pathway, but the differences are negligible. For the additionally picked PO pathways larger differences occur and further TSs are found. If the TSs of the depicted pathways are in comparison with the TS of the minimum pathway lower in their energy or comparable and if the main TS of the minimum pathway is the rate determining step also additional TSs can be included and the related pathways are accessible. Hence, they play a role in the overall description of the transition. Besides the depicted pathways there exists of course possible pathways which possess larger barriers. To illustrate this, in Figure 5.1.28 all minima obtained within this PO run are depicted, related to their hyperplane. The minima found span up a range of about 58 kcal/mol and compared with the minimum pathway TS the highest found TS is 21 kcal/mol higher in energy. Such transitions would play only a minor role in the

description of the overall process (see also Ar_{38} study). Summarizing these results, the PO procedure is also applicable to larger molecules, like proteins in a reasonable computational time. The use of the mix-move strategy seems to be recommended.

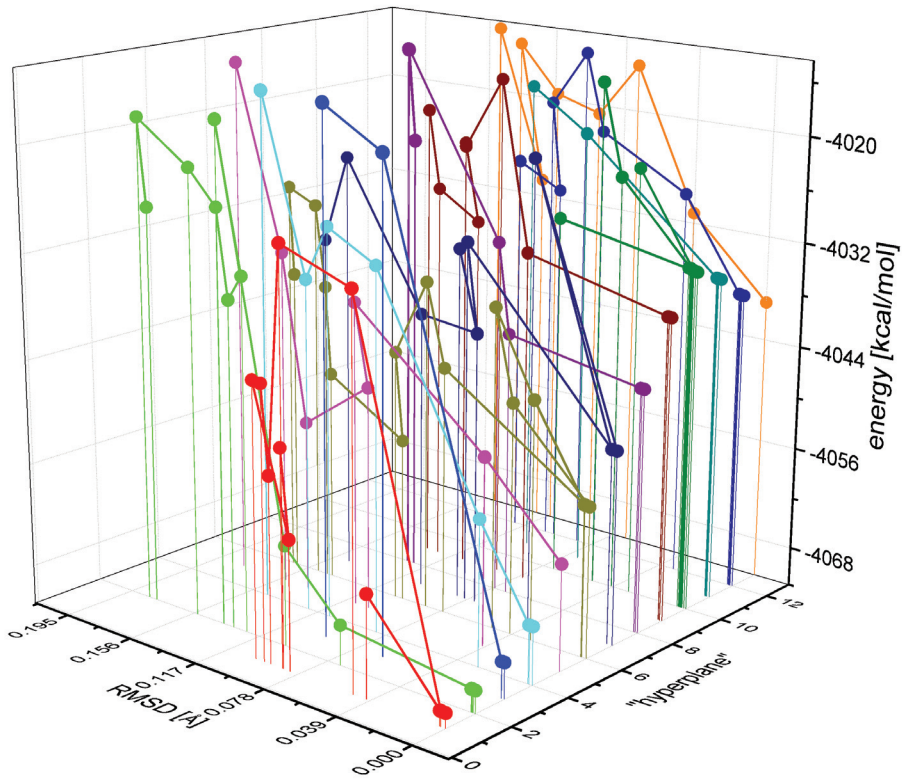

Figure 5.1.28: All obtained minima from one PO run on 13 intervening hyperplanes are given with respect to their RMSD referenced to the starting structure on each hyperplane.

5.1.3 Sampling strategies and perpendicular sampling - the tridecaalanine

For the tridecaalanine system the transition between different peptide conformations has been investigated to address different global optimization strategies. Therefore, we want to have closer look on the choice of different coordinate systems, as well. The starting structures for this purpose are illustrated in Figure 5.1.29.

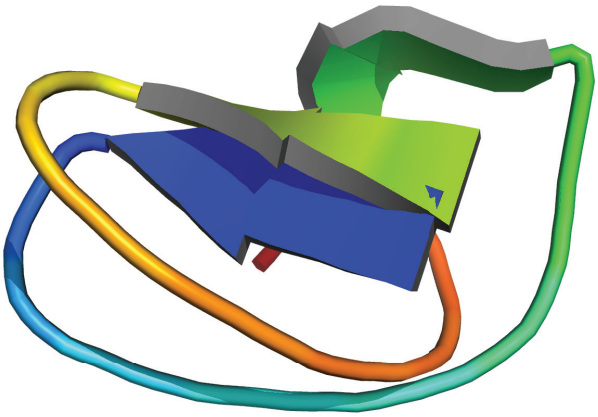

Figure 5.1.29: Two conformations of tridecaalanine are given which were obtained from a Tabu Search (GOTS)[62, 63, 64, 65] optimization with the OPLS-AA FF. They are represented by two beta-sheet cartoons.

As already utilized in the previous sections the progress of a reaction can be shown by the RMSD value change. This representation e.g. for a reaction paths can deliver further insight into the overall progress and makes pathways comparable with each other. Instead of the RMSD value also other reaction coordinates might be chosen. In PES calculations, often distances or angles are used, but they are not general in their description. Therefore, various approaches exist like the intrinsic reaction coordinate approach (IRC)[66], integrated path lengths or using main modes from a principal component analysis (PCA)[67]. In addition to an one dimensional RMSD value representation two dimensional RMSD matrix plots can help to understand the data obtained from a global optimization or from MD simulations. In Figure 5.1.30, the RMSD matrices for tridecaalanine are summarized. The general structure of a RMSD matrix is a real symmetric matrix whereas the diagonal elements are zero.

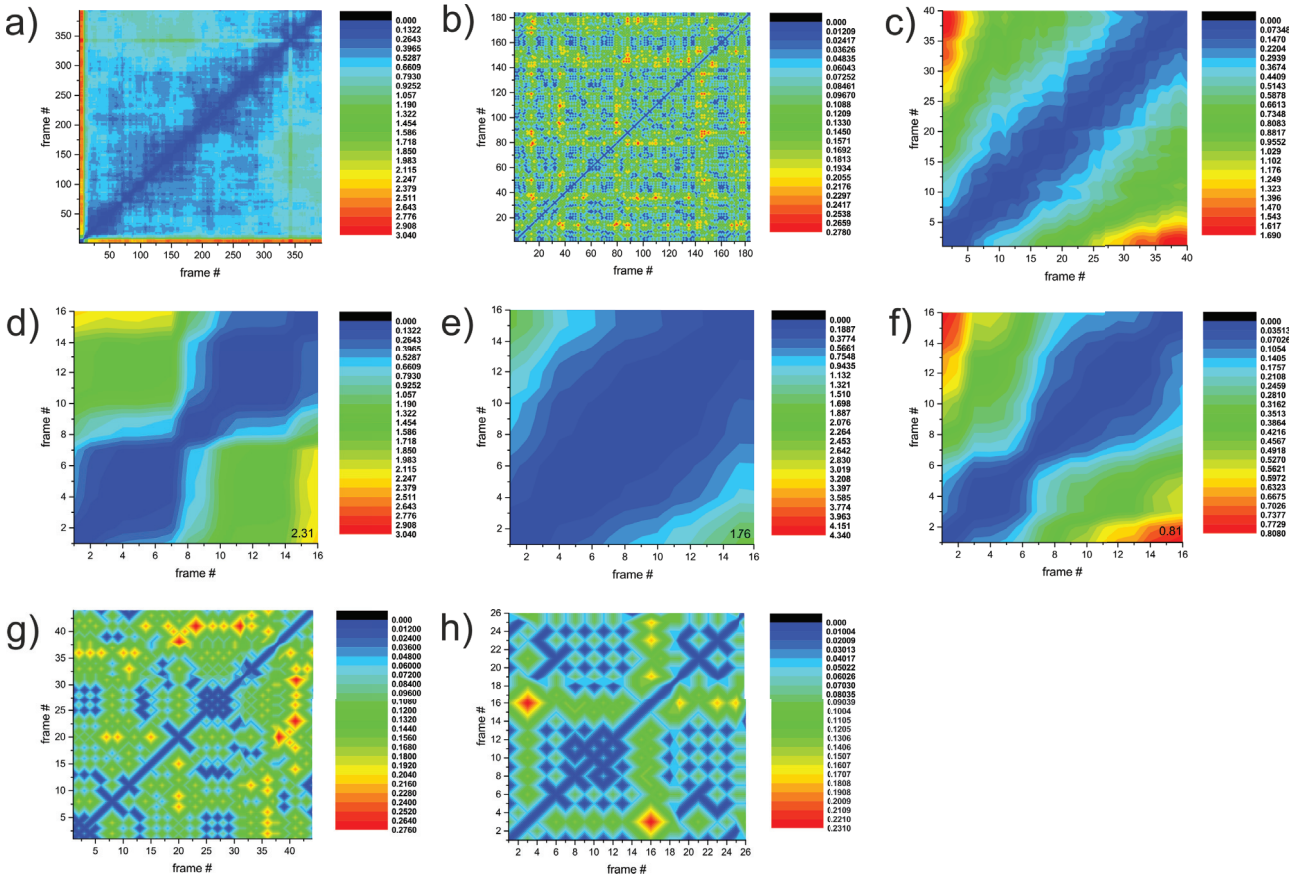

Figure 5.1.30: RMSD matrix plots are shown for different simulation cases during a PO optimization. The RMSD distances are given in Å indicated by different colors (blue=0.0, red=max.). The investigated system is the tridecaalanine. The optimization was carried out on 20 connecting planes within PO and the depicted results stem from the simulation on the first plane: a) unrestricted global optimization with perp. MC steps; b) multiple MCM simulations (5 iterations) with applied projection scheme and perp. MC steps; c) multiple MCM simulations (5 iterations) with bias (k=0.1) and perp. MC steps; d) single MCM simulation no bias (k=0.00); e) single MCM simulation with bias (k=0.05); f) single MCM simulation with bias (k=0.1); g) single MCM simulation with projection scheme and Cartesian only moves; h) single MCM simulation with projection scheme and mixed moves (Cartesian/dihedral)

The color code represents different RMSD values for each pair of frames within Figure 5.1.30. The coding starts from zero RMSD, which is indicated by blue and ends up with red which stands for high RMSD values, respectively. All the depicted results stem from the optimization on the first hyperplane for a simulation, which was carried out by using 20 connecting NEB structures. Example pathways from this simulation are depicted in

Figure 5.1.31. For the simulation with applied bias potential a clear trend is observable. With increasing frame number the RMSD values continuously increase. This means that the RMSD change between early and late structures is larger than the combination of early frames (structures) with early frames. In addition, the influence of the force constant can be seen within the series of RMSD matrices (d-f). The frame combinations starting with frame 0 ending up with frame 16 are shown. For the simulation with no applied bias potential (d) the maximum RMSD distance measured is of about 2.3 Å. By using a bias which is illustrated in (e) the RMSD value decreases to 1.8 Å. Further increasing of the bias leads to an additional decrease in RMSD to the value of 0.8 Å (f). In addition to the single runs, also multiple runs (5 times) were carried out with applied bias (k=0.1) which can be seen in (c). The results obtained for multiple runs are in a good agreement with the single run (f). For the frame 0 to 16 combination, the RMSD value is of about 0.8 Å for all runs. Therefore, the single run results might be reproducible. For the multiple runs the parameters were set as follows: 4000 steps at 200 K and 4 repetitions. For the simulation with the gradient projection scheme a different pattern for the RMSD matrix is obtained. The values do not continuously increase with increasing frame number. In addition, the overall deviations between the structures are smaller. A checkerboard pattern is obtained for (b+g). This means that the overall deviations are smaller and similar structures with respect to the starting structures in the simulations are found. In consequence, it can be stated that this kind of search is more restricted. On the one side this is exactly what it is meant to be, but on the other side, as already mentioned before scanning all possible combinations e.g. rotations is not easily feasible. Therefore, the mixed move strategy can be included. The results are depicted in (h) where the same pattern like in the Cartesian only methodology with gradient projection is obtained, but the maximum RMSD, by comparing the frame numbers, is slightly increased.

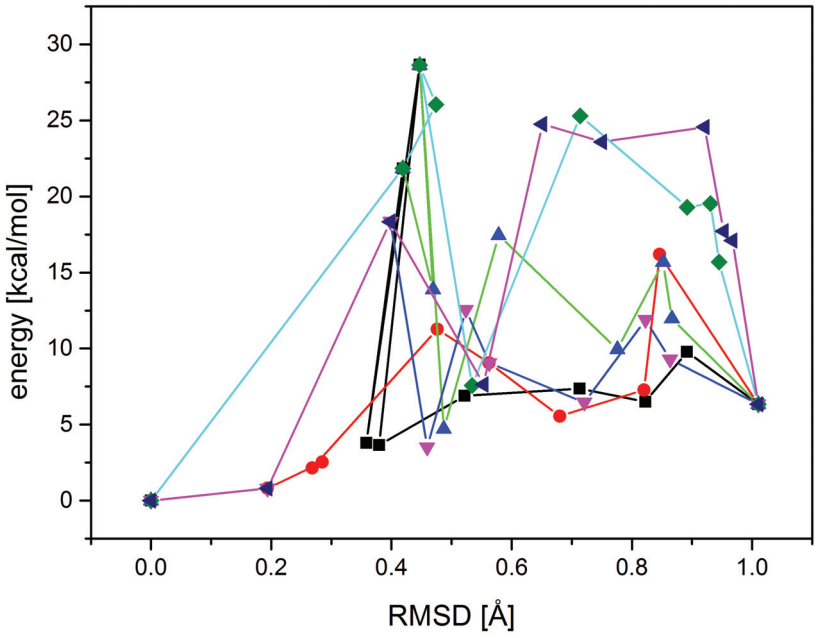

Figure 5.1.31: Various pathways for the transition between two conformations of tridecaalanine are depicted. The energy in kcal/mol is depicted versus the RMSD value in Å. The OPLS-AA FF was used.

In consequence, it can be stated that the diversification is less by using the Cartesian only steps in combination with the projection scheme, but in combination with the projected dihedral move method the diversification can be increased. For a more or less uncorrelated movement within the clusters the Cartesian move strategy seems to be sufficient. For the peptide test case this is not the case. In Figure 5.1.31 example pathways from a PO run with applied mix-move strategy are given to complete the picture.
A different approach to do sampling for additional structures around a pathway is to "exclude" the RC within a global optimization. It is based on the idea to identify the internals which change the most and freeze them out during the global optimization. The internal changes are identified on the basis of an initially calculated NEB pathway. Then in an automatic way the internals (dihedrals) are identified and atom positions are fixed for a global optimization procedure. The implementation of this procedure is related to the bachelor work of Julian Erdmannsdörfer[68]. He included the functions for identification of redundant internals into the NEB class and the related search functions for the largest changes. In addition, the fixations are carried out. His work was in close collaboration with me and

has been adopted and tested to work with the current CAST implementation. Related test calculations were carried out for the tridecaalanine test system. The influence on a MCM optimization by using a different number of fixation is shown for this case in Figure 5.1.32. The results are related to the run starting from the first NEB pathways structure. The procedure might be of interest if one has identified a TS via NEB method and then wants to investigate the chemical space around the TS to determine the kinetics.

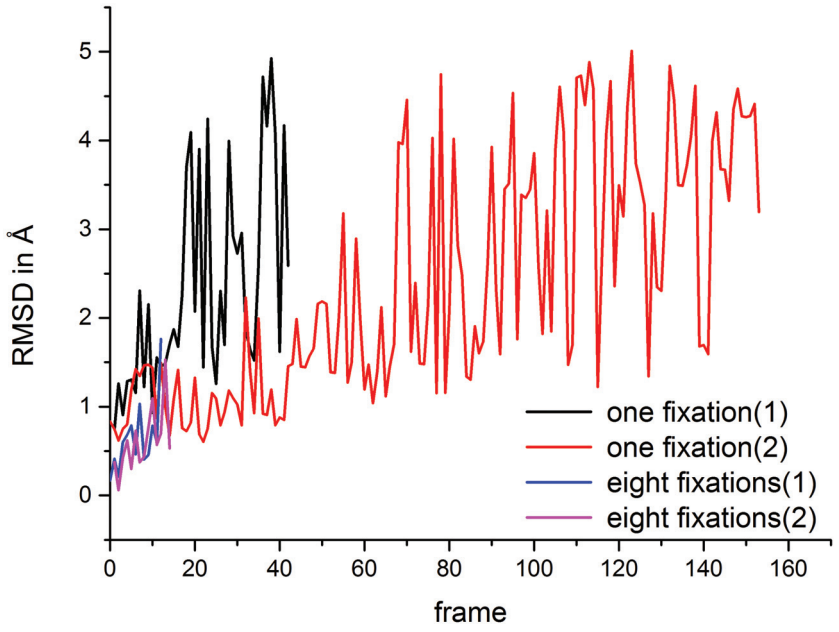

Figure 5.1.32: Resulting RMSD values in Å are given for structures which stem from MCM optimizations by using a different number of fixations. The results are related to optimizations starting from the first NEB structure.

Summary

For the applied test systems it was possible to show that the connection strategy which is functional in an automated way is able to treat various systems. Therefore, different clusters with different types of interactions were tested, starting from "simple" argon clusters and going ahead to a water cluster. It was possible to show that for the clusters the Cartesian move strategy in combination with the gradient projection scheme is a good choice. In addition it could be shown that the connection via RMSD criterion between the detected minima on the

hyperplane is able to give complete pathways and even deliver TSs and good guesses for them. By applying energy and RMSD criterion for the pathways it is also possible to identify the most relevant pathways and hence fore use them for further investigations. Moving forward to the description of real chemical reactions and describing large flexible molecules the move strategy was adopted in that way that the mixed move strategy was implemented. With this approach a faster diversification of the optimization on the concerning hyperplanes was reached which was not easily the case by using the Cartesian only strategy. In consequence, it can be stated that with PO and the different move and optimization strategies (gradient projection/bias potential) the ability is given to treat systems of different natures like large (bio)molecules, clusters and the proceeding reactions.

Chapter 6

Testing of AMOEBA09 polarizable force field gradients with short-range correction

6.1 Implementation of analytical Spackman gradients

The implementation of the AMOEBA09[5, 6] force field and the Spackman correction[69] for short-range electrostatics was already described within my master-thesis[70]. Within this part the implementation in the current version of CAST and inclusion of short-range electrostatics gradients is presented. Especially, the implementation of interpolated short-range electrostatics gradients are in the focus and the related testings. The class for calculating the AMOEBA09 energy has been adopted to the interface based implementation in the current CAST version. Within this process also the terms for describing short- range electrostatics were adopted. These short-range electrostatics and their implementation are described in [70, 71].

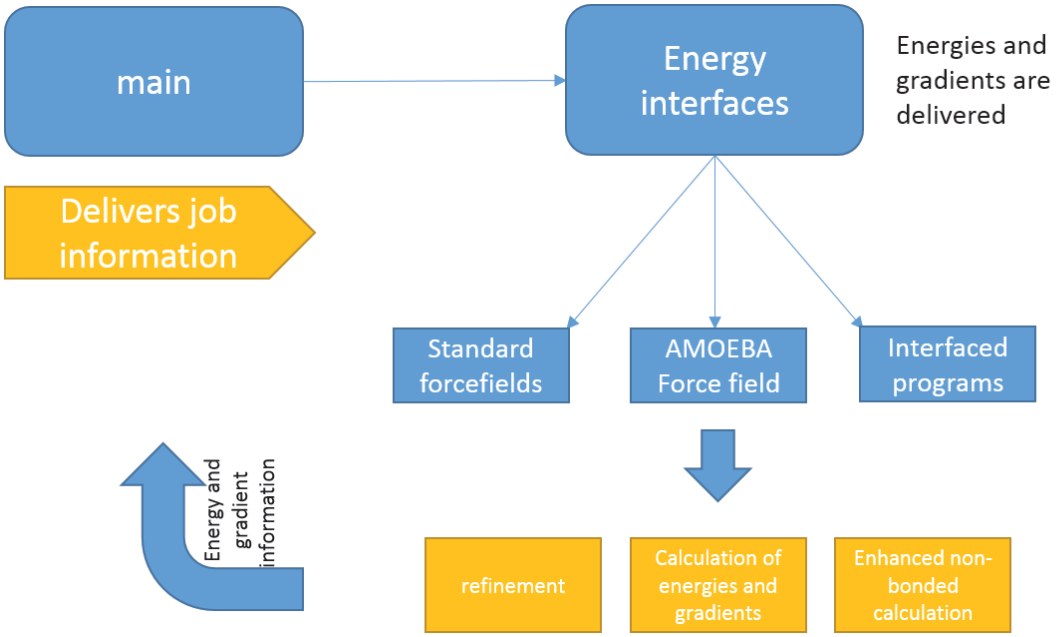

Figure 6.1.1: The schematic representation of the AMOEBA energy interface within CAST

For the description of the analytical gradients related to the short-range electrostatic correction two new functions were included and replace the old numerical calculation. Two different types of calculations exist. On the one side the function for the direct calculation, which would cause the evaluation of the integral based terms each time (numerically) and on the other side the calculation based on a list which includes pre-calculated values. This list is built for meaningful interaction distances between, in our case, hydrogen-hydrogen, carbon-hydrogen and carbon-carbon interactions. The short-range correction can be described by the following term

$$E_{es}^{a,b} = \frac{2}{\pi} \int_{\infty}^{0} \left[Z_a - f_a(s)/\kappa_a\right] \left[Z_b - f_b(s)/\kappa_b\right] j_0(sR) ds, \tag{6.1.1}$$

whereas only the term $j_0(sR)$ depends on the distance R. This term is the bessel function of zeroth order:

$$j_0(sR) = \frac{sin(sR)}{sR}. \tag{6.1.2}$$

Hence the derivative with respect to R is given by the bessel function of first order

$$j_1(sR) = \frac{sRcos(sR) - sin(sR)}{sR^2}, \tag{6.1.3}$$

which replaces than the zeroth order form in equation 6.1.1. As already mentioned to circumvent the demanding numerical calculation of the concerning integrals we addressed different interpolation strategies by using calculated gradients and energies lists.[70] Based on the new implementation of analytical and interpolated gradients, the speed up with respect to the numerical calculation is shown in Figure 6.1.2.

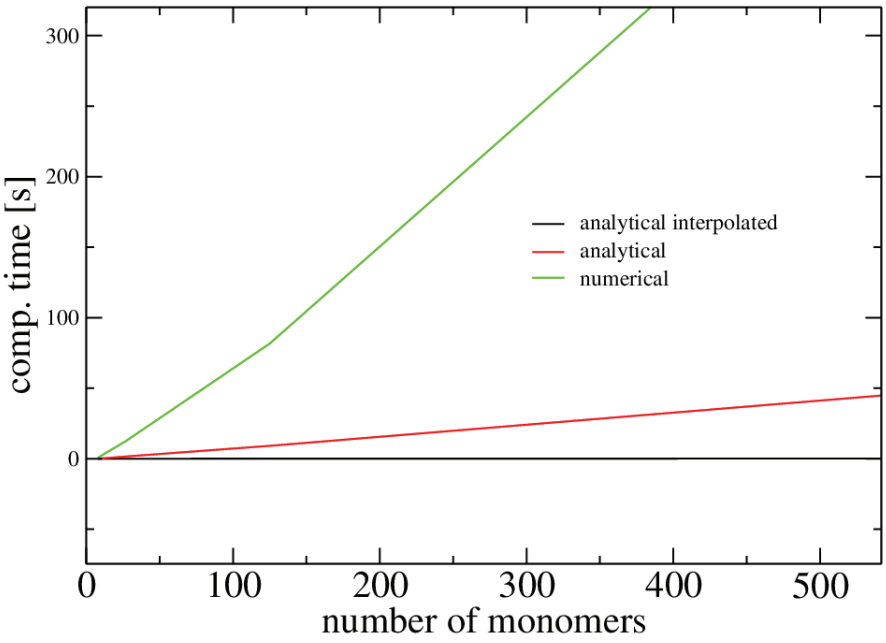

Figure 6.1.2: Computational times for one gradient step are shown for numerical gradient evaluation, the analytical and the interpolative one. The results for benzene clusters are shown (2-1000 monomers with 3.0 Å inter-monomer distance).

Nevertheless, the accuracy of the gradient calculation is only minimally reduced by the interpolation procedure. In the case of the 27 monomer benzene test system the difference in total RMSD for direct and interpolated scheme is for a local optimization only 0.27 Å. For evaluation of the accuracy capabilities of the new implemented force field several test calculations were performed. The test runs were performed on a workstation with AMD Phenom X6 1075T (3.0 GHz) processor and 8 GB DDR3 (1033 MHz) memory and using one thread.[70].

6.2 Calculations on benzene dimer and clusters

For testing the implementation, with the new AMOEBA gradients available test case calculations were done. Therefore, we choose benzene cluster systems which are widely investigated in literature. Given that the description of π-conjugated molecules is an important research field and one of the ideal test candidates for testing the capabilities of the new gradient implementation. Many studies have been performed around different benzene motifs and in focus of them often stands the interaction between π-systems. In a former publication[72] it was shown that the interaction energy between two benzene units in parallel and t-shaped orientation can be described in the right manner with the presented approach. For the application in the material science field also a larger scale is of interest. In this chapter test-calculations on benzene clusters of different sizes are presented. The used structures represent the global minima found by Hiroshi Takeuchi.[73] The structures were optimized with OPLS-AA force field and a global optimization was done by using a metaheuristic geometrical perturbation approach called (MHGP)[74]. For method validation we calculated local minima starting from the global minimum structures. The minimizations were done by using the L-BFGS[26, 27, 28, 29, 30, 31, 32] minimizer in the CAST program and were compared with obtained minimum structures from calculations on B3LYP[55, 56, 57, 58, 59]/TZVP[60] level with Grimmes dispersion correction (3rd generation)[75, 76] using the Turbomole 6.5[61] package. The DFT calculations were performed for the benzene clusters consisting from two monomers up to five. In addition to the described minima, also the global minimum described on the DFT/CCSD(T)[77] and CCSD(T)/CBS[78, 79, 80] level by a paper of Petr Nachtigall[81] is used for investigations. The optimized structures were calculated with PBE[55, 56, 82, 83, 84]/CCSD(T) which means that the interaction energy is corrected on the CCSD(T) level. For the comparison of the obtained structures, in both cases single point calculations on the CCSD(T)/XX level were done for the dimer systems.

6.2.1 Results on small clusters

First we want to present the results for the geometry optimization of the clusters from the dimer system up to the pentamer system. Optimizations were performed with the new described force field approach (SAPT-FF) and also with the standard AMOEBA09 force field. The OPLS-AA structures from Takeuchi are shown in Figure6.2.1.

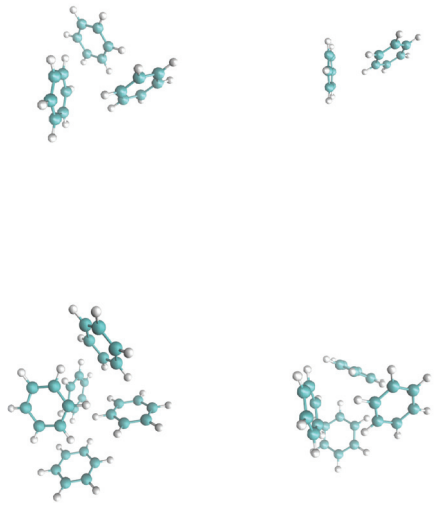

Figure 6.2.1: Starting structures from Takeuchi which were obtained via a global optimization scheme using the OPLS-AA force field.

After local optimization with a gradient threshold of about 0.001 on force field and DFT level, the obtained structures were compared. The RMSD values for the structures are shown in Table 6.1. From the obtained RMSD values it can be seen that the differences between the structures obtained with B3LYP-D3 and the starting structure on OPLS-AA level remain very small.

method	2	3	4	5
AMOEBA	0.13	0.25	0.13	0.54
SAPT-FF	0.07	0.12	0.06	0.20
OPLS-AA	0.06	0.12	0.05	0.14

Table 6.1: RMSD values are shown for a local optimization on the OPLS-AA global minimum structures from Takeuchi by using B3LYP-D3/TZVP. The values are calculated relatively to the B3LYP-D3 geometries. The OPLS-AA values are relatively to the Takeuchi structures.

This is the case for the dimer and the tetramer, the deviations for the trimer and pentamer are slightly larger. The same trend and more or less equal deviations are found with the new force field approach (SAPT-FF). The geometries obtained with the standard parameter set and the AMOEBA09 force field without correction vary more leading to a more or less doubled RMSD value. The obtained structures are shown for comparison in Figure 6.2.2.

These results shows that the gradient and energy implementation in our own program package is able to describe the geometrical properties with a good accuracy.

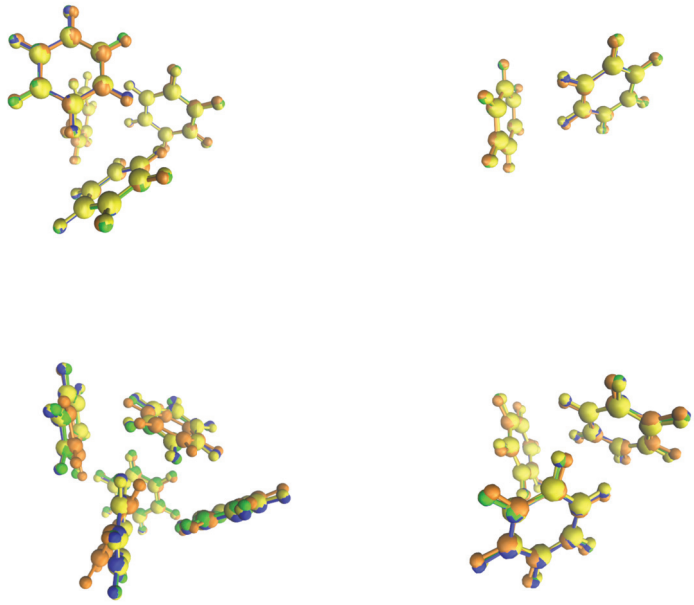

Figure 6.2.2: Optimized structures of benzene clusters from dimer up to pentamer. The B3LYP-D3 structures are shown in yellow, the OPLS-AA structures in blue, the AMOEBA structures in orange and the SAPT-FF structures in green.

Compared to the standard AMOEBA force field a significant improvement is obtained. Also the interpolation scheme for the correction scheme works, not only for the first mentioned benzene test systems. Regarding the single point energies on the CCSD(T)[77]/cc-pVDZ[85, 86] level of the dimer, the results show that the structure computed with the new force field approach is 3.18 kJ/mol stabilized compared with the B3LYP-D3/TZVP structure. The starting OPLS-AA structure is 4.71 kJ/mol more stable. This leads to the conclusion that within the accuracy of the CCSD(T) method of about 0.8 up to 2.0 kJ/mol the structures are more or less identical in terms of energy, although the global minimum OPLS-AA structure is slightly more stable. This is also represented in the small RMSD deviations. For further investigations MD simulations were done on the described cluster systems. These MD simulations were performed for the small clusters (2-5) and in addition also for the larger ones. The results for the small clusters and the cluster consisting 30 monomers are shown in the following. The MD simulations were taken for 0.1 ns simulation time and the step size

was set 0.001 *ps*. A heat bath was used with Nosé-Hover thermostat[87] and a temperature of about 50 K. In Figure 6.2.3 the energy distributions for the dimer up to the pentamer test systems are depicted. The given energies stem from optimized structures out of the MD simulation. For increasing system size the energy distribution is wider. This trend continues and is shown in Figure 6.2.4 for the largest test candidate (30 monomers).

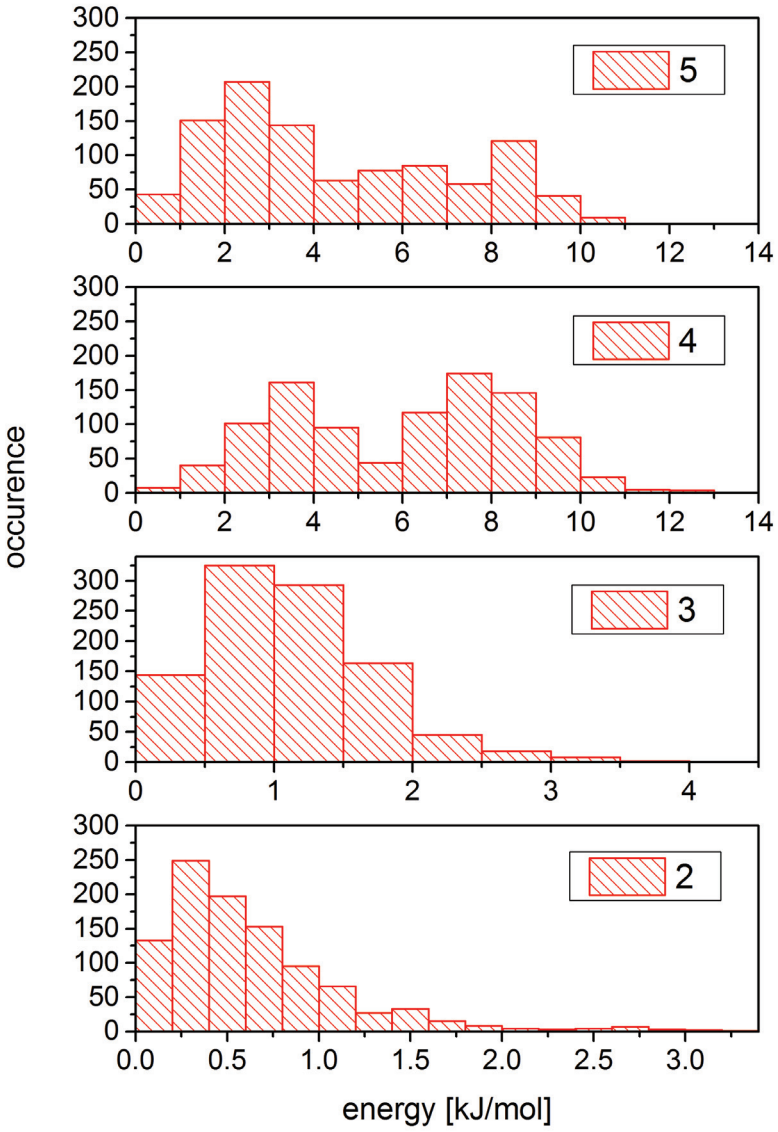

Figure 6.2.3: Energy distribution for a MD run at 50 K and 0.1 *ns*. The step size was set to 0.001 *ps*. The energies shown are the locally optimized frames of the MD run and their energies. The distribution is shown for the four different clusters in this figure (dimer(2) up to pentamer(5)).

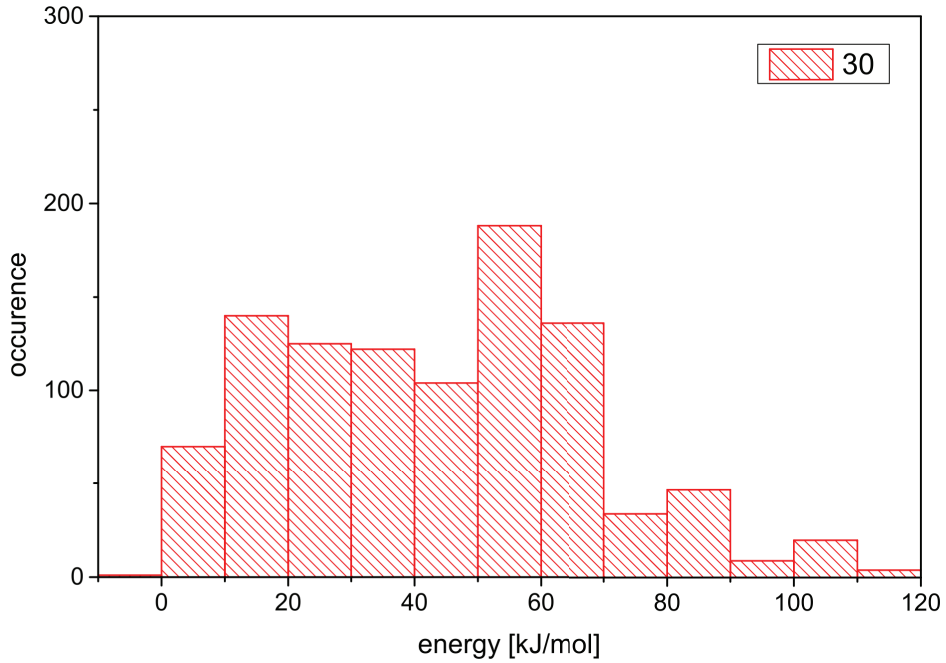

Figure 6.2.4: Energy distribution for a MD run at 50 K and 0.1 *ns* simulation time. The step size was set to 0.001 *ps*. The energies are the locally optimized frames of the MD run and their energies. The distribution is shown for the 30 monomers benzene cluster.

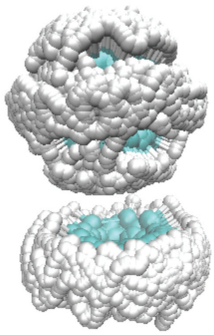

Figure 6.2.5: The overlaid structures from the MD-simulation at 50 K with the SAPT-FF of the dimer are depicted.

In the case of the dimer structure the inter-monomer distances for a MD simulation were investigated. The raw data is plotted in Figure 6.2.6 and the overlaid structures of the MD-simulation with the new SAPT-FF is depicted in Figure 6.2.5. The width of the distributions

is quite different. The distribution obtained with the SAPT-FF is much wider than with the OPLS-AA force field. From the probability plots the mean average distance for the optimized frames was calculated which is 4.94 Å for OPLS-AA and 4.87 Å for SAPT-FF.

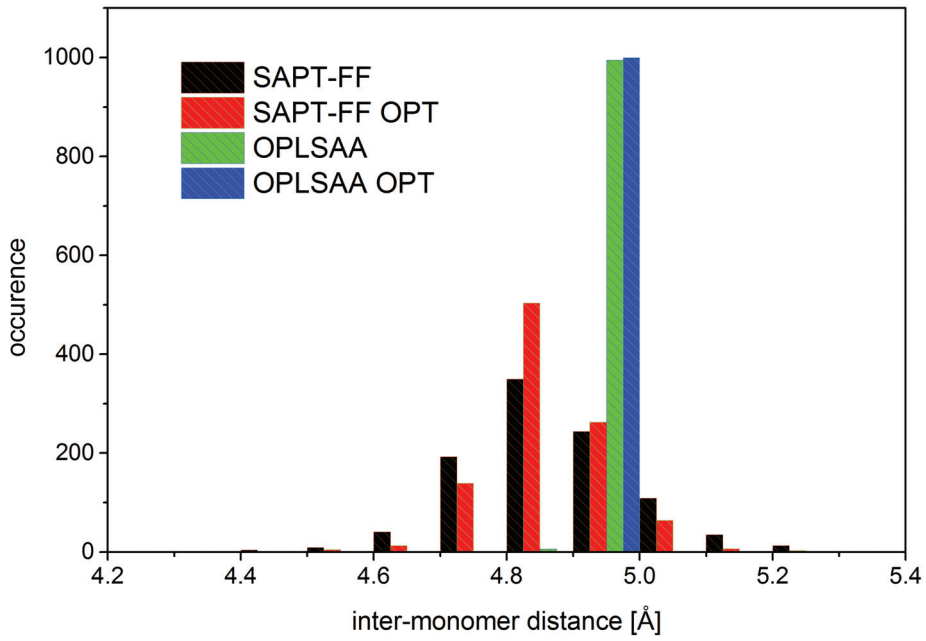

Figure 6.2.6: Distribution of the inter-monomer distances for The SAPT–FF and the standard OPLS-AA force field. The distances are shown for optimized- and MD-frames (50 K).

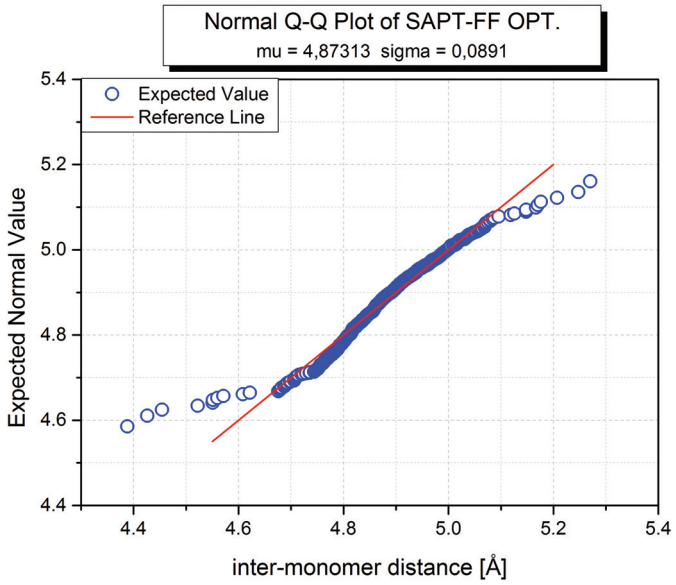

Figure 6.2.7: Probability plot for inter-monomer distances obtained with SAPT-FF by optimized MD-frames (50 K).

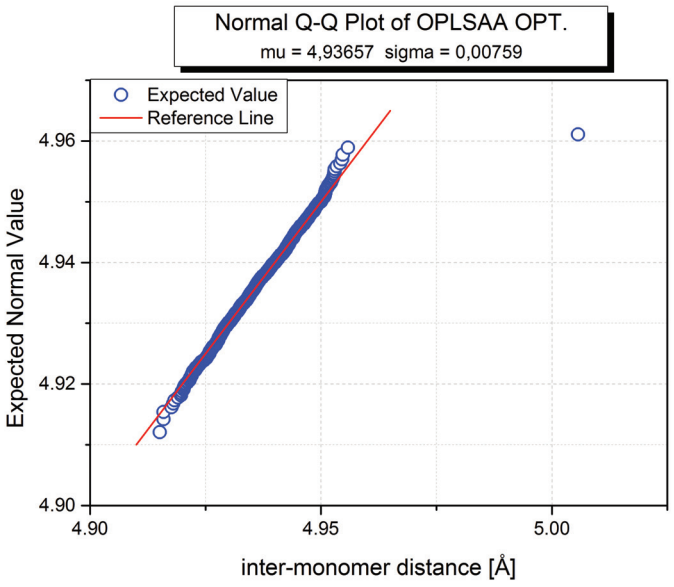

Figure 6.2.8: Probability plot for inter-monomer distances obtained with OPLS-AA by optimized MD-frames (50 K).

Also for the simulation at 200 K heat bath temperature the same trends occurred. The mean average distance for SAPT-FF and optimized frames is 4.94 Å and for OPLS-AA 4.95 Å.

In addition to the dimer MD simulation, the trimer results should also be presented in detail for SAPT-FF. The inter-monomer distances measured for the starting structure, which was optimized with the SAPT-FF, are more or less symmetric. All distances are of 4.89 Å. This is in a good agreement with a previous theoretical study[88] which predicts for this structure a center to center distance of 4.80 Å. In reference[89] the authors describe a benzene trimer structure found in a tripyrrolic crystal[90]. In this structure the inter-monomer distances are 4.973, 4.623 and 5.004 Å. In Figure 6.2.10 the distribution of the MD simulation is shown. Starting from the symmetric trimer structure during the simulation asymmetric structures are reached. The average distances from the simulation are 4.83 (1-2), 4.82 (1-3) and 4.63 Å (2-3).

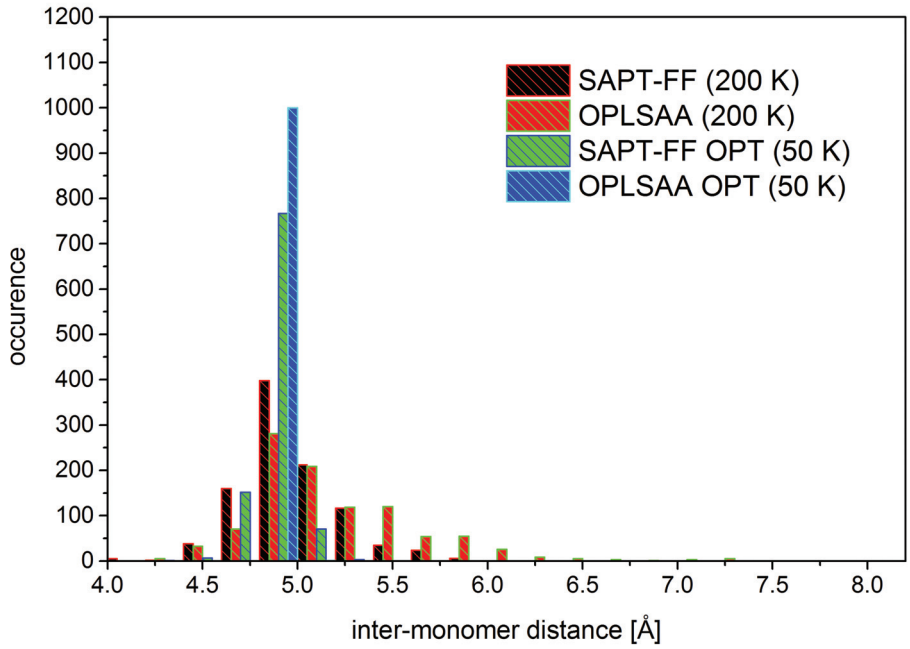

Figure 6.2.9: Distribution of the inter-monomer distances for The SAPT force field and the standard OPLS-AA force field. The distances are shown for optimized frames(200 K).

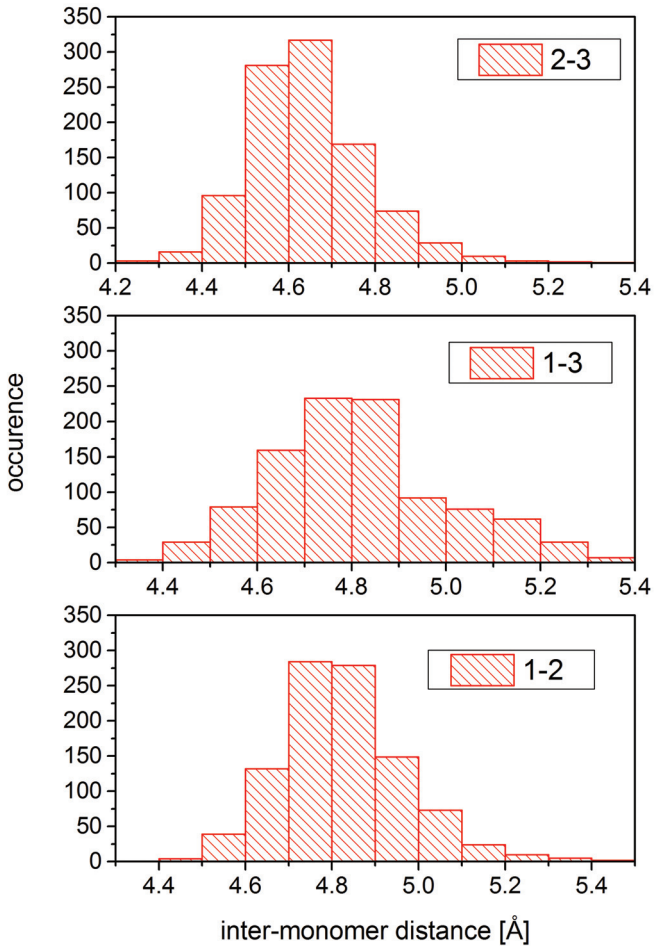

Figure 6.2.10: The distribution of the inter-monomer distances for the MD simulation of the trimer cluster are shown.

6.2.2 Benzene dimer calculations with respect to PBE/CCSD(T) dimer

In this part the results from the investigation of the global minimum structure obtained on the PBE/CCSD(T) level are presented. In a first step local optimized structures and their single point energies on CCSD(T)/aug-cc-pVDZ level are compared. The dimer structures from the OPLS-AA and from CCSD(T)/CBS study are slightly different. The structures are shown in Figure 6.2.11. The OPLS-AA structure is shown in red while the blue structure represents the minimum structure obtained with PBE/CCSD(T). The distance between the monomers

is 4.94 Å for the OPLS-AA one and 4.93 Å for CCSD(T). The OPLS-AA structure is slightly more stable than the PBE/CCSD(T) one. The RMSD between the two minimum structures is 2.78 Å. The energy difference on CCSD(T)/aug-cc-pVDZ level between SAPT-FF and OPLS-AA is of about 1 kJ/mol and the difference between OPLS-AA and PBE/CCSD(T) is 9 kJ/mol.

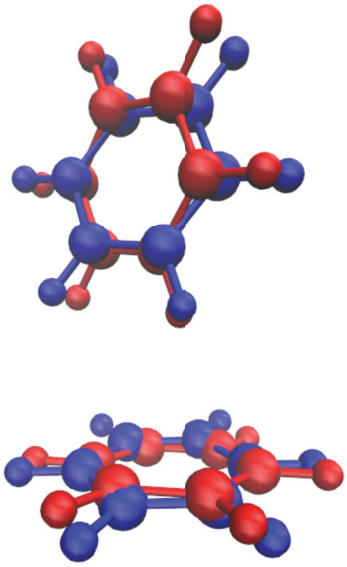

Figure 6.2.11: Comparison of the different dimer structures. Blue represents the PBE/CCSD(T) structure and the red one the structure from the Cluster study (OPLS-AA).

In a next step local optimizations starting from the PBE/CCSD(T) structure were performed. The optimized structures are depicted in Figure 6.2.12. The RMSD values are summarized in Table 6.2. OPLS-AA and the SAPT-FF perform very well in terms of total RMSD, while the standard AMOEBA force field performs worse in terms of accuracy. For the calculated inter-monomer distances larger deviations occur. The SAPT-FF delivers in this case the best agreement with the CCSD(T)/CBS structure, as depicted in Table 6.3.

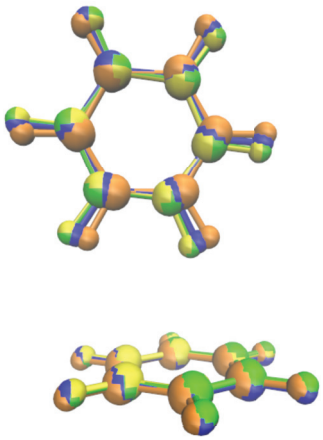

Figure 6.2.12: Optimized structures of the PBE/CCSD(T) benzene dimer are depicted. The PBE/CCSD(T) structure is shown in yellow, the OPLS-AA structures in blue, the SAPT-FF structure in green and the AMOEBA structure in orange.

Method	RMSD [Å] referenced to PBE/CCSD(T)
OPLS-AA	0.10
AMOEBA	0.21
SAPT-FF	0.02

Table 6.2: RMSD values in [Å] referenced to the CCSD(T)/CBS dimer structure.

Method	Distance between monomers in [Å]
OPLS-AA	5.01
PBE/CCSD(T)	4.93
SAPT-FF	4.92

Table 6.3: : The inter-monomer distances are shown for the PBE/CCSD(T) structure, SAPT-FF and OPLS-AA.

The relative energy differences for the cluster dimer and the PBE/CCSD(T) structure are listed in Table 6.4. The deviations are small in terms of energy, but the SAPT-FF delivers

the better structure in terms of inter-monomer distance, total RMSD (compared to the PBE/CCSD(T) structure). The OPLS-AA structure is slightly lower lying in energy after local optimization starting from the CCSD(T)/CBS structure. The comparison is made on basis of CCSD(T)/aug-cc-pVDZ single point calculations. Larger basis sets were not tested due to the computational effort. In addition, MD simulations were carried out for the PBE/CCSD(T) dimer. For the simulation with the SAPT-FF larger variations for inter-monomer distances occur. By optimizing the frames, the distribution width gets smaller. The average inter-monomer distance for the frames with OPLS-AA is 4.96 Å and for the SAPT-FF 4.91 Å.

Relative energies in [kJ/mol]	CCSD(T)/ TZVP	CCSD/ cc-pVDZ	CCSD(T)/ cc-pVDZ	CCSD/ aug-cc-pVTZ	CCSD(T)/ aug-cc-pVDZ
Cluster Dimer					
SAPT-FF	2.21	0.65	3.57	8.19	2.82
OPLS-AA	1.99	1.61	2.04	6.57	4.43
B3LYP-D3/TZVP	1.04	3.45	6.75	1.93	7.32
CCSD(T)/CBS structures					
OPLS-AA	4.29	0.42	0.00	14.22	0.00
SAPT-FF	0.00	0.00	1.23	5.83	1.00
PBE/CCSD(T)	0.82	5.70	9.70	0.00	10.39

Table 6.4: Relative energy differences for the optimized clusters starting at the cluster dimer and the CCSD(T)/CBS configuration are shown. The single point energies refer to the addressed methods and basis sets. The relative energies are column wise presented.

6.2.3 Global optimization of the cluster dimer configuration

A Tabu search optimization was performed for the cluster dimer starting structure. Therefore, 500 steps were carried out by applying the biased random dihedral move strategy. The optimization was carried out with the standard OPLS-AA or the new SAPT-FF. New y-shaped minimum structures were found and for the SAPT-FF, also additional orientations occurred. In Figure 6.2.13 the obtained minimum structures for the GOTS[62, 63, 64, 65] in the T-shaped or tilted motif are shown. The center-to-center distance for the OPLS-AA structure is 5.06 and for the SAPT-FF structure 4.80 Å.

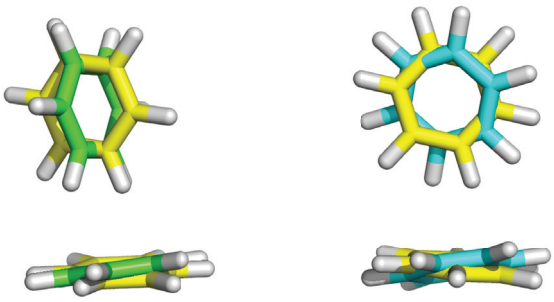

Figure 6.2.13: Obtained T-shaped and tilted minimum structures from a Tabu-Search run. In blue color, representation is the OPLS-AA and in green the SAPT-FF minimum shown. The structures are compared with the PBE/CCSD(T) structure in yellow.

The two structures obtained via optimization for each method are close in energy. The single point calculation on CCSD(T)/aug-cc-pVDZ shows that the OPLS-AA T-shaped structure is 2.32 KJ/mol more stable. In comparison with the dimer configuration obtained by optimization with OPLS-AA on top of the PBE/CCSD(T) dimer these two structures are slightly higher in energy (˜ 3 KJ/mol).

6.2.4 Summary

Within this part of the work it was shown that the improved gradient implementation of the SAPT-FF into the CAST program is able to handle the description of small benzene cluster system. Therefore, we addressed different clusters for benchmarking. It is remarkable that both SAPT-FF and OPLS-AA give trustworthy results and are able to reproduce the dimer structures obtained on PBE/CCSD(T) level. The SAPT-FF is a good improvement of the standard AMOEBA implementation which was shown. The low costs of force field methods in this context makes it possible to carry out global optimizations and predicting additional minimum structures. These minimum structures can then be characterized by higher order methods like in this case the CCSD(T)/aug-cc-pVDZ approach.

Chapter 7

Study on the flexibility of cyclic PBI derivatives with respect to AFM microscopy - the structure property relationship

Within this section the properties of acetylene linked PBI macrocycles should be discussed. Especially the flexibility of different sized rings is of interest. Therefore, our coworkers studied these macrocycles by atomic force microscopy (AFM). We were able to confirm their findings using MD simulation techniques in combination with a semi-empirical (PM6-DH2) approach.[91] In Figure 7.0.1 the different 1,6,7,12-tetraphenoxy-PBI macrocycles from a MD simulation in vacuum are depicted. We investigated the different ring sizes starting with a ring built up by three PBI monomers and the ending at the macrocycle built up by 6 PBI monomers. The AFM measurements were conducted by using spin-coated films of a 7.5 x 10^{-6} M onto a HOPG (highly ordered pyrolytic graphite) surface.

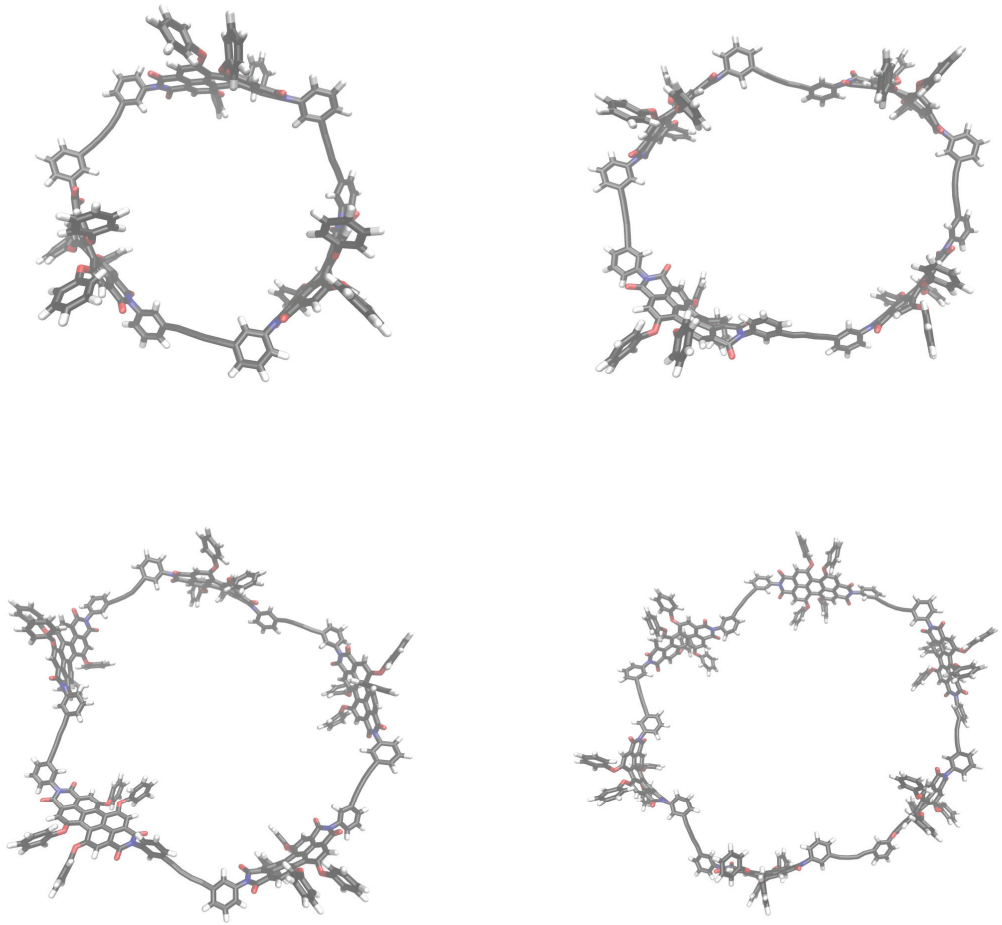

Figure 7.0.1: Typical snapshots from a PM6-DH2 MD simulation are depicted of the 1,6,7,12-tetraphenoxy-PBI chromophore of different ring sizes, three to six, which are bridged via acetylene units.

The observed structures and the degree of order is very different for the ring sizes (C3-C6). For the three-membered ring a hexagonal and clearly structured pattern (donut-like) was observed. For the four-membered ring structures AFM revealed a well ordered structure as well, whereas a rectangular motif was observed. For the larger macrocycles (5-6) no self-assembly behavior could be investigated. Hence, within our study we investigated how the self-assembly behavior can be explained from a molecular point of view. Therefore, in a first step the right choice of the underlying theoretical model is important. For the description of the flexibility of the different macrocycles MD simulations are a good choice. Within

MD simulation also the temperature-dependency can be simulated. Carrying MD simulation out even for the largest macrocycles restricted us to use computationally cheaper methods, because a full quantum-mechanical investigation would be very time-demanding. Therefore, we tested various classical force fields and semi-empirical approaches against standard DFT calculations on B3LYP[55, 56, 57, 58, 59]/6-311G**[92, 93, 94, 95] level of theory. To keep the calculations feasible within a meaningful time we decided to focus on a simplified model system and investigated different torsion and bending angles. In Figure 7.0.2 OPLS-AA[42, 39, 40], MM+[96, 97], AMBER[98] and PM6-DH2[53, 67]/MOZYME(localized molecular orbitals)[99] potentials in kcal/mol for the bending of the linker between two PBI units is shown. The strongest deviations from the B3LYP curve is obtained by the OPLS-AA description which strongly overestimates the bending energy for larger deflections.

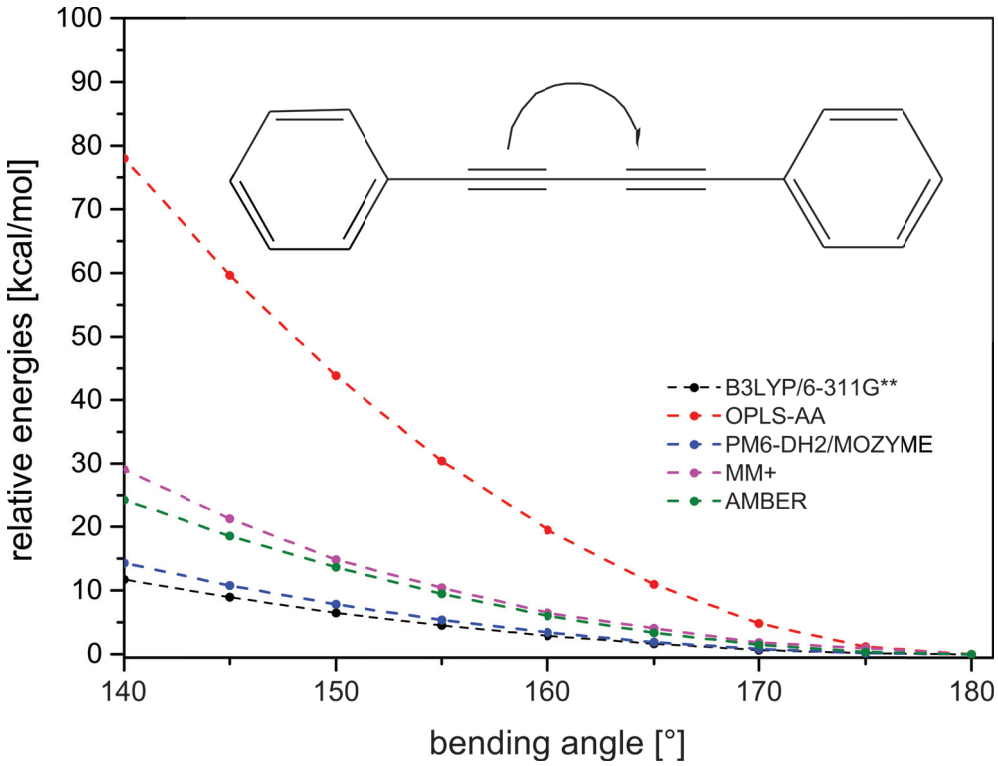

Figure 7.0.2: The relative energies for bending the acetylene linker unit is shown for different computational methods.

Also the other force fields overestimate the energies but are better in their description (MM+,AMBER). This fact is not surprising that within the classical description without inclusion of higher order effects (only quadratic function) for large displacement from the equilibrium angle the energy rises tremendously. Nevertheless the PM6-DH2 (if PM6-DH2 is

mentioned in this chapter than we refer to the usage of the MOZYME approximation) method seems to be the best choice. The same observation can be obtained, looking at the torsional motion of the PBI unit relatively to the linker. In Figure 7.0.3 the comparison between classical force field (OPLS-AA), PM6-DH2 and B3LYP is drawn. By having a closer look on the smaller torsions (see Figure 7.0.4) the differences between the methods are below the methods reliability. We also tested other semi-empiric approaches, but kept with the PM6-DH2 method because of the inclusion of dispersion, as well as explicit hydrogen bonding corrections. These corrections might be important for the description of the inter-monomer interactions of the concerning PBI units.

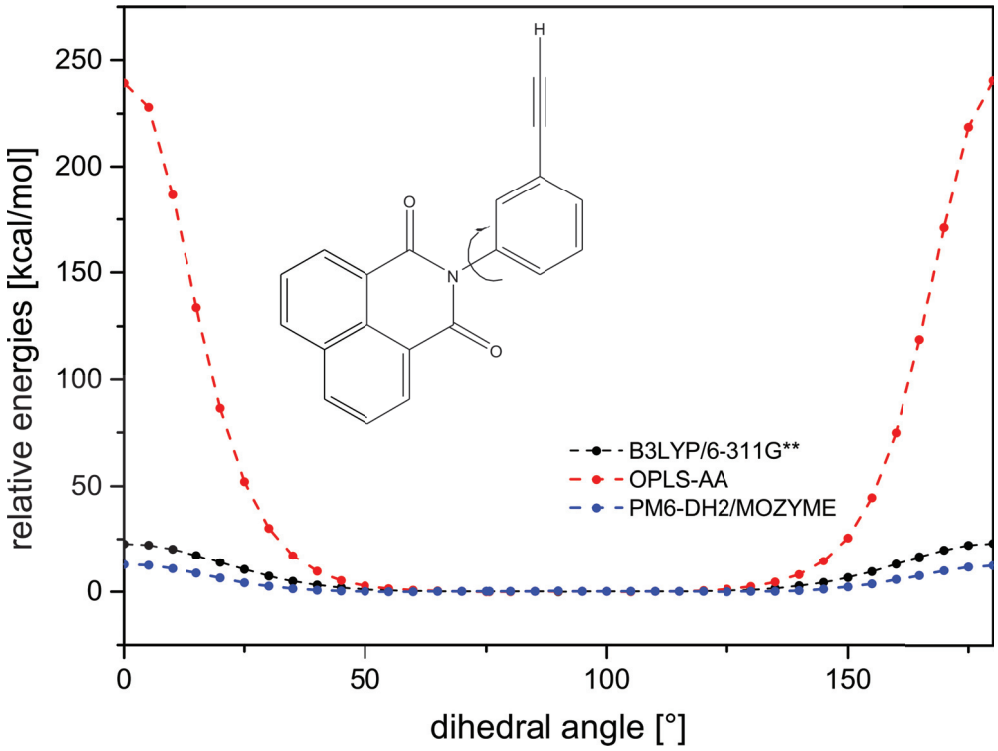

Figure 7.0.3: The relative energies for the rotation of the naphthalene mono-imide unit with respect to the linker unit is shown for different computational methods.

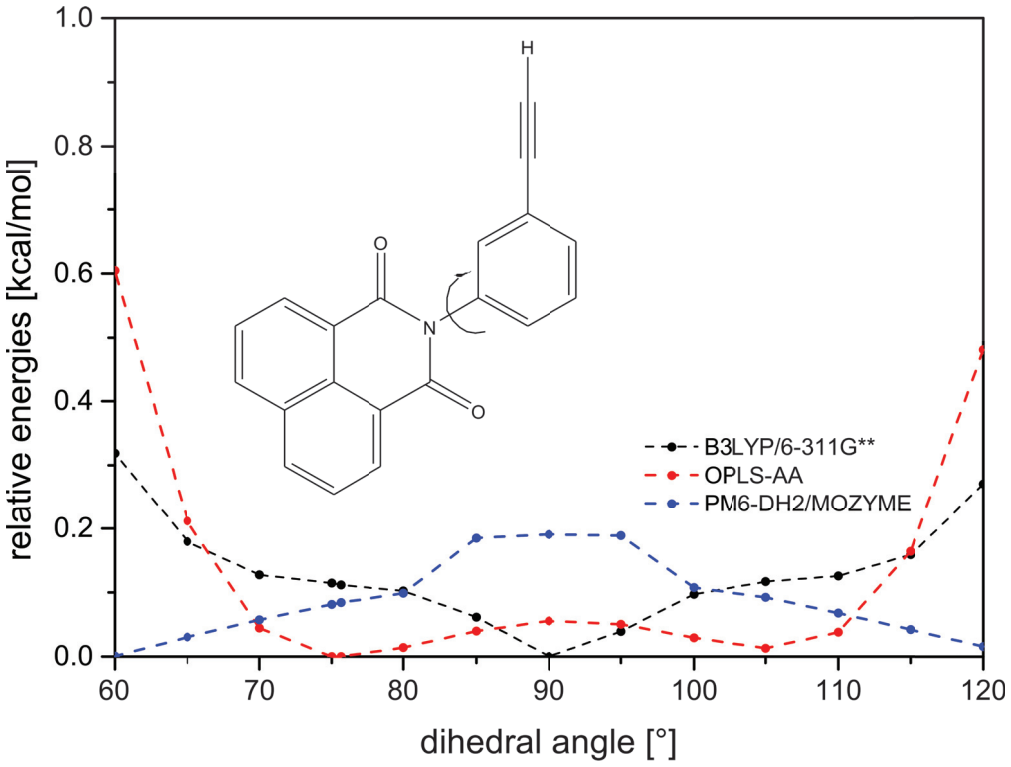

Figure 7.0.4: The relative energies for the rotation of the naphthalene mono-imide unit with respect to the linker unit is shown for different computational methods. The angles in the region of about 60°to 120°are shown.

Besides MD simulations we constructed different conformers (C3-C6) and compared the relative energies of the optimized species (PM6-DH2). Within these calculations we omitted the phenoxy substituents. As the benchmark investigation shows, a rotation around the [phenyl]C-N(PBI) bond posses a small barrier of around 6 kcal/mol. Therefore, it is interesting to investigate all possible conformers and if for larger rings the *trans* configurations become energetically reachable and more stable. The optimization of the all *cis* conformation leads to the most stable one for the trimer (C3), but for larger rings the various trans configurations lead to the preferred structures. The energies for the different *cis-trans* conformers are summarized in Table 7.1. For the tetramer (C3) the configuration with one *trans* configuration (tcc) is 8.7 kcal/mol higher in energy while the all *trans* lays 12.7 kcal/mol higher. For the hexamer the two *trans* configuration (tctccc) is the most stable one.

C3		*C4*		*C5*		*C6*	
a	b	a	b	a	b	a	b
ccc	0.0	tctc	0.0	tttcc	0.0	tctccc	0.0
tcc	8.7	ttcc	1.4	ttccc	0.4	ttttcc	0.6
ttc	14.0	cccc	1.9	tctcc	0.5	tttccc	1.0
ttt	12.7	tttc	2.9	ccccc	1.1	tccccc	1.2
		tccc	3.1	ttttc	1.4	tcctcc	1.8
		tttt	4.3	tcccc	1.9	ttcccc	2.0
				ttctc	2.2	cccccc	2.7
				ttttt	3.4	ttctcc	2.6
						tctctc	2.5
						ttcttc	2.8
						tttttc	3.2
						tttttt	3.2
						tttctc	3.5

Table 7.1: The relative energies of the optimized structures obtained by using the PM6-DH2 approach are depicted. [a]used starting structures ordered with respect to their sequence of cis (c) and trans (t) orientation relative to the acetylene linker. [b]relative energies given in kcal/mol. C3-C6 is indicating the number of monomer units.

In Figure 7.0.5 the optimized structures related to the energies summarized in Table 7.1 are given. The minimum structure of the trimer (C3) posses the feature that two PBI units are perpendicular relatively to the linker unit, but one stays in plane. This might be related to the rigidity of the small ring. Nevertheless, the barrier is not very high so the fact that on the HOPG substrate all PBIs are flat on the surface is explainable and is mediated by $\pi - \pi$ interactions. The $S_0 \rightarrow S_1$ is polarized along the long molecular axis and hence the optical properties are not affected by the rotational motion. For the tetramer the most stable configuration is the tctc structure. The next higher lying structure is the ttcc one which is around 1.4 kcal/mol higher in energy. In fact the population in thermodynamic equilibrium of this conformers is by around 10%. The all *cis* structure is even higher in energy. As already mentioned due to the relatively flat potential for the rotation the phenyl rings and the PBIs are not orthogonal to each other. The tetramer is indeed not really flat compared with the trimer. Nevertheless, the interactions with the HOPG surface might flatten it again which is proven by the AFM pictures. Here, ordered domains of large sizes with a square lattice are obtained.

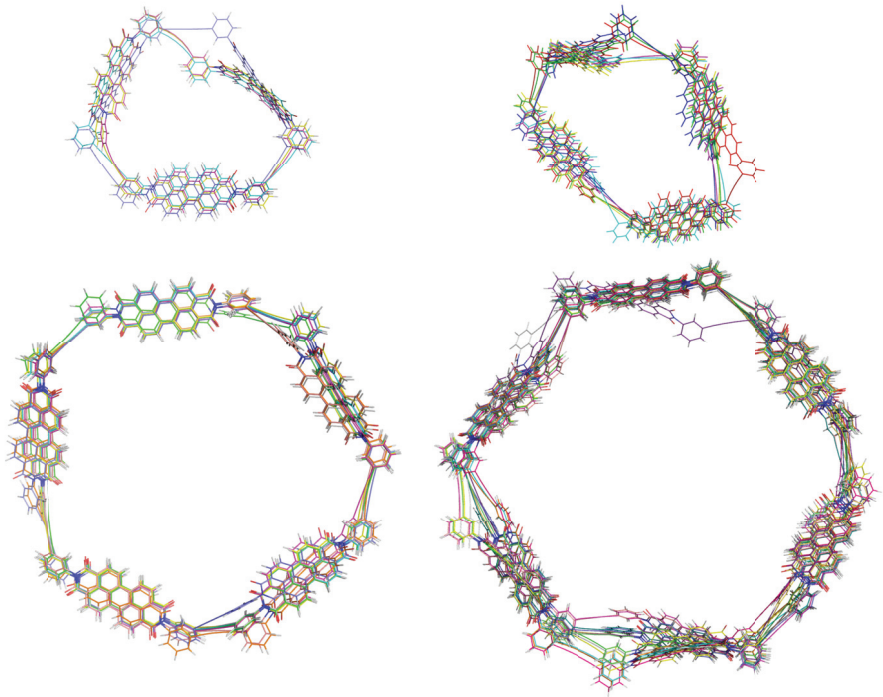

Figure 7.0.5: For different ring sizes the optimized structures (C3-C6) of different *cis-trans* conformers are shown. The related energies and different configurations are summarized in Table 7.1.

The optimization of the different pentamer conformers leads to five structures which are in a range of less than 2 kcal/mol. These minima differ less with respect to each other and the acetylene linker shows *cis* configuration. For C6 three quite similar conformers are obtained, but they possess both *cis* as well as *trans* orientations. In fact, for C5 and C6 a zigzag-crown like structure is found. The presented calculations underpin the fact that the larger the rings are the more flexible they become and that the trimer and the tetramer are represented by well separated conformers due to the larger barriers. By increasing the ring size (C5 and C6) the optimization lead to more similar structures, due to the smaller barriers.

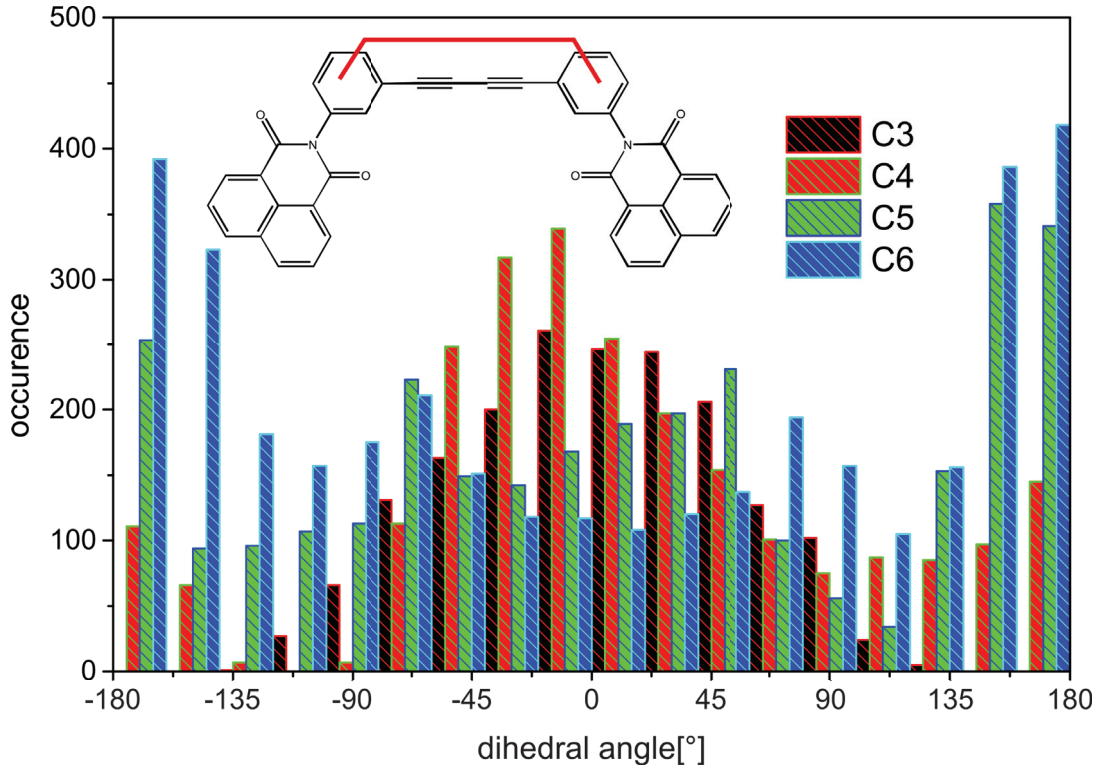

Figure 7.0.6: The distribution of the indicated dihedral angle (rotation around the linker) is shown for MD simulations of the various macro cycles. The energy describing method is PM6-DH2, whereas the ring size increases from C3 to C6.

We were able to show within our model calculations that we can explain some features of self-assembly. Nevertheless, the influence of the phenoxy substituents was not included and only a small number of molecules were generated by hand. Therefore, we performed MD simulations (vacuum) at different temperatures of the complete system by inclusion of the phenoxy substituents. The results of the 300 K simulation are given in Figure 7.0.6 which shows the probability distribution of the dihedral angle between the PBI units. It can be seen that with increasing ring size the flexibility is higher. For the smallest system, namely the C3 rings, only angles in the range of ± 130° occur. Hence, for C3 only fluctuations around the all-*cis* form can be seen. For C4 a higher flexibility is examined and dihedral angles larger than 130° can occur. A strong increase of angles around 180° is obtained. Although the flexibility increases flat conformers are still favored. For the larger ring systems (C5 and C6) this changes and dihedral angles of 180° are dominant within the overall distribution. Hence non-planar configurations are reached, as one can see in Figure 7.0.7, as it was already discussed for the locally optimized structures.

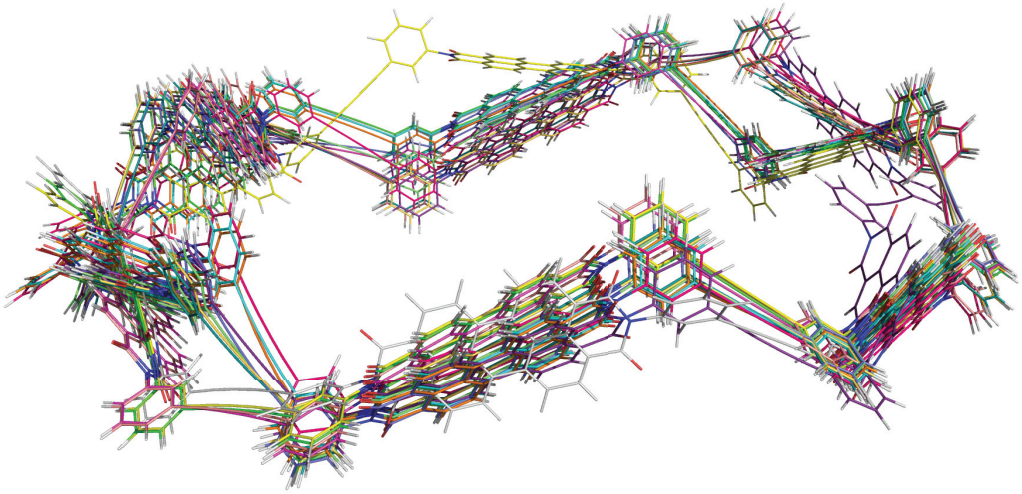

Figure 7.0.7: The overlayed structures which were obtained via optimization of constructed conformers of the C6 ring system is shown as a side view.

Our computations explain the absence of ordered domains for C5 and C6. The increased flexibility reduces the possible attractive interactions with the HOPG substrate. Furthermore, an increased entropic penalty exists for reducing the system to one single conformation on the substrate. This describes the structural features which were detected by AFM and give some insight into related spectroscopy and single-molecule spectroscopy data. Within the experiments a broadening of e.g. the Fluorescence lifetime occurs with increasing ring size.[91]

Chapter 8

Effects of the environment on photo-physical processes in perylene dyes

8.1 Description of environmental effects on excited states

The accurate description of molecules in vacuum can be already a challenging task. But taking the description of the surrounding into account and mimicking a more realistic situation is even more demanding. A main focus of the research today deals with such projects like condensed phase systems, or ligand enzyme interactions, to give but two examples. Both examples deal with systems which are mostly built up by distinct molecules so the molecular description is needed. In that manner a good description of the molecule(s), the surrounding and their coupling is needed, because gas phase properties may change due to solvent-solute interactions.[100] One way to include the environment within calculations is founded on the idea of a partitioning scheme which divides the whole system into subsystems. One small part which is the most relevant for chemistry or physics (e.g the chromophore) is treated quantum mechanically while the influence of the surrounding is taken into account by atomistic force fields (QM/MM).[101, 102, 103, 104, 105] The advantage of these approaches is the fully atomistic treatment of the surrounding and the direct answer by structural changes is incorporated, for example. But these methods also have some drawbacks related to statistics. Therefore, often simulation times and convergence issues are the limiting factors. For example the situation of a solute in a solvent, which is embedded in a surrounding which fluctuates more than a protein environment and is less ordered might be better described by

other approaches, for example continuum solvation models(CSMs).[106, 107, 108, 109, 110]

8.1.1 The standard polarizable continuum model (PCM) approaches

The basic PCM & the Conductor like screening model (COSMO)

In its original formulation PCM (polarizable continuum model) was meant to be a QM only method for treating isolated molecules within solution (single type of solvent).[106] The approaches summarized within the PCMs are the oldest methods belonging to the class of apparent surface charge (ASP) methods. The effective Hamiltonian within the PCM description is defined by the coordinates of the solute only and can be addressed like in the following,

$$\hat{H}_{total}(r_{solute}) = \hat{H}_{solute}(r_{solute}) + \hat{H}_{solv-solute}(r_{solute}). \tag{8.1.1}$$

The total Hamiltonian is described by the sum of the solute Hamiltonian plus the Hamiltonian which describes the electrostatic interactions between the solute and the solvent. The electrostatic interaction is based on the idea that a continuous charge distribution σ is generated on the surface of a cavity which is built up due to the solutes structure. The surface charges are generated by using the boundary condition for the transition between the cavity surface and the dielectric continuum. At the cavity surface the electric permittivity changes from 1 to ϵ for the external space which induces a jump of the derivative of the total electrostatic potential $V(s)$. The charge distribution $\sigma(s)$ is given by

$$\sigma(s) = \frac{\epsilon - 1}{4\pi} \left(\frac{\partial V(s)}{\partial \vec{n}} \right)_{outer} = \frac{\epsilon - 1}{4\pi\epsilon} \left(\frac{\partial V(s)}{\partial \vec{n}} \right)_{inner}. \tag{8.1.2}$$

$V(s)$ is the total electrostatic potential. For the polarization vector and systems built up by subsystems of constant isotropic permittivity the vector depends on the gradient of the total electrostatic potential:

$$P_i(r) = -\frac{\epsilon_i - 1}{4\pi} \frac{\partial V(s)}{\partial \vec{n}}. \tag{8.1.3}$$

The polarization vector $P_i(r)$ is defined for a region i with its dielectric permittivity ϵ_i. At the boundary between two regions the charge distribution is given as

$$\sigma(s)_{ij} = -(P_i - P_j) \cdot \vec{n}_{ij} \tag{8.1.4}$$

and at the boundary between the cavity surface and the solvent it is given as:

$$\sigma(s) = -\left\{P(r)\cdot\vec{n}\right\}_{outer}. \tag{8.1.5}$$

The apparent surface charges (ASC), or better the resulting potential V_σ interacts with the real charges of the solute. This potential is called solvent reaction potential. The ASC is described due to the response of the solvent by

$$Q(s) = -\int_s ds' A^{-1}(s,s')V_\sigma(s'), \tag{8.1.6}$$

whereas A denotes the kernel function of the given PCM. For the solvent reaction potential one half of it gives a contribution to the systems energy, whereas the computed energy is a free energy.[107, 109]
The effective solvation potential for a given solute can be expressed by introducing two operators. One of them is the measure of the solute potential on the cavity surface ($\hat{V}(s)$) and the other one related to the measure of the surface charge $\hat{Q}(s)$. In this manner the potential is given with respect to the solute and its wave function ($|\Psi_M\rangle$) by

$$\hat{V}\left\{|\Psi_M\rangle\right\} = \int_s ds \left\langle \Psi_M \left| \hat{Q}(s) \right| \Psi_M \right\rangle \hat{V}(s), \tag{8.1.7}$$

whereas M is the enumerator for the given electronic state. Accordingly to literature[108, 111] we use a shorthand notation and the integral is replaced by a vector dot product which can be seen as a summation over finite elements. Hence the solvation potential $\hat{V}\left\{|\Psi_M\rangle\right\}$ is dependent on the wave function and a non-linear Schrödinger equation (SGE) is obtained (within the simplified notation):

$$\left\{\hat{H} + \left\langle \Psi_M \left| \hat{Q} \right| \Psi_M \right\rangle \cdot \hat{V} \right\} |\Psi\rangle = E_M |\Psi\rangle . \tag{8.1.8}$$

A difference exists between the eigenvalue E_M and the free energy of solvation. This difference is related to the work needed for creating the surface charges on the cavity and is defined as

$$-\frac{1}{2}\left\langle \Psi_M \left| \hat{Q} \right| \Psi_M \right\rangle \left\langle \Psi_M \left| \hat{V} \right| \Psi_M \right\rangle . \tag{8.1.9}$$

Therefore, Equation 8.1.8 can be modified and one obtains the free energy expression for the reference state:

$$G_M = \left\langle \Psi_M \left| \hat{H} \right| \Psi_M \right\rangle + \frac{1}{2} \left\langle \Psi_M \left| \hat{Q} \right| \Psi_M \right\rangle \left\langle \Psi_M \left| \hat{V} \right| \Psi_M \right\rangle . \tag{8.1.10}$$

If Equation 8.1.8 is solved self-consistently then the condition is full filled that solute and solvent are in equilibrium. This is a sufficient description for long living states such as the ground state. For vertical excitations the nuclei of the solvent cannot follow the fast electronical change and only the change of the polarizability can be seen as an immediate response. The nuclei are kept fix and remain in the configuration of the reference state (M). The new populated state will be denoted by $|\Psi_N\rangle$. For a distinction between non-equilibrated and equilibrated the reference state will be given by $\left|\Psi_{M_{eq}}\right\rangle$. To describe both situations (slow/fast) the response of the solvent is split. The response in terms of nuclear degrees of freedom is described by the slow response, whereas the fast term represents the electronically adoption of the solvent. Within this description the slow part stays equilibrated and only the fast one adopts to the target state ($|\Psi_M\rangle$). In this manner, the adoption to the non-linear SGE can be made

$$\left\{ \hat{H} + \left(\left\langle \Psi_{M_{eq}} \left| \hat{Q}_{slow} \right| \Psi_{M_{eq}} \right\rangle + \left\langle \Psi_N \left| \hat{Q}_{fast} \right| \Psi_N \right\rangle \right) \hat{V} \right\} |\Psi_N\rangle = E_N |\Psi_N\rangle , \tag{8.1.11}$$

whereas the surface charge operator is divided into a fast $\hat{Q}_{fast}$ and a slow part $\hat{Q}_{slow}$. Hence the expression for the free energy is

$$\begin{aligned} G_{N(noneq)} = {} & \langle \Psi_N | \hat{H} + \left(\left\langle \Psi_{M_{eq}} \left| \hat{Q}_{slow} \right| \Psi_{M_{eq}} \right\rangle + \left\langle \Psi_N \left| \hat{Q}_{fast} \right| \Psi_N \right\rangle \right) \hat{V} |\Psi_N\rangle \\ & - \frac{1}{2} \left\langle \Psi_{M_{eq}} \left| \hat{Q}_{slow} \right| \Psi_{M_{eq}} \right\rangle \cdot \left\langle \Psi_{M_{eq}} \left| \hat{V} \right| \Psi_{M_{eq}} \right\rangle \\ & - \frac{1}{2} \left\langle \Psi_N \left| \hat{Q}_{fast} \right| \Psi_N \right\rangle \cdot \left\langle \Psi_N \left| \hat{V} \right| \Psi_N \right\rangle . \end{aligned} \tag{8.1.12}$$

The direct use of Equation 8.1.11 and its self consistently solving for every state concerned might be not the best case in terms of calculation time as well as by the fact of introducing dependencies between higher excited state, whereas the linear independence should be ensured. In practice, a perturbative approach is often used. Therefore, Equation 8.1.8 is solved for each state concerned and the additional terms due to Equation 8.1.11 are added as perturbative corrections. In consequence, the free energy of state M is given by the eigenvalue

from Equation 8.1.8 plus the corrections as follows:

$$\begin{aligned} G_{N(noneq)} = & E_M \\ & - \frac{1}{2} \left\langle \Psi_{M_{eq}} \left| \hat{Q}_{slow} \right| \Psi_{M_{eq}} \right\rangle \cdot \left\langle \Psi_{M_{eq}} \left| \hat{V} \right| \Psi_{M_{eq}} \right\rangle \\ & + \frac{1}{2} \left\langle \Psi_N \left| \hat{Q}_{fast} \right| \Psi_N \right\rangle \cdot \left\langle \Psi_N \left| \hat{V} \right| \Psi_N \right\rangle \\ & + \frac{1}{2} \left\langle \Psi_{M_{eq}} \left| \hat{Q}_{fast} \right| \Psi_{M_{eq}} \right\rangle \cdot \left\langle \Psi_{M_{eq}} \left| \hat{V} \right| \Psi_{M_{eq}} \right\rangle \\ & - \left\langle \Psi_{M_{eq}} \left| \hat{Q}_{fast} \right| \Psi_{M_{eq}} \right\rangle \cdot \left\langle \Psi_N \left| \hat{V} \right| \Psi_N \right\rangle . \end{aligned} \tag{8.1.13}$$

The uncorrected excitation energy with respect to the equilibrated reference state Ψ_M is

$$\Delta E_{M_{eq},N} = E_N - E_{M_{eq}}, \tag{8.1.14}$$

with

$$E_{M_{eq}} = \left\langle \Psi_{M_{eq}} \right| \hat{H} + \left\langle \Psi_{M_{eq}} \left| \hat{Q} \right| \Psi_{M_{eq}} \right\rangle \cdot \hat{V} \left| \Psi_{M_{eq}} \right\rangle . \tag{8.1.15}$$

The free energy difference for the vertical excitation can be written as

$$\begin{aligned} \Delta G_{M_{eq},N} = & \Delta E_{M_{eq},N} \\ & + \frac{1}{2} \left(\left\langle \Psi_N \left| \hat{Q}_{fast} \right| \Psi_N \right\rangle - \left\langle \Psi_{M_{eq}} \left| \hat{Q}_{fast} \right| \Psi_{M_{eq}} \right\rangle \right) \\ & \left(\left\langle \Psi_N \left| \hat{V} \right| \Psi_N \right\rangle - \left\langle \Psi_{M_{eq}} \left| \hat{V} \right| \Psi_{M_{eq}} \right\rangle \right) , \end{aligned} \tag{8.1.16}$$

under the assumption that

$$\left\langle \Psi_{M_{eq}} \left| \hat{Q}_{fast} \right| \Psi_{M_{eq}} \right\rangle \cdot \left\langle \Psi_N \left| \hat{V} \right| \Psi_N \right\rangle = \left\langle \Psi_N \left| \hat{Q}_{fast} \right| \Psi_N \right\rangle \cdot \left\langle \Psi_{M_{eq}} \left| \hat{V} \right| \Psi_{M_{eq}} \right\rangle \tag{8.1.17}$$

holds true.[112] For COSMO this equality is formally exact. Up to this point only the slow response of the reaction field was included. To go further one can use linear response theory to obtain an additional contribution in the description. These terms which occur are transition moments between different states.

The COSMO kernel

Within the COSMO or (CPCM) approach the solute is embedded in an ideal conductor which is defined by its dielectric permittivity of infinity. The calculation of the effective surface charges is defined as (for the ASC description see Equation 8.1.6)

$$Q_n = -f(\epsilon) \sum_m (A^{-1})_{nm} V_m, \tag{8.1.18}$$

whereas the Kernel function A is defined according to Klamt et al.[113]. For the outer diagonal parts of the interaction matrix between the unit charges the definition of A is as follows:

$$A_{nm} = \frac{1}{s_n - s_m}. \tag{8.1.19}$$

For the diagonal parts which are related to self interacting unit charges the kernel is given by:

$$A_{nn} = 3.8\sqrt{S_n}. \tag{8.1.20}$$

Within the equations a small s resembles the position of discrete small segments with a constant charge density σ_n and capital S stands for the segment area. The dielectric permittivity which is the character of the modeled surrounding is used as a scaling factor in Equation 8.1.18 and is defined by the empirical dielectric permittivity of the medium

$$f(\epsilon) = \frac{\epsilon - 1}{\epsilon + \alpha}, \tag{8.1.21}$$

with α a constant which is is normally set to 1/2, but also different values were chosen within the existing implementations, e.g $\alpha = 0$. According to literature the error made within this model is small and of about 10 %.[114] For the treatment of excitation processes the surface charge operator has to be divided into a fast and a slow component (see above). Therefore, within the COSMO model an additional scaling factor is introduced f_{fast}. In consequence, two scaling factors are used: For fast processes $f_{fast} = f(n^2)$ and the slow one is given by $f_{slow} = f(\epsilon) - f(n^2)$. Within the definition of the fast component n is the refractive index and at the high frequency limit ϵ is $\lim_{\epsilon \to \infty} n^2$.

8.2 Excited state properties of PBI and PTCDA with respect to the role of the surrounding

8.2.1 Introduction

The inclusion of the environment in accurate calculations of excited states in combination with a proper investigation of the important molecular degrees of freedom might be crucial. Within this study we applied Continuum Solvation approaches as well as embedding schemes

based on point charge interactions to model isotropic and anisotropic media to some extent. The systems of interest are PTCDA and PBI aggregates and their thin films. In combination with simulations of relaxation processes from a neutral to a zwitterionic dimer system we were able to show that an isotropic medium does not strongly influence the order of the four dimer excitations found in vacuum. By applying different models for crystal like environments within a QM/MM scheme we were able to show that a localization of the excitation on one monomer unit might occur and the localization correlation with the inhomogeneity of the charge distribution. This leads to a stronger mixing of the states. Besides the dimer study we began to treat also larger aggregates on different levels of theory. Therefore, we also made a comparison to simple exciton model and investigated the effect of relaxation on the description of the spectrum of PTCDA.

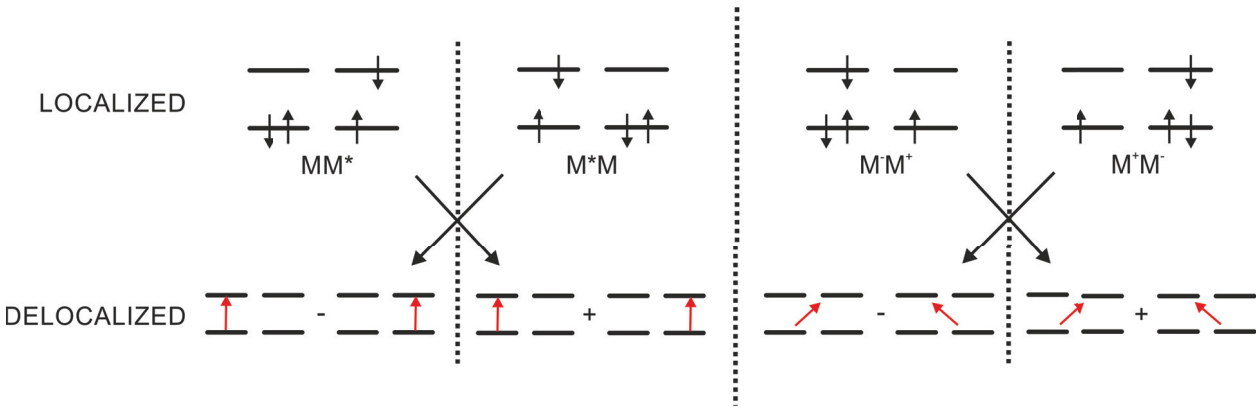

Figure 8.2.1: The major configurations of the excited states of a dimer are depicted. The localized states are depicted on the top and the delocalized states built by linear combination on the bottom. On the left hand side, the Frenkel configurations are shown and on the right hand side the Charge Transfer states

Understanding the properties of thin films of functionalized polycyclic aromatic molecules plays an important role. Therefore, the underlying physical processes in optoelectronic devices are of interest. Besides the application side such as optoelectronics[115, 116, 117], also the understanding of fundamental processes in biological systems is of great interest[118]. Therefore, the theory which tries to explain these processes should be able to handle different kind of systems like amorphous or crystalline ones. Within the study of perylene based systems we want to focus on models for crystalline and aggregate like systems. These systems which exist in a great variety have been investigated to a large extend. We want to focus on the subtle interplay between intramolecular degrees of freedom and the influence

of the surrounding in crystals and the influence on the spectral properties in a molecular picture[119, 120, 121, 122, 123, 124]. Within this study, we want to investigate this interplay by modeling the influence of structural relaxation in the presence of isotropic as well as anisotropic environments. Therefore, we investigate spectral shifts as well as the nature of excited states. Especially, we are interested in the properties of crystalline α-PTCDA and of the aggregate like PBI. For our study we use the dimer model system treated fully quantum mechanically. Within the dimer model the excitations can be described by four different types of excitations. Two local excitations with either Frenkel or Charge Transfer (CT) character and two delocalized ones built by linear combination of either Frenkel or CT states (see Figure 8.2.1). The interaction of Frenkel and CT states with a polarizable environment is mediated differently. Frenkel states interact by their transition density, while for CT states a charge stabilization can occur. Besides the dimer model we extent our study also on multimer systems and use a QM/MM[125, 126] scheme, especially for the PTCDA crystal.

The character of the lowest lying states in PTCDA or PBI aggregates is under debate.[127, 128] Forrest and coworkers designated the transition in crystalline phase of PTCDA to be a CT state within the picture of non-interacting excitons.[129] Scholz and coworkers[130] were able to explain the Photoluminescence (PL) spectrum of α-PTCDA, based on model calculations with B3LYP[55, 56, 57, 58, 59]/3-21G. They investigated the relaxed excimer and the zwitterionic state. Within their studies they concluded that the lowest PL band around 1.67 eV should be assigned to the anion-cation arrangement while the higher lying PL band is correlated with the excimer (1.72eV) state. In a different approach by Petelenz et al.[131] the relative position of the lowest CT state was calculated using calculated ionization potentials and electron affinities in combination with micro electrostatic calculations to determine the electrostatic stabilization energies. On the one side the method of Forrest and Shen[132] and on the other side the one of Soos et al.[133] were used. Nevertheless, both methods lead to mostly similar results. They predict a stabilization energy of about 2 eV. Including the effect of charge delocalization and polarization they assumed that the stabilization is reduced by about 1 eV. Using polarization energies from fullerene calculations they predicted the CT state to be located at 2.4-2.5 eV.[134] Also an interpretation as mixed Frenkel and CT states exists in literature.[133, 135] The mixed description stems from a model dimer calculation, whereas one might criticize that in a dimer only model the effects of disorder and of the infinite nature of the crystal is not take into account. Therefore, in other studies calculations were carried out to model the crystal environment for example by applying one or three dimensional approaches, whereas by Mazur and Petelenz a model Hamiltonian is constructed

and the excited states are represented by linear combinations of localized Frenkel and CT excitons.[131]

The effects on the excited state properties of PBI by a polarizable surrounding was investigated by Veldman et al.[136] For their studies they used time-resolved photoluminescence and photo-induced absorption experiments. Their experiments were carried out on J-aggregate like structures whereas the PBI molecule is bound to a perylene monoimid. They showed that the CT and Frenkel states are more or less iso-energetic. Within toluene the CT state is about 0.06 eV lower in energy, but in cyclohexane the reversed order should take place. Up to now only pure characters of the states were discussed, but interactions between CT and Frenkel states are taking place[137, 138]. Hence a description as mixed states where one state can have a dominant character is more appropriate. Heinz et al. confirmed this with the help of an empirical approach for estimating experimentally obtained solvatochromic shifts of solid and in liquid n-alkane matrices embedded perylene.[139] The shifts are in a range from 0.14 up to 0.21 eV. Studies on the PBI monomer showed that a polarizable continuum model (PCM) description with toluene parameters can lead to an increase of the transition dipole moment by about 0.9 Debye and a lowering in the coupling parameter, defined as half of the Davydov splitting[140]. Within this study Munoz-Losa and coworkers used the CIS approach in combination with the 6-31G(d)[92, 93, 141, 142] basis. Also by an QM/MMpol approach a lowering of the excitation energies and a decrease of the coupling is obtained. Curutchet et al.[143] and Neugebauer et al.[105] used this approach to study a PBI dimer solvated by water molecules. The inter-monomer distance is of about 3.5 Å in the dimer which is face to face oriented. By using the CIS/6-31G(d) method they found a lowering of 0.13 eV which is in a good agreement with the PCM approach where a lowering of 0.12 eV was found by Munoz-Losa et al. In both descriptions the coupling parameter decreases by 0.04 eV. For the QM/MMpol approach the increase of the dipole moments is 0.7 Debye which is in a good agreement with the findings by using the PCM description.

In addition, the question arises which theoretical method is sufficiently accurate. In time-dependent density functional theory (TD-DFT) based calculations the CT state are often predicted to be below the Frenkel ones. This might be true but could also be related to the fact that DFT functionals often predict to low excitation energies, especially for CT excitations. Within this context a recent study shows that indeed long-range corrected functionals, especially ωB97xd[144] are quite accurate in their description of vertical excitation energies of p-type semi-conductors.[145] Nevertheless, the results should be checked against more sophisticated methods like the SCS-CC2[146] or the SCS-ADC(2)[147] approaches. For smaller systems and if the nature of the excited state remains unclear even more sophisticated

methods should be addressed like CASPT2.[148]

8.2.2 PBI

In this part the results for the PBI dimer system should be presented by applying different QM approaches as well as explicit and implicit solvation models. Besides the role of the solvent a structural relaxation to an zwitterionic motif of the dimer is investigated. The related work can be separated into two parts, the first parts used an interpolation model which can be used to predict solvatochromic shifts based on TD-HF calculations to predict them on top of higher level *ab initio* methods. This part is continues work which was done within my bachelor thesis and within the PhD thesis of Volker Settels. The second part is related to work done in this thesis and deals with explicit and implicit solvation with respect to relaxation processes within the dimer model. Therefore, also higher level methods have been used to answer the remaining questions and proof the reliability of the linear model.[149]

Technical and computational details

The dimer structures used in this study are built up by optimized monomers, because an optimization of the dimer itself at various levels of theory led to bend structures. These bend structures were not found in the aggregates where only flat monomers are forming the stacks. Therefore, we used neutral monomers to built up the *MM* configuration which were optimized by using DFT in combination with dispersion correction. For the first studies related to the study of the longitudinal shift and rotation along the stacking axis and excited state calculation on TD-HF level the optimization of the monomers was carried out using the BLYP/TZV(P)[55, 56, 59, 57, 58, 150, 151] with dispersion correction[152, 75] using the Turbomole 6.0 program[61]. The notation TZV(P) means that the hydrogen atoms were treated using the TZV basis while for all non-hydrogen atoms the TZVP basis was used. For the relaxed structures and the calculations done within this work, the cation (M^+) and the anion (M^-) structures in gas phase were obtained by using the B3LYP/TZV(P)[55, 56, 59, 57, 58, 150, 151] level of theory. The structural feature will be denoted in *italic*. The structure of the explicitly solvated PBI dimer with 8 water molecules (PBI$(H_2O)_8$) was obtained by the following methodology. The preoptimization of the water shell was carried out by using the AMOEBA[5] FF implemented in the CAST[71] program. This water shell was then finally optimized using the BP86/TZV(P)[57, 82] method within the Turbomole 6.6 program package[61]. We used this methodolgy because in our studies we also applied the COSMO-RS[113, 153, 114, 154, 155] approach to compare the results with gas phase and

standard COSMO implementation in Turbomole. For COSMO-RS within the standard Turbomole package the σ-potentials are optimized for the BP86 functional. The microsolvated structures will be abbreviated by $(MM((H_2O)_8))$ for the neutral and $(M^+M^-((H_2O)_8))$ for the zwitterionic motif. The electronic configuration will be given by normal capital letters. For example, it is the case that by symmetry for the neutral (MM) structure an equal contribution of both local Frenkel type excitation is obtained and can be written as (M*M or MM*) and for the zwitterionic electronic configuration the notation is the following: M^+M^- or M^-M^+.
For the study of solvent effects on the excited state and properties we applied the IEFPCM[156, 157, 158, 108] formalism in combination with TD-HF[159, 160, 161, 162, 163, 164, 165] for the investigation of the rotation and the shift of two PBI units with respect to each other. The focus in the former study laid on the rotation from 0 to 90°, whereas the TD-HF excitation energies were added to BLYP-D ground state potential energy curve (PEC). These calculations were carried out with the Gaussian03 program[166] and will be only briefly mentioned and related to the calculations done in this study.[149] In this study the treatment of the surrounding was realized by using the explicit solvent molecules and by employing the COSMO implementation within the Turbomole 6.6 version. Within this version of Turbomole it is also possible to use ADC(2) in combination with COSMO which is the perfect tool to proof the former results. This study applies parameters for cyclohexane ($\epsilon = 2.028, n = 1.424$) and non-standard parameters to include also media with higher refractive indices ($\epsilon = 10.0, n = 1.5/3.0$).
The excited state calculations in this study were carried out with the SCS-CC2/SV(P)[146, 167], the SCS-ADC(2)/SV(P)[147, 167] and the ADC(2)/SV(P)[147, 167] approaches, but the focus will lay on the SCS (spin component scaling) variants.

Results and discussion

For the simulation of the solvent included by a PCM description the findings indicated that a generalization scheme could be found for transferring shifts from one method to another. These findings based on the simulation of the PECs of the 3.3 Å stacked PBI dimer which is rotated along the stacking axis. Due to the simulations it was predicted that the ground state is stabilized by 2.18 ± 0.06 eV in average if water is simulated within the IEFPCM formalism. For cyclohexane the stabilization is less and of about 0.71 ± 0.06 eV. The shape of the ground state PEC did not change much by including the IEFPCM description. An overall stabilization could be observed. This behavior was observed for the excitations as well. Here it could be shown that the maximum shift is of about 0.2 eV. Besides the fact that all

states are stabilized an interestingly behavior was found that is connected with transition dipole moments and the refractive index of the solvent. The higher the refractive index is the higher are the shifts of the states and additionally the shifts are direct proportional to the transition dipole moments. These findings are explainable with Bayliss law[168]

$$\Delta E^{exc} \propto \frac{\mu^2}{R^3} \cdot \frac{n^2-1}{2n^2+1}, \tag{8.2.1}$$

with R the cavity radius, n the refractive index and μ the transition dipole moment. The second observation which was unexpected is that the CT states are only stabilized to a small extend. This is counter intuitive to the expectations one might had. Within the standard picture the CT states should be more stabilized through a polar solvent like water. But is explainable by the high symmetric configuration of the two diabatic electronic configurations (M^+M^- or M^-M^+) which are coupled so that no real localization of the charges occurs. Due to the findings the shifts in excitation energies (ΔE^{exc}) were plotted against the square of the transition dipole moments (μ^2) for the rotation and other PECs as well. From the data it was possible to extract a linear relationship and obtain fitted parameters. Accordingly to the fitted parameters it was possible to extrapolate data obtained for gas phase on SCS-CC2 level for different solvent parameters. The oscillator strengths could be adopted due to Chako's law[169] as well. The oscillator strength for a chosen solvent is given as:

$$f^{solv} = f^{vac}\frac{(n^2+2)^2}{9n}. \tag{8.2.2}$$

For the obtained data set it was possible to get a linear relationship, too. Even though Chako's law is only defined for spherical cavities. Therefore, the previous work could be summarize in the manner that it was possible to extrapolate the SCS-CC gas phase curve and the related properties without doing an explicit calculation with a COSMO approach.[149] Because of the simplicity and the counter intuitive results for the stabilization of the CT states, additional calculations were performed which should be presented in detail as the next step.

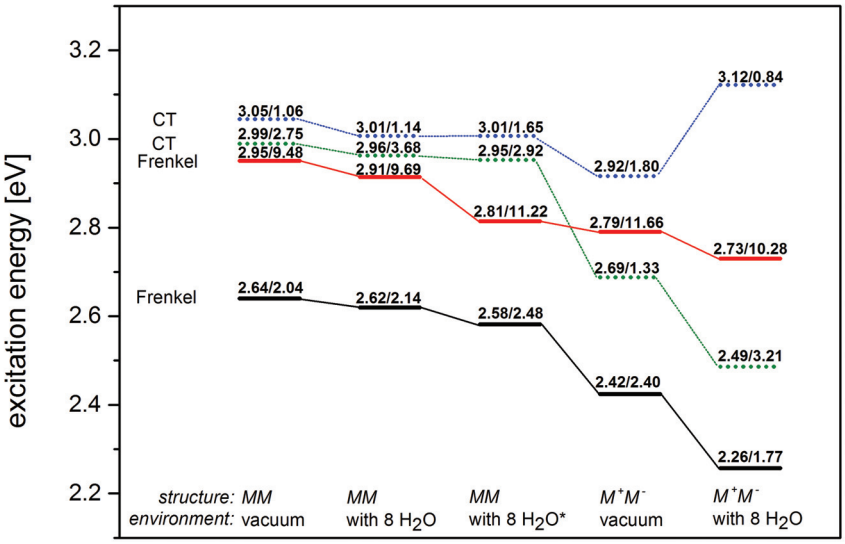

Figure 8.2.2: The excitation energies for different structural distortions and different applied environment (*vacuum* and $8H_2O$) are given on the SCS-CC2/SV(P) level (in eV). The system of interest is the face-to-face stacked dimer of PBI which is rotated by 30°. The neutral structure configuration is given as (MM) and the zwitterionic structure as (M^+M^-). The concerning Frenkel states are represented by solid lines and the CT states by dashed lines. The numbers (N/N) are related to excitation energies in eV and transition dipole moments in Debye. *explicit water by combining the shifts from the direct model.

As mentioned beforehand the symmetry of the dimer hinders the charge localization, because both electronic configurations (M^+M^- or M^-M^+) are coupled. Therefore, the influence of a solvent shell which lifts or lowers this symmetry should be addressed. In a second step, the influence of a relaxation process should be investigated which breaks the symmetry. The inclusion of 12 methane molecules for the 30° rotated PBI dimer shows indeed no strong influence of the solvent shell. No drastic change in the ordering of the states was obtained, i.e. the gas phase results were underpinned. The solvent shell by the methane lowers the symmetry to C_2 symmetry. Starting at this point the calculations of the neutral species with an asymmetric water shell should be presented ($MM((H_2O)_8)$). The findings for the small water shell and the neutral dimer configurations are in line with the methane findings[149] (see Figure 8.2.2). The fact that the same trend for the excitation energy shifts and the

ground state were found for different non-polar and polar solvents as well as explicit and implicit solvation indicates that the results are quite general. The influence of a polarizable environment or even the aggregate environment might have no strong influence in the case of PBI aggregates. Besides the symmetry breaking effects through the surrounding or the effect of polarization the structural relaxation should be discussed as a next step. In a study made by Schubert et al.[170] it was shown that for vacuum a geometry variation from the neutral to the zwitterionic configuration can lead to a stabilization of the CT state with respect to the upper Frenkel state so that both states cross. To proof our first results and go into further detail, calculations were carried out using the SCS-CC2/SV(P) method. The ground and the first four excited states of various 30° rotated PBI dimers were treated. In Figure 8.2.2 the results for vacuum, neutral (MM) and zwitterionic (M^+M^-) configuration and for the microsolvated counterparts are depicted ($MM((H_2O)_8)/M^+M^-((H_2O)_8)$). For vacuum the calculations predict the same effects on the ordering of the states like predicted by Schubert and coworkers. Concerning Figure 8.2.2 only the excitation energies are depicted. One should take into account that the red shift also occurs due to the destabilization of the ground state which is up to 1.16 eV. Taking the microsolvation into account a different behavior is found for the zwitterionic system surrounded by eight water molecules. The lower CT state is stabilized the most by about 0.2 eV, whereas the lower Frenkel state is only stabilized by 0.16 eV. The Frenkel state with high oscillator strength (bright) is only weakly influenced (0.06 eV). Interestingly, the upper CT state is even destabilized by about 0.22 eV. The results of these calculations indicate that the influence of the structure is predominant and determines the influence mediated via the solvent. In addition, it is also crucial to mention that the shift due to the structural distortion is stronger compared with the solvent shifts.

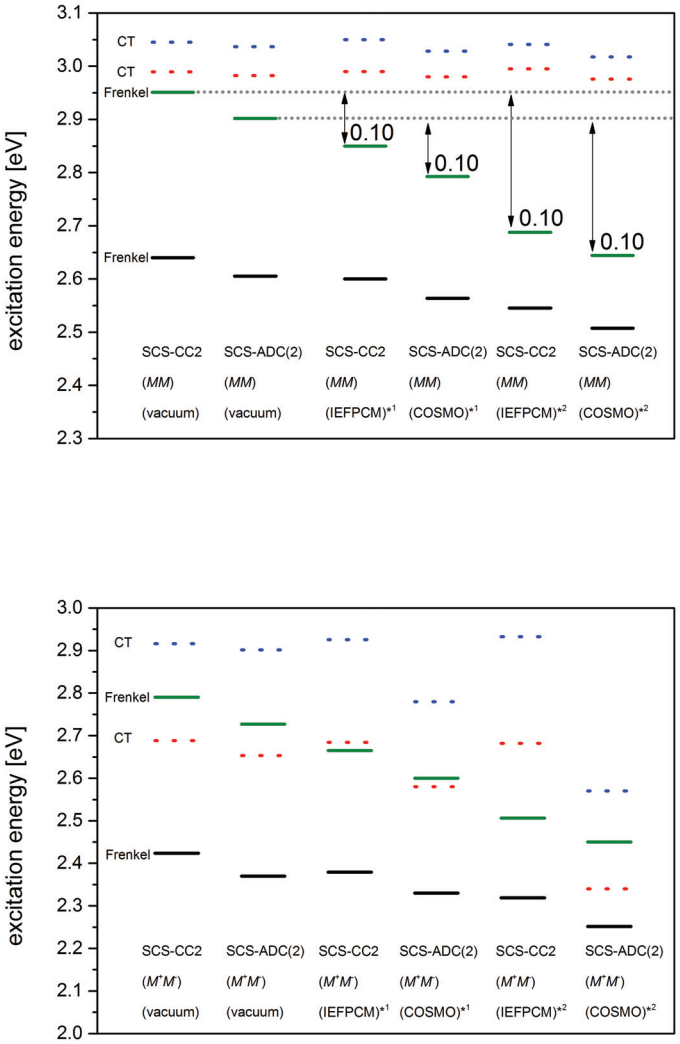

Figure 8.2.3: On top the excitation energies are shown for the neutral (MM) and in the bottom for the zwitterionic (M^+M^-) parallel stacked and 30° rotated PBI dimer. The excitation energies are related to SCS-CC2/SV(P) and SCS-ADC(2) calculations. Dashed lines stand for states with more CT character and solid lines for the more Frenkel like states. $IEFPCM^{*1}$solvatochromic shifts for cyclohexane predicted by using the direct model. $COSMO^{*1}$ is used with cyclohexane parameters. $IEFPCM^{*2}$ solvatochromic shifts for $\epsilon = 10.0$ and n = 3.0 predicted by using the direct model. $COSMO^{*2}$ is used with $\epsilon = 10.0$ and n = 3.0.

Up to this point solvent effects were treated with small solvation shells or using a PCM

description in combination with TD-HF. To test the previous calculations we began to use the ADC(2) and the SCS-ADC(2) approach in combination with the COSMO description implemented in the Turbomole 6.6 version. The calculations were performed for the neutral (MM) and the zwitterionic (M^+M^-) configuration. For these calculation a wider range of the parameters within the COSMO approach were used like mentioned beforehand. In this manner the cyclohexane ($\epsilon = 2.2028, n = 1.424$) as well as the following values for the refractive indices in combination with the dielectric constant were chosen: $\epsilon = 10.0$ and $n = 1.0/3.0$. The results from these calculations are summarized in Figure 8.2.3. For the discussion of the obtained shifts we focused on the upper Frenkel and the lower CT state. The results of the SCS-ADC(2)/COSMO calculations should be compared with results previously made by the direct approach which means that the shifts on TD-HF//IEFPCM level are adopted to SCS-CC2/SV(P) gas phase results.[149]. This approach predicted a shift for the 30° configuration of about 0.10 eV for the upper Frenkel state. The shifts for the lower CT state are very small (0.01 eV). These shifts for the neutral (MM) configuration are comparable with the ones obtained on the SCS-ADC(2)/COSMO level. It predicts shifts of about 0.11 for the upper Frenkel and 0.003 eV for the lower CT state. In the case of the higher refractive index and the higher dielectric constant ($\epsilon = 10.0$ and $n = 1.0/3.0$) the direct approach predicts a shift of 0.26 eV for the upper Frenkel and an upshift of about 0.01 for the lower CT state. The direct comparison with the SCS-ADC(2)/COSMO computations for the same parameters are in a good agreement(Frenkel: 0.26 eV and CT: 0.01 eV).
In consequence, one can summarize that for the neutral configuration the prediction of shifts due to the solvent can be predicted by using the direct approach and can be seen as good estimated to more expensive computations like ADC(2)/COSMO (see Figure 8.2.3 (top)). For the zwitterionic configurations the situation is getting more complex. The shifts from the direct method are for the cyclohexane results in a satisfying agreement, but for the other cases differences occur. For cyclohexane SCS-ADC(2)/COSMO predicts a shift of 0.05 eV for the concerning CT state and 0.07 eV for the upper Frenkel. This is in line with the previous results. Within both approaches the CT and Frenkel state are virtually degenerate. But for a surrounding with higher ϵ and n the situation changes. For $\epsilon = 10.0$ and $n = 3.0$ the shift of the upper Frenkel state is predicted to be of about 0.28 eV, but the shifts for the lower CT diverge. The TD-HF/IEFPCM approach predict nearly no shift, while SCS-ADC(2)/COSMO predicts a shift of 0.31 eV. So the ordering predicted by both methods is reversed. The reason for the differences in the shifts might be related to differences in the mixing of CT and Frenkel states. In Table 8.1 the computed CT character with respect to the transition density matrix analysis for different surroundings are given. The analysis was

carried out by using the TheoDORE program [171, 172, 173].

	TD-HF			*SCS-ADC(2)*		
state	vacuum	cyclohexane	10.0/3.0	vacuum	cyclohexane	10.0/3.0
lower Frenkel	0.05	0.05	0.04	0.20	0.16	0.11
upper Frenkel	0.03	0.03	0.03	0.06	0.10	0.04
lower CT	0.97	0.97	0.97	0.85	0.84	0.93
upper CT	0.93	0.93	0.93	0.87	0.90	0.91

Table 8.1: The CT numbers obtained from a transition density analysis are shown for the zwitterionic configuration at different environments. The numbers are related to TD-HF/IEFPCM and SCS-ADC(2)/COSMO computations.

Table 8.1 shows that the variations in the CT character stem indeed from a stronger mixing of the lower CT and the upper Frenkel state. The mixing is possible, because both belong to the same irreducible representation in D_{2h} symmetry. For TD-HF no variations in the CT character are predicted, so all states are nearly pure CT or Frenkel states for all surroundings. A different situation is described by the SCS-ADC(2) method. Therefore, a demixing is predicted by increasing ϵ and n. At vacuum conditions the lower Frenkel state ha of about 20 % CT character which decreases to 16 % for cyclohexane and 11 % for ($\epsilon = 10.0$ and $n = 3.0$). The opposite behavior is obtained for the predominantly CT states. An increase of about 8 % is obtained for the lower CT state. The variations of the CT states might result, because SCS-ADC(2) predict states to be close in energy, while TD-HF computes the CT to lie higher above the Frenkel states(0.9 eV).

8.2.3 PTCDA

In this section the insights obtained from the PBI calculations and the description of intra-molecular relaxation processes in the presence of an isotropic medium should are used and extended to the dimer as well as larger aggregates of PTCDA. Therefore, different strategies like COSMO calculations, QM/MM strategies and multimer calculations are employed to model the situation in the crystal. On the one side the focus lays on the accurate description of the excited states and their characteristics (Frenkel/CT) and on the other side we want to continue addressing the role of the inter- and intra-molecular degrees of freedom by applying different strategies. This can be done by using high-level QM approaches for the dimer model and applying TD-DFT and a semi-empirical approach for the multimers. As mentioned in the introduction, former investigations were able to explain the measured absorption spectra of PTCDA and assigned the transition in the crystalline to be a CT state. The investigations

made by Settels et al.[137, 174] shed a different light on this and motivated this investigation. Assuming that the discussion remains open if PTCDA might act differently compared with other perylene based molecules which is in contradiction to the investigations made by Settels et al., but might be related due to the level of description of the surrounding, up to this point. In the former study the description was limited to a dimer ansatz by using the Apèry's[175] factor to describe the increasing splitting in the aggregate and by using a static embedding scheme (QM/MM). Within this approach the Apèry's constant was used times two for the correction of the Davydov splitting.

Technical and computational details

The dimer structures used within this study were built up using optimized monomers of the neutral, anionic and cationic species. The monomers were optimized by using the ωB97xd/TZVP approach which is implemented in the Gaussian09 program package. The crystal structures and the multimers were built up using these monomer structures as well. The treatment of the environment was realized by applying the COSMO model for the SCS-ADC(2) calculations and the IEFPCM approach for the TD-DFT calculations. For the QM/MM calculations the systems we introduce were built to mimic the environment in α-PTCDA crystal films. We employed the cell parameters described by Tojo and Mizuguchi.[176] Two different cells are given in Figure 8.2.8. The small excerpt from the larger supercell is shown in red. The blue colored dimer structure indicates the part which was treated quantum mechanically (also valid selection for monomer calculations). The supercell which is depicted is built up by 54 monomers and the cell volume is 36702.1 $Å^3$. To describe the excited state properties of the system we applied different QM/MM approaches. On the one side we used the Chemshell 3.4[177, 178, 179] program and on the other side we used the Gaussian09 program to read in point charges. The charges which simulated the crystal environment were calculated in two different ways. On the one side we used AM1 derived charges and on the other side ESP fitted charges based on ωB97xd/TZVP calculations of the PTCDA monomer. Within the Chemshell approach we used the DL-POLY[180] interface to the AMBER force field by using GAFF (generalized amber force field)[181, 182] parameters. For the excited state calculations on ωB97xd/TZVP level we used only charges and neglected steric effects.

The computations of the CT numbers were carried out with the TheoDORE program package[171, 172, 173] These numbers directly represent the amount of CT character. Within the picture of a single determinant ground state the transition density matrix corresponds

to one-electron excitation transfer operators. Using the dimer excited states the four localized states (Frenkel) are represented by the diagonal elements and the linear combinations which describe the delocalized states (CT) refer to the off-diagonal elements. The charge transfer number can be expressed as the sum over all contributions on the respective fragments:$\Omega_{AB}^{\alpha} = \frac{1}{2}\sum_{\alpha\in A\cap b\in B}\{\left(D_{AB}^{0\alpha,[LO]}\right)^2\}$. The methods for the excited state calculations are TD-ωB97xd/6-31+G(d)[144, 92, 183, 184], TD-ωB97xd/TZVP, SCS-ADC(2)/SVP and ZIndo(S)[185, 186, 187, 188, 189, 190, 191, 192, 193] and will be addressed at the specific points in the following.

Results and discussion

A large number studies in this field use monomer based descriptions, whereas in this study aggregate structures are used within a supermolecule ansatz. The starting point of our investigations is the dimer. In contrast to our model the monomer approaches often use a mixed Holstein-Peierls[194, 195] Hamiltonian to describe the coupling. In this picture the coupling is described by a Förster term (sometimes also more comprehensive expressions are used) for the coupling of the ground and the excited states of the monomer. Due to additional coupling terms the interactions with CT states can be described and improved.[196, 197, 198, 199, 200] Most of the time the parameters which are used in these models are obtained via experiment and fitted with respect to the system modeled. The supermolecular approach might have some advantages over these methods, because the interaction between monomers is treated on a full quantum mechanical level. In this manner the description of both Frenkel and CT state is founded on the same basis. As mentioned in the introduction the interaction of CT and Frenkel states is mediated differently. In the adiabatic picture in general all states can mix. This mixing can be seen in Table 8.2, where results of dimer calculations are summarized.

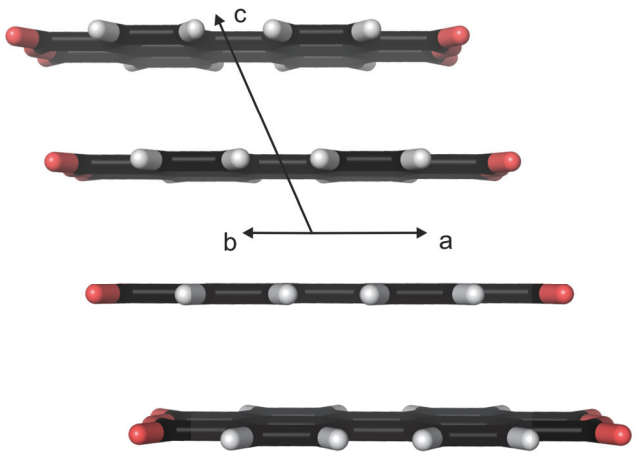

Figure 8.2.4: The orientation of the monomers within an out-of-plane stack along the crystalline c-axis is shown.

We first focused on situation where the exciton is delocalized along out-of-plane stack which is defined by the cell axis c and is illustrated in Figure 8.2.4. Within the first part the focus is laid on the influence of the environment and structural relaxation using Continuum Solvation approaches. In addition, we want to show different methods and test how they address these effects. Besides computationally very demanding methods like the SCS-ADC(2) approach we applied also more cheaper ones like a long-range corrected DFT functional with empirical dispersion correction, namely the ωB97xd functional to test the capabilities in making trustworthy predictions compared with SCS-ADC(2). In a former study different dimer arrangements of a parallel stacked PTCDA were investigated on the SCS-CC2 level of theory. A conical intersection was located between the first and the second excited state which both possess mostly Frenkel character. The simulated degrees of freedom applied were the longitudinal and the transversal shift of the two monomers with respect to each other (parallel stacked by 3.3 Å). On top of the computed Potential Energy Surface (PES) dynamics were calculated by using wave packet propagation methods. The Franck-Condon (FC) region was located at 1.19 Å longitudinal and 1.05 Å transversal shift. Starting at the FC region the wave packet propagates to the CI and a population transfer to the first excited state occurs. For simulating the effect of structural relaxation we applied a stepwise distortion from a neutral (MM) to a zwitterionic (M^+M^-) configuration. For testing the capabilities of ωB97xd/6-31+G(d) approach we compared vacuum results with computations

on SCS-ADC(2)/SVP level. In Figure 8.2.6 the results of the simulated shift around the FC region for the S2 state (1.19 Å (long)/1.05 Å (trans)) on TD-ωB97xd/6-31+G(d) level are depicted. The dimer structure was built up using the optimized monomer structures on ωB97xd/TZVP level, whereas the inter-monomer distance was set to 3.3 Å. By simulating the transition, it can be stated that the second and third excited state flip their positions. This can be observed by looking at the calculated CT numbers. At the calculated distortion of 40 % the S2 and S3 state are nearly degenerate. The energy difference is 0.013 eV for the vertical excitation energies. The CT characters of the S1 and the S4 excited state remain the same. For the fully distorted (100 %) structure the ground state (GS) is slightly destabilized by about 0.28 eV. The same trend is obtained as well for the SCS-ADC(2) calculations which are depicted in Figure 8.2.5. The S2 and S3 state change their positions as well. But the location of the intersection seems to occur at larger distortion values and can be located around 57.5 % of distortion. If one compares the excitation energy values of both methods than ωB97xd predicts slightly lower lying excitation energies, but the difference never exceeds 0.24 eV.

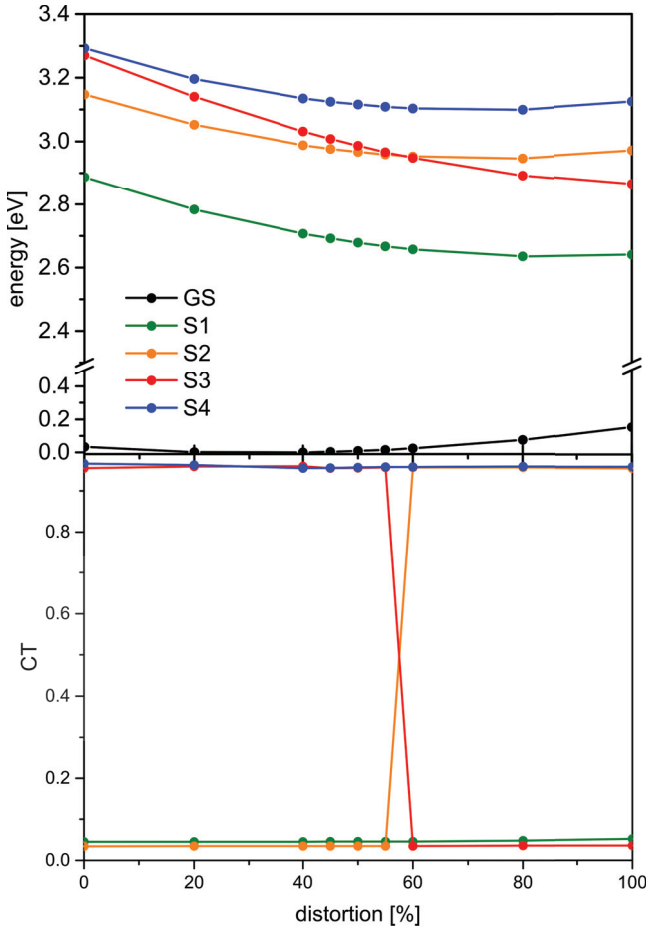

Figure 8.2.5: In the upper panel SCS-ADC(2)/SVP dimer potential energy curves as a function of the distortion in [%] are given. The lower panel shows the quantum chemically determined CT numbers for the electronic states.

In a second step, we included the effect of a polarizable surrounding simulated within the ωB97xd/6-31+G(d)//IEFPCM (cyclohexane) model. By inclusion of the environment on this level of theory the intersection of the 2^{nd} and 3^{rd} state occurs for a larger value of distortion. The results are depicted in Figure 8.2.7. Analyzing the excited state shifts one can see that the S2 state which has the largest oscillator strength is stabilized the most. In addition, it can be seen that the effect of stabilization increases the more the structures are getting distorted.

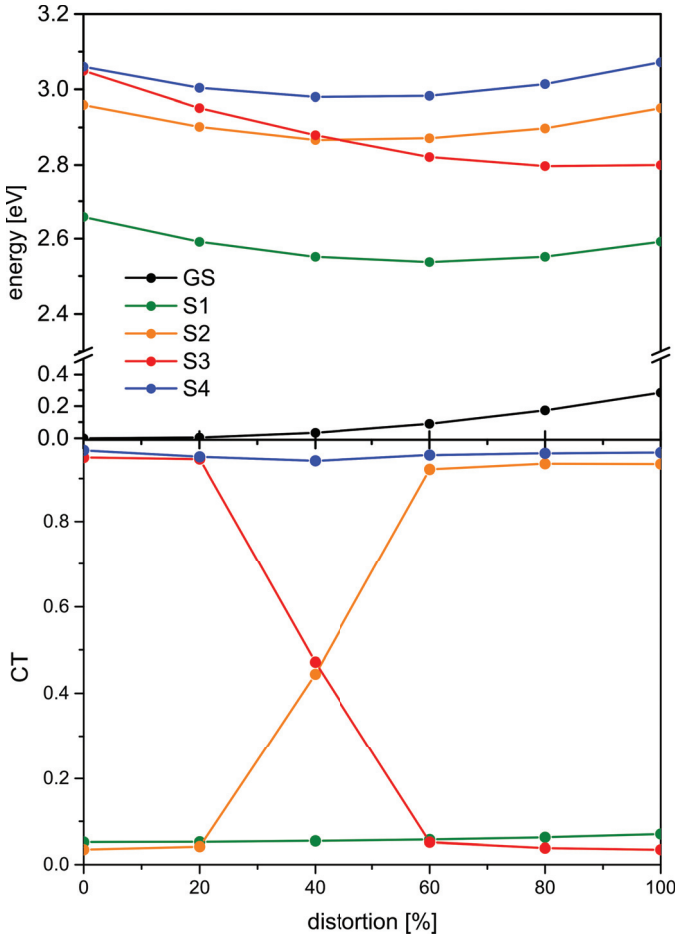

Figure 8.2.6: In the upper part ωB97xd/6-31+G(d) dimer potential energy curves as a function of the distortion in [%] are shown. The lower panel gives the quantum chemically determined CT numbers for the electronic states.

For the fully distorted (100 %) structure the ground state (GS) is destabilized by about 0.28 eV. The same trend is obtained for the SCS-ADC(2) calculations which are depicted in Figure 8.2.5. The S2 and S3 state change their positions as well. But the location of the intersection seems to occur at larger distortion values and can be located around 57.5 % of distortion. The excitation energy values predicted by ωB97xd are slightly lower than those computed with SCS/ADC(2)/SVP, but the difference never exceeds 0.24 eV. In a second step, we included the effect of a polarizable surrounding simulated within the ωB97xd/6-31+G(d)//IEFPCM (cyclohexane) model. By inclusion of the environment on this level of theory the intersection of the 2^{nd} and 3^{rd} state occurs for a larger value of distortion. The results are depicted in Figure 8.2.7. Obviously the S2 state which has the largest oscillator strength is stabilized the most. In addition, it can be seen that the effect of the shift increases

the more the structures are getting distorted.

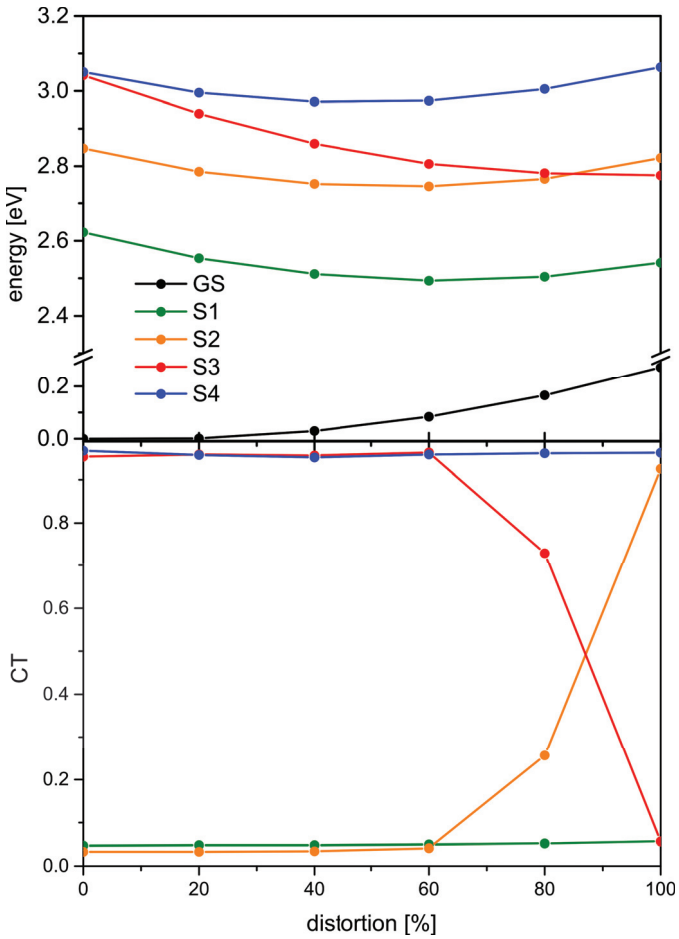

Figure 8.2.7: The upper panel shows ωB97xd/6-31+G(d)//IEFPCM(cyclohexane) dimer potential energy curves as a function of the distortion in [%]. The lower panel shows the quantum chemically determined CT numbers for the different electronic states.

To proof the obtained results with the IEFPCM model, we investigated the neutral (*MM*) configuration as well with SCS-ADC(2)/SVP//COSMO (see Table 8.2). For both methods we found an increase in oscillator strengths of the S2 state up to a value of 1.51 which is an increase by 36 % for ωB97xd and by 17 % for SCS-ADC(2). The oscillator strengths for the other states stay the same. The shift of excitation energies is of about 0.11 eV for S2 SCS-ADC(2) and the same at ωB97xd level. The S3 state is only shifted by 0.01 eV. The shifts for the other states are also very small. Besides the distortion of the dimer arrangement around the FC region we also computed the distortion of the parallel dimer arrangement and the arrangement of a 1.5 Å longitudinal shifted dimer. The vacuum values on ωB97xd

level indicate that also for the parallel arrangement an interchange of the energetic order of the S2 and S3 excited state occurs. For distortions of 40 % and 60 % the S2 and S3 state both possess a 50/50 mixture. Interestingly for the parallel arrangement is the fact that by inclusion of a polarization through the environment modeled with IEFPCM or COSMO the stabilization of the bright Frenkel like state is large enough that the interchange with the S3 state does not occur.

Related to the investigations based on the distortion of the dimer structures of the FC motif Table 8.2 summarizes a comparison between SCS-ADC(2) and ωB97xd. In Table 8.3 additionally the results of our QM/MM investigations are shown. The vertical excitation energies, oscillator strengths and the CT numbers are given. The geometries used for the QM/MM investigations are slightly different to the FC geometry, but both resemble the crystal structure. For the FC geometry both methods predict that the two Frenkel states lay below the CT states. As it was already discussed and seen for the simulated distortions the ωB97xd/TZVP excitation energies are approximately 0.2 eV lower than the values obtained with SCS-ADC(2)/SVP. Nevertheless the relative energy spacing are well described and are in the range of 0.05 eV. In conclusion to the shift calculations as well as the neutral (*MM*) FC are in good accordance with Bayliss' law as discussed for the PBI case. The explanation of this behavior is may be related to the fact that due to the high symmetry of the dimer which is not lowered due to a PCM description, a strong mixing of Frenkel and CT states can occur. Therefore, no charge accumulation on a monomer can take place and the CT states posses no net dipole moment which would interact with the environment.

FC dimer (MM)	*ωB97xd/6-31G+(d)*			*SCS-ADC(2)*		
vacuum	exc. energy [eV]	osc.	qCT	exc. energy [eV]	osc.	qCT
1	2.66	0.00	0.05	2.85	0.00	0.05
2	2.96	1.11	0.04	3.11	1.29	0.03
3	3.05	0.00	0.95	3.24	0.00	0.96
4	3.06	0.03	0.97	3.26	0.03	0.97
cyclohexane	exc. energy [eV]	osc.	qCT	exc. energy [eV]	osc.	qCT
1	2.62	0.00	0.05	2.81	0.00	0.04
2	2.85	1.51	0.03	3.00	1.51	0.04
3	3.04	0.00	0.95	3.23	0.00	0.96
4	3.05	0.03	0.97	3.25	0.03	0.97

Table 8.2: The excitation energies, oscillator strengths and CT numbers are given for the neutral (MM) FC dimer arrangement.

SCS-CC2/SVP	*vacuum*			*AM1/small*			*AM1/big*			*ESP/small*		
state	exc. energy [eV]	osc.	qCT	exc. energy [eV]	osc.	qCT	exc. energy [eV]	osc.	qCT	exc. energy [eV]	osc.	qCT
1	2.88	0.00	0.07	2.86	0.08	0.00	2.85	0.07	0.00	2.77	0.00	0.09
2	3.14	1.00	0.16	3.10	0.32	0.81	3.09	0.30	0.87	3.01	0.64	0.45
3	3.32	0.00	0.93	3.21	0.66	0.31	3.21	0.71	0.30	3.12	0.48	0.56
4	3.35	0.16	0.84	3.44	0.92	0.04	3.43	0.93	0.05	3.33	0.05	0.93
SCS-ADC(2)/SVP	*vacuum*			*ESP/small*								
state	exc. energy [eV]	osc.	qCT	exc. energy [eV]	osc.	qCT						
1	2.85	0.00	0.07	2.73	0.00	0.08						
2	3.10	1.18	0.13	2.97	0.93	0.30						
3	3.31	0.00	0.93	3.09	0.36	0.69						
4	3.34	0.14	0.88	3.32	0.04	0.94						
ωB97xd/TZVP	*vacuum*			*ESP/small*			*ESP/big*					
state	exc. energy [eV]	osc.	qCT	exc. energy [eV]	osc.	qCT	exc. energy [eV]	osc.	qCT			
1	2.66	0.00	0.07	2.65	0.00	0.08	2.65	0.00	0.07			
2	2.94	0.98	0.15	2.92	0.80	0.32	2.92	0.78	0.35			
3	3.12	0.00	0.93	3.02	0.31	0.66	3.03	0.35	0.67			
4	3.13	0.14	0.86	3.22	0.03	0.94	3.21	0.05	0.93			

Table 8.3: The excitation energies, oscillator strengths and CT numbers for the first four excited states of the dimer built up by ωB97xd/TZVP optimized monomers are shown. The dimer configuration is related to the α-PTCDA crystal configuration. On the one side vacuum calculations and on the other side different charge models (QM/MM) were used. The results are related to two different cell configurations small (red) and big(black) (see Figure 8.2.8).

In a next step the influence of symmetry lowering on charge localization and a net dipole moment was investigated. Therefore, we applied a QM/MM scheme, whereas the inner dimer is treated fully quantum mechanically while the influence of the surrounding is modeled by an interacting charge field. For simulating a different environment we employed two crystal surroundings. In addition, we employed different strategies for estimating the atomic charges (see Figure 8.2.8). The QM part is highlighted in blue and the small cell is given in red and the whole system is called the big system (supercell). The clusters have been built accordingly to the following cell parameters: $P12_1/n1$ (no.14), a=3.704 Å, b=12.014 Å, c=17.161 Å and $\beta = 93.27°$.[176]

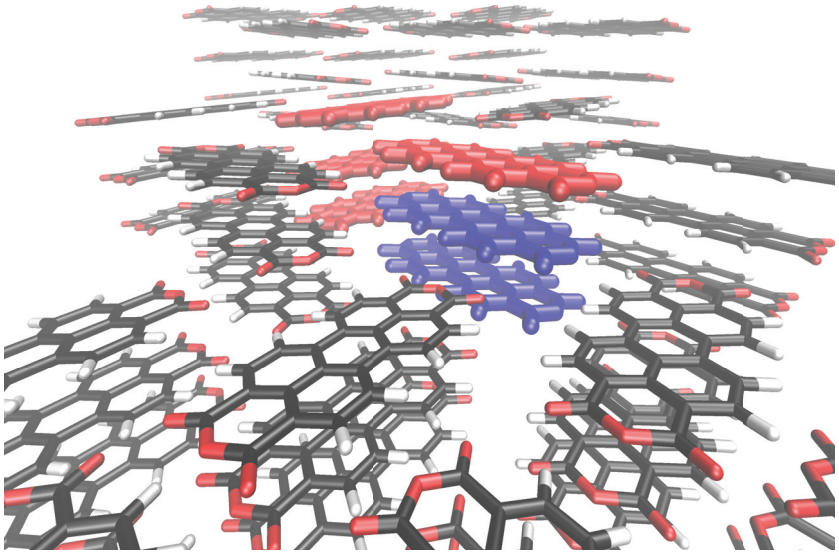

Figure 8.2.8: The different clusters within the QM/MM calculations are depicted. The QM part is highlighted in blue and molecules forming the small charge field are shown in red. The monomers were optimized by using the ωB97xd/TZVP approach.

As already mentioned we used AM1/Mulliken and ESP fitted charges due to the ωB97xd/TZVP density. The summarized results are given in Table 8.3. The differences in geometry between the crystal dimers and the built dimer (FC) remain small. If one compares the vacuum results given in Table 8.3 with the results in Table 8.2 it can be seen that the influence of the geometry variation on the excitation energies is small. In the upper part of Table 8.3

the SCS-CC2/SVP results for the AM1/Mulliken based charge field are shown. Within this calculation the CT state (S3 in vacuum) is more downshifted than the Frenkel state (S2 in vacuum). Additionally it is obtained that both states strongly mix which is figured out by calculating the CT numbers. The oscillator strength in combination with the CT number indicate that the S2 state (AM1) has even more CT character than the S3 (AM1). By using the ESP fitted charges both states mix as well, but the lower state still possesses the higher oscillator strength. Again, SCS-ADC(2) and ωB97xd deliver qualitatively the same picture and agree very well with the SCS-CC2 computations.

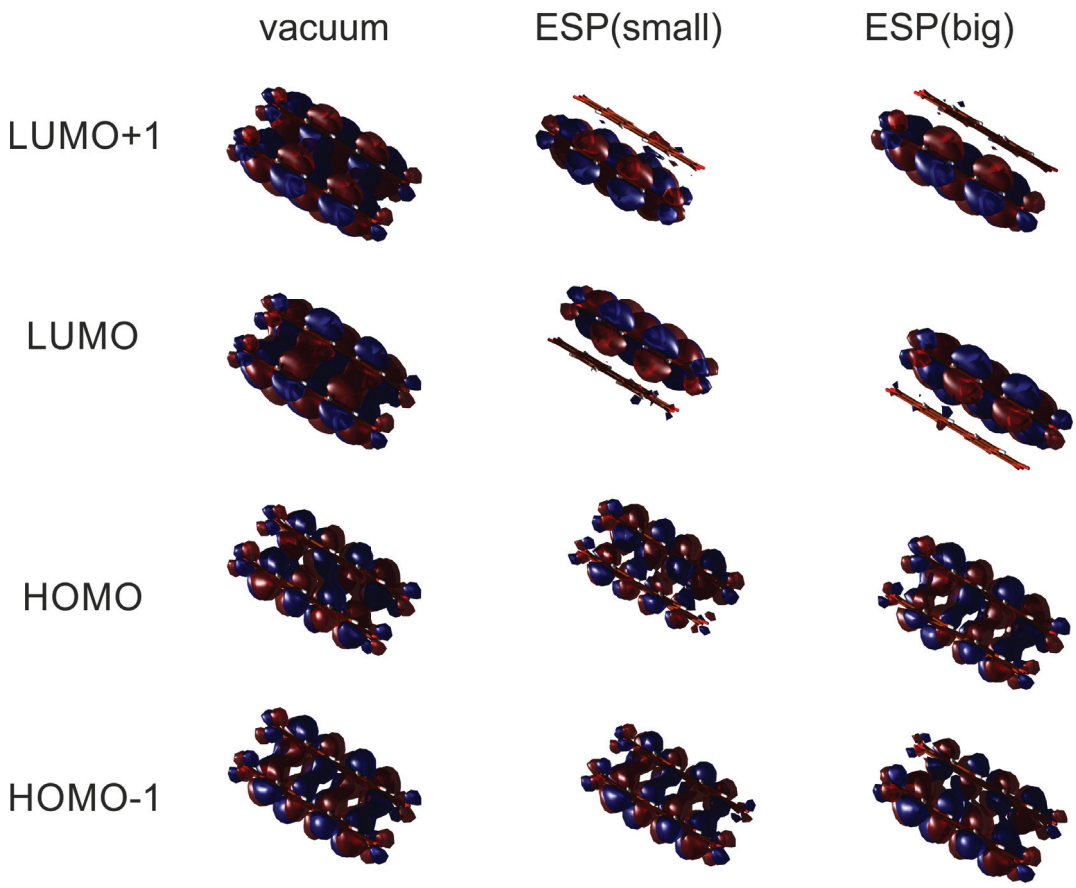

Figure 8.2.9: The influence of different surroundings on the MOs (ωB97xd/TZVP) which are involved in the lower excitations of the dimer is shown. The field ESP (small) is built up by the red PTCDA molecules in Figure 8.2.8. The ESP (big) field is built up by all depicted PTCDA molecules.

The differences to the PCM description can be related due the lower symmetry of the charge fields. This is also observable by the MOs which are involved in the excitation processes discussed. The MOs for vacuum conditions are fully delocalized over the dimer, the MOs of the charge field localize due to lower symmetry. Especially for the LUMO and LUMO+1 a lowering in symmetry is obtained. It can be stated that the crystal surrounding leads to a strong mixing of the states, but within the manifold of states the lowest one remains of nearly pure Frenkel type. Additionally the lowest Frenkel type state is in range of 0.2-0.3 eV lower in energy than the next mixed states.

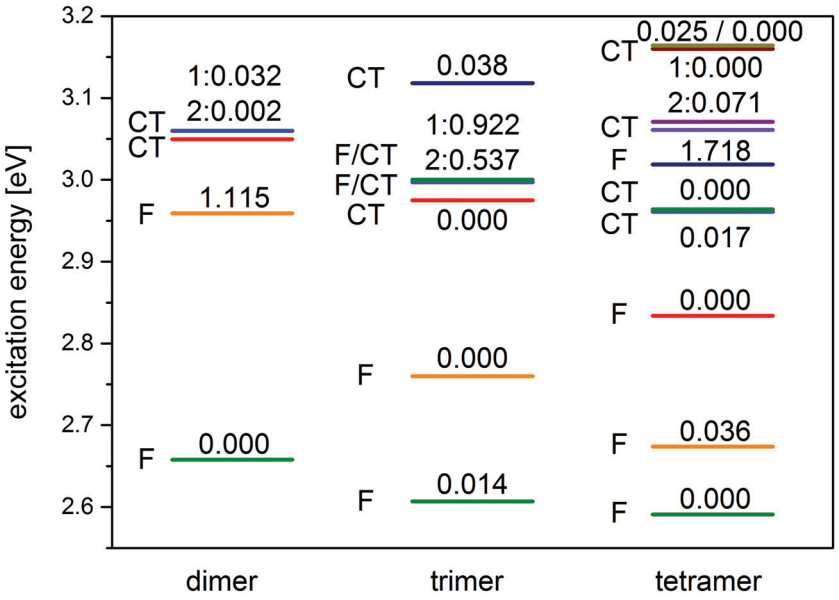

Figure 8.2.10: : The vertical excitation energies in eV are given for the dimer, trimer and tetramer of PTCDA in combination with the computed oscillator strengths. The systems are built by monomer units optimized on ωB97xd/TZVP level of theory and arranged in the FC geometry. The Excitations were treated by using the TD- ωB97xd/6-31+G(d) approach.

In various studies it was indicated that excitons are delocalized over several monomer units in strong interacting stacks.[129, 201] To shed some light onto this question we performed calculations of the trimer and tetramer in FC (*MM*) configuration. We used the ωB97xd/6-31+G(d) approach to address the question of how the order of the CT and Frenkel states is influenced by increasing the stack size along the c-axis. The results are depicted in Figure

8.2.10, whereas the excitation energies and the related oscillator strengths are given. The related CT numbers are given in Table 8.4. The first excited state of the monomer splits into four states for the dimer. For the trimer respectively the tetramer this would deliver 9 or 16 states. But to keep the computations manageable within a reasonable time only ten excited states were calculated for the tetramer. Within our calculations all four Frenkel states are included i.e. the higher states would possess mostly CT character.

ωB97xd/6-31+G(d) (FC)	*dimer*		*trimer*		*tetramer*	
state	exc. energy [eV]	qCT	exc. energy [eV]	qCT	exc. energy [eV]	qCT
1	2.66	0.05	2.61	0.07	2.59	0.07
2	2.96	0.04	2.76	0.06	2.67	0.08
3	3.05	0.95	2.98	0.96	2.83	0.09
4	3.06	0.97	3.00	0.33	2.96	0.96
5			3.00	0.63	2.96	0.96
6			3.12	0.96	3.02	0.05
7			3.15	0.96	3.06	0.96
8			3.77	0.25	3.07	0.97
9			3.84	0.28	3.16	0.96
10					3.16	0.94

Table 8.4: The vertical excitation energies in eV and the CT numbers (qCT) are given for a out-of-plane stack consisting of two, three or four monomers. The TD-ωB97xd/6-31+G(d) method was employed.

These variations resulting from the delocalization over more than two monomers and can be summarized in the following way. In the case of the trimer the two lowest states can be described as predominantly Frenkel ones and for the tetramer the three lowest state are of Frenkel type. Increasing the stack size the lowest excitation energy is down shifted, whereas for the dimer the excitation energy is 2.66 eV, the trimer one is 2.61 eV and the tetramer excitation energy is 2.59 eV. If one starts from the lowest excited state of the monomer which is predicted at 2.87 eV, the Davydov splitting leads to a red shift 0.22 eV (dimer), 0.26 eV (trimer) and 0.28 eV (tetramer) for the first excited state. The bright Frenkel state is shifted above one CT state for the trimer and two for the tetramer. For the trimer two states at 3.0 eV are observable which are mixtures of CT and Frenkel characters. This is underpinned by the CT numbers, the oscillator strengths and the electron-hole plots (see Figure 11.1.3). The prediction of the shift of the highest Frenkel state is hard to address, because of the strong interaction between the CT and Frenkel states. With respect to the monomer brightest excited state the dimer shift for the brightest state is 0.09 eV, the trimer state is shifted

by 0.13 eV and 0.15 eV for the tetramer. In the monomer the second excited state is 1 eV higher in energy. Therefore, the state manifold from the first and second excited state of the monomer starts to overlap for states above 3.5 eV. The 8^{th} and 9^{th} state are in the range of 0.3 eV with respect to 3.5 eV and no increase in the oscillator strength is observed. This may indicate that they have strong contributions arising from the state manifold with respect to the second excited state of the monomer.
The computation of even larger aggregates using the ωB97xd fails due to the computational effort. To get further information of larger aggregates the ZIndo(S) approach was tested in terms of accuracy. The results are summarized within Figure 8.2.11 and Table 8.5 (The results for the hexamer to nonamer systems can be found in the Appendix).

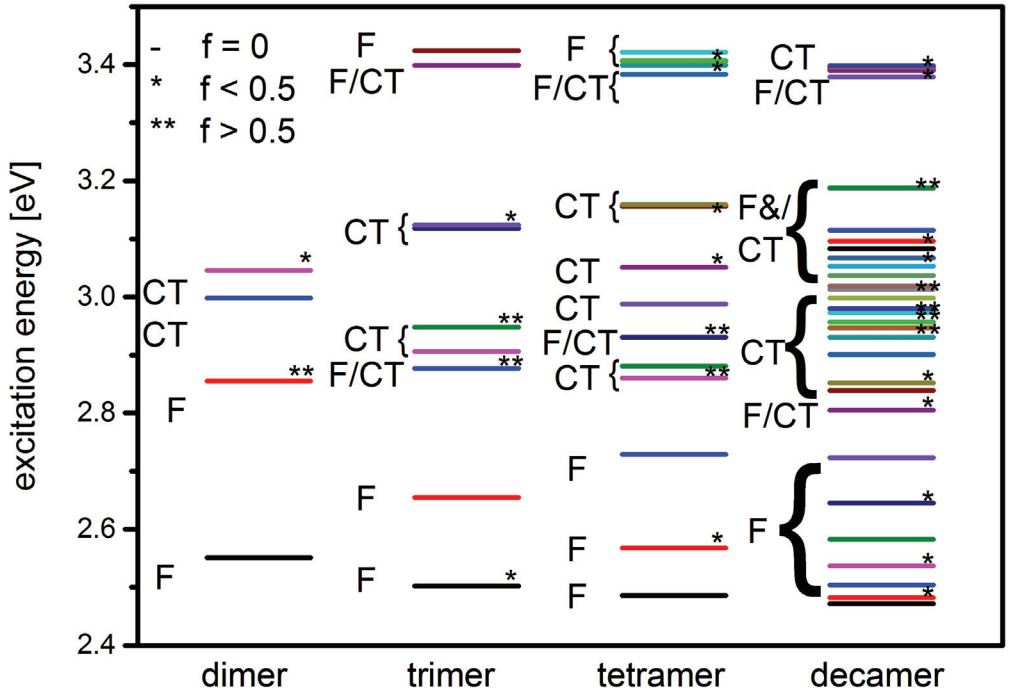

Figure 8.2.11: The vertical excitation energies in eV are given and the character of the states are indicated. The results are related to ZIndo(S) calculations. The systems are built by monomer units optimized on ωB97xd/TZVP level of theory and arranged in the FC geometry.

ZIndo(S)	*dimer*			*trimer*			*tetramer*			*decamer*		
state	exc. energy [eV]	osc.	qCT	exc. energy [eV]	osc.	qCT	exc. energy [eV]	osc.	qCT	exc. energy [eV]	osc.	qCT
1	2.55	0.00	0.06	2.50	0.02	0.10	2.49	0.00	0.13	2.47	0.00	0.20
2	2.86	1.79	0.10	2.66	0.00	0.06	2.57	0.05	0.13	2.48	0.00	0.17
3	3.00	0.00	0.94	2.88	1.52	0.47	2.73	0.00	0.13	2.50	0.00	0.22
4	3.05	0.14	0.90	2.91	0.00	0.90	2.86	0.53	0.87	2.54	0.01	0.19
5				2.95	0.95	0.63	2.88	0.00	0.93	2.58	0.00	0.20
6				3.12	0.20	0.91	2.93	2.20	0.36	2.65	0.05	0.22
7				3.12	0.00	0.91	2.99	0.00	0.92	2.72	0.00	0.28
8				3.40	0.00	0.44	3.05	0.45	0.76	2.81	0.36	0.58
9				3.42	0.00	0.15	3.16	0.19	0.84	2.84	0.00	0.92
10							3.16	0.00	0.91	2.85	0.06	0.90
11							3.38	0.00	0.52	2.90	0.00	0.59
12							3.40	0.00	0.51	2.93	1.47	0.83
13							3.41	0.00	0.17	2.95	0.00	0.95
14							3.41	0.00	0.19	2.96	2.11	0.76
15							3.42	0.00	0.11	2.97	0.72	0.89
16							3.42	0.00	0.11	2.97	0.00	0.97
17										2.98	0.00	0.93
18										3.00	0.66	0.88
19										3.01	0.00	0.86
20										3.02	0.00	0.91

Table 8.5: The vertical excitation energies, oscillator strengths and CT numbers (qCT) are shown. The out-of-plane FC stack are built by ωB97xd/TZVP monomers. The ZIndo(S) approach was used.

The ZIndo(S) results (dimer to the tetramer) and the ωB97xd values are in good accordance. The absolute value of the excitation energies are slightly lower (0.1 eV), whereas the CT number are slightly larger. Consequently, within the description of the mixing of states they differs to some extent, but the overall description is in a good agreement. Also the calculated Davydov splittings are equally well described by ωB97xd/6-31+G(d) and ZIndo(S). Using ZIndo(S) the downshift of the dimer first excited state relatively to the monomer first excited state (2.75 eV) can be calculated and is 0.20 eV. This is in good accordance to the ωB97xd/6-31+G(d) results (0.22 eV). The same trends are obtained for the trimer (0.25 vs. 0.26 eV) and the tetramer (0.26 vs. 0.28 eV). The blue shifts of the brightest states also compare quite well. In the row from dimer to tetramer the shifts are 0.11 eV, 0.13 eV and 0.18 eV for ZIndo(S) compared with 0.09 eV, 0.13 eV and 0.15 eV for ωB97xd/6-31+G(d). In consequence, we used ZIndo(S) to investigate even larger aggregates and estimate the characteristics of the excited states.

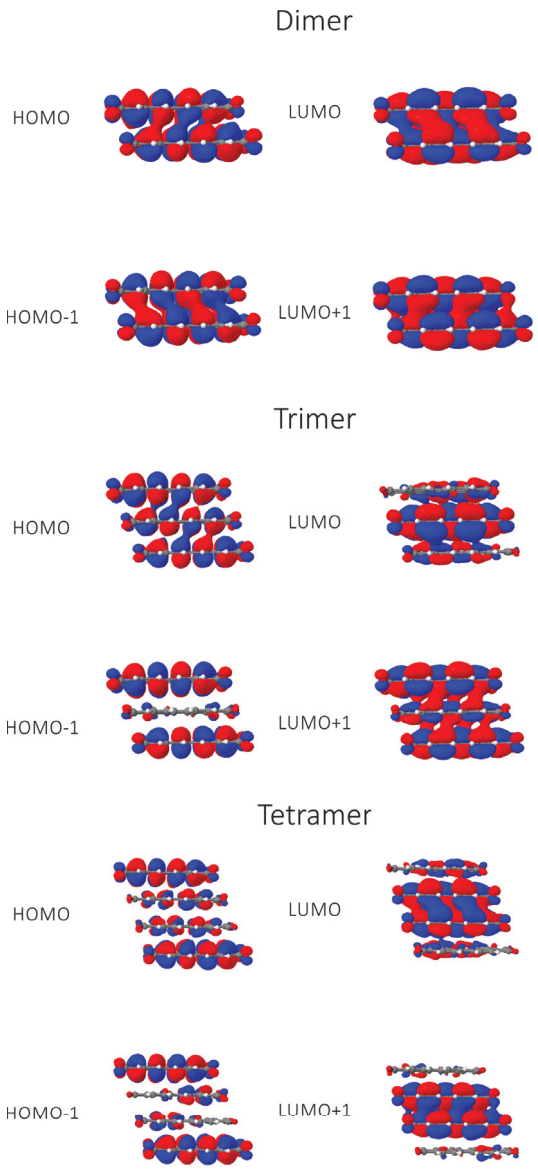

Figure 8.2.12: The MOs contributing at the first excited states for the dimer, trimer and tetramer in the out-of-plane (c-axis) stack (FC) are given on the basis of ωB97xd/6-31+G(d) calculations.

For the decamer (see Figure 8.2.11 and Table 8.5) out-of-plane stack the energy spacing between the 20 lowest state is lower than 0.1 eV in most cases. The lowest state lies at 2.47 eV and is only 0.08/0.02 eV lower than the dimer/tetramer first excited state. For the brightest state an even stronger mixing compared to the tetramer is obtained and the shift is difficult to estimate. The excitation energy (brightest state) of the decamer is of about 2.96

eV, which is 0.03 eV higher in relation to the tetramer. From these results one can conclude that the excitation energies are nearly converged for the tetramer description.

The character of the lowest excited states for the decamer of PTCDA is predominantly Frenkel like. Nevertheless, a slight increase of the CT amount is found going to larger stacks. Starting at a CT number of 0.06 for the dimer and ending with a CT number of 0.20 for the decamer. For the states in the middle energy range of the manifold a stronger mixing can be seen as for the tetramer. Therefore, in the energy interval from 2.9 eV till 3.0 eV four states with large oscillator strengths were obtained. This may lead to the assumption that the strong absorption band of PTCDA results from transitions into various electronic states. Making the assumption that the peak maximum can be assigned and the states might lay in the range of 2.5 eV up to 2.7 eV the absolute error of our model calculations is of about 0.3 eV. By downshifting the obtained excitation energies for this factor the first excited state of the decamer is located slightly below 2.2 eV. For this value the first peak in the absorption spectra can be found which is in line with our calculations.

One interesting fact is that by going from the dimer to the larger FC stacks or even larger aggregates, some of the lower Frenkel states gain intensity. For a better description of the spectra and get further insight exciton theory might help. This exciton model employs only Frenkel states. For calculating the excitation energies within this model one needs the monomer excitation energy E_m and the electronic coupling J. By using this input the energies of a N monomer consisting aggregate is calculated as follows:[202]

$$E(k,N) = E_m + 2Jcos\left(\frac{k\Pi}{N+1}\right), (k = 1, ...N)\,. \tag{8.2.3}$$

In case of positive values of J, the lowest energy is obtained at $k = N$ and the highest at $k = 1$. Using also vibrational degrees of freedom the oscillator strengths can be calculated as well.[203, 204, 205] The derive expressions can be simplified for the pure electronic case due to Brüning et al.[206]. For a parallel orientation of the transition dipole moments, whereas the intensity for the ground to the k-band in the excited state manifold can be formulated as:

$$I(N,k) = \frac{4\mu^2}{6(N+1)} \left(\frac{sin\left(x\left(N,k\right)\right)}{sin\left(\frac{x(N,k)}{3}\right)} \right)^2 (k = odd) \qquad (8.2.4)$$
$$I(N,k) = 0(k = even).$$

Within this equation μ describes the modulus of the monomer transition dipole moment, and the angle $x(N,k)$ is defined as:

$$x(N,k) = \frac{Nk\Pi}{2(N+1)}. \qquad (8.2.5)$$

Taking the trends from the equations described above the following can be summarized. By increasing the stack/aggregate size the excited state energy of the lowest state is shifted down and the energy of the highest state shifts up. For larger numbers of N one finds an energy gap of $4J$ between these states.

Within the QM calculations this trend is obtained for the lowest excited state, but related to the mixing of the Frenkel and CT states for higher energies the exciton model is not applicable. From Equation 8.2.4 the conclusion can be drawn that in aggregates consisting of an even number of states (monomers), transitions to the lowest state are strictly forbidden. This is in accordance with numerical calculations summarized in Table 8.4 and 8.5. We obtained that the hypsochromic bands in the various cases are the most intense ones but the transitions to lower bands occur leading to low intensity bands.

In Figure 8.2.13 the line spectra predicted by the exciton model and ZIndo(S) are compared. For the exciton model we applied the following parameters: $E_m = 2.70$ eV and $J = 0.15$. The chosen parameters give the best agreement with respect to the dimer. States with zero intensities are indicated by stars at the occurring energies. To provide better comparability the intensities were normalized to 1. Figure 8.2.13 illustrates that both approaches agree within their predictions. Differences arise from the CT states only, because they are neglected within the exciton model. In that way the distribution of the Frenkel oscillator strength over several interacting CT states is not included. Despite this, the resulting errors in the prediction of the band maximum are smaller than 0.1 eV.

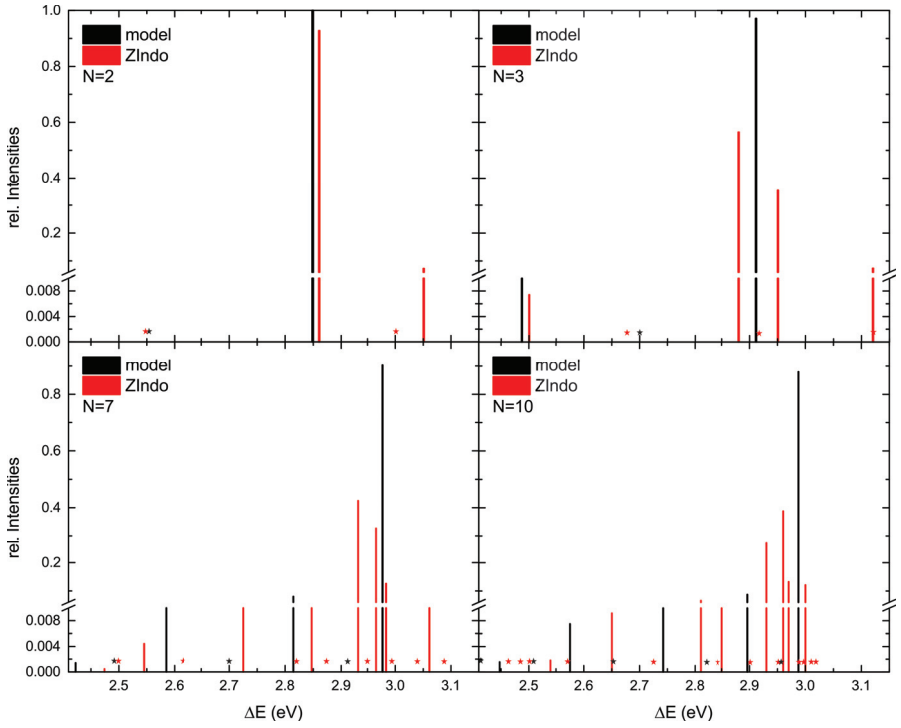

Figure 8.2.13: The line spectra for the simple exction model (black) and in comparison for the ZIndo(S) (red) calculations are depicted. For the model the following values have been used: $E_m = 2.70$ and $J = 0.15$. The intensities are normalized to 1 and states with no intensity are indicated by stars.

Up to this point, the focus laid on interactions within out-of-plane stacks (c-axis), but the interactions between the stacks have been neglected. For investigating their influence on the spectrum we start with the minimal system a dimer consisting of two molecules which are defined in the unit cell. This dimer lays in-plane (ab-axis) (see Figure 8.2.14). Due to their geometry they form a kind of J-aggregates i.e. the excitation to the lower band is allowed and to the upper band forbidden. This might be one possible explanation for the lower band in the experimental absorption spectrum located at about 2.2 eV. The calculated excitation energies, oscillator strengths and CT number are summarized in Table 8.6. For the dimer we found as expected intensity for the first excited state (high oscillator strength). In contrast to this the excitation to the upper state has no intensity. Despite of these findings the lower absorption band cannot be explained because the computed Frenkel states are too high in energy. This is related to the fact that the monomers are nearly 90° orientated with respect to each other which leads to a very small Davydov splitting. In consequence, the excitation energies of both states are close to the S1 excitation energy of the monomer (2.87 eV). Within

the tetramer as depicted in Figure 8.2.14 the interaction between the H-aggregate stacks is included . In this structure four molecules of two unit cells are aligned on top of each other. For this arrangement two neighboring out-of-plane stacks of the crystal are obtained, each built by an out-of-plane dimer. If one compares the results of the tetramer with the in-plane dimer (see Table 8.4) it is obvious that the coupling within the out-of-plane dimer is the dominating contribution. The first four states of the spectrum can be split into two pairs, whereas each pair is nearly degenerate. The energetically first pair stems from the interaction of the first two Frenkel states of both out-of-plane dimers. This can be assigned due to their excitation energies (2.64 and 2.66 eV) which are around the excitation energy of the lower Frenkel state of the single out-of-plane dimer (2.66 eV). In addition both states possess no transition moment (intensity). The excitation energies of the upper pair of states show only slightly lower excitation energies (2.89 and 2.93 eV) in comparison with the upper Frenkel state of the single out-of-plane dimer (2.96 eV). Both states have a considerable transition moment. Consequently, they can be related to the upper state of the single out-of-plane dimer, because of the interaction within the out-of-plane dimers which determines the oscillator strengths of the tetramer. The interaction between two out-of-plane stacks is not resulting in higher intensities for the lower states. By increasing the size of the clusters the situation does not change.

ωB97xd/6-31+G(d) (FC)	*dimer*			*tetramer*		
state	exc. energy [eV]	osc.	qCT	exc. energy [eV]	osc.	qCT
1	2.83	1.02	0.01	2.64	0.01	0.09
2	2.88	0.60	0.01	2.66	0.00	0.10
3	3.54	0.00	1.00	2.89	1.44	0.17
4	3.87	0.01	0.04	2.93	0.71	0.32
5				3.03	0.21	0.76
6				3.08	0.10	0.88
7				3.13	0.09	0.90
8				3.15	0.00	1.00
9				3.18	0.00	1.00
10				3.22	0.04	0.93

Table 8.6: Vertical excitation energies in eV, the oscillator strengths (osc.) and charge transfer numbers (qCT) of the dimer within the unit cell and a tetramer consisting of two such dimers on top of each other (see Fig 8.2.14) are given. All values were obtained employing the ωB97xd/6-31G+(d) level of theory.

The considerably weaker interaction which was found between two out-of-plane stacks is

in agreement with experimental data provided by Alonso et al.[207] and Engel et al..[208] In case of the former study the in-plane Davydov-splitting was assigned of about 37 meV by spectroscopy which matches the small difference calculated of about 20 meV for the S1 and S2 state of the given tetramer configuration (Table 8.6). Furthermore, the loss in luminescence anisotropy observed by Engel and coworkers is explainable in a consistent manner by our model, if one assumes the initially excited Frenkel state to be efficiently converted into the lower lying dark state on ultra-fast time-scales of a few hundred femtoseconds.[174]

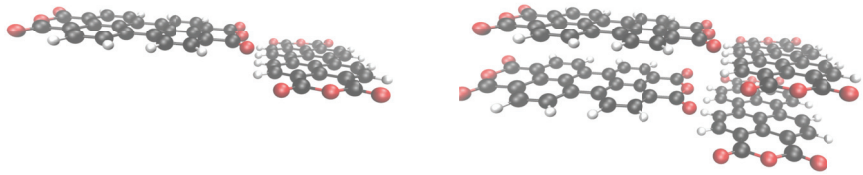

Figure 8.2.14: Left: The dimer of the unit cell. Right: The tetramer consisting of two unit cells on top of each other.

In our former study[174] about the lower Frenkel states which, for a perfect H-aggregate, have vanishing transition probabilities the assumption was made that an increasing intensity is due to vibrational motions. These vibrations induce weak geometrical distortions lead to the increase of the transition probability to the lower states. For further investigation of such effects, the vibrational spectra of monomer and dimer were calculated by using ωB97xd/6-31+G(d). The computations for larger aggregates were not possible due to the large computational effort. Unfortunately, the ZIndo(S) cannot be used to compute vibrations, although it provides accurate excitation spectra, it is worse for geometries.[209, 210] In Table 8.7 the variation in the electronic structure arising from an intra-monomer distortion of the upper monomer of a trimer is depicted. The variations are along various modes are taken from the monomer vibration. The structures lie 2 kcal/mol (distorted 20%) and 10 kcal/mol (distorted 40%) above the global minimum of the trimer. One fact to notice is the zero-point vibrational energy of the trimer which can be estimated to about 500 kcal/mol, i.e. the distortion is a very moderate one. Related to the results in Table 8.7 it can be clearly seen that due to the intra-monomer vibration, the oscillator strength of the lowest

state increases. Due to these findings intra-monomer vibrations seem to be the reason for the lower band of the absorption spectra of α-PTCDA crystals. The influence of inter-monomer motions only, seems to be smaller. Nevertheless, in combination both types of vibrations can well explain the intensity of the lower absorption band.
Surface relaxation might not have an influence on the experiments of Alonso[207] and Engel et al.[208] which were performed for large single crystals. Nonetheless, we simulated such effects and obtained a similar increase of the transition probability to the lowest state. If one would like to interpret the emission spectra it is important to notice that the CT states are not shifted below the Frenkel states even if relaxation processes are accounted. Related data can be found in the Appendix.

ωB97xD/6-31+G(d)	*trimer crystal*			*trimer (one) relax (20%)*			*trimer (one) relax (40%)*		
state	exc. energy [eV]	osc.	qCT	exc. energy [eV]	osc.	qCT	exc. energy [eV]	osc.	qCT
1	2.51	0.01	0.11	2.50	0.06	0.12	2.49	0.17	0.05
2	2.66	0.00	0.06	2.62	0.04	0.14	2.61	0.05	0.06
3	2.85	1.78	0.44	2.84	1.73	0.42	2.86	1.93	0.31
4	2.97	0.00	0.97	2.99	0.15	0.88	3.02	0.47	0.82

Table 8.7: The vertical excitation energies in eV, the oscillator strengths (osc.) and charge transfer numbers (qCT) are given. The results are related to a trimer in which the upper monomer is distorted (20, 40 %) along several vibrational coordinates. The 10% and 20% structures are about 2 and 10 kcal/mol above the crystal structure, respectively. All values were obtained with ZIndo(S).

8.2.4 Summary

Within the first part of this section it was shown for PBI that the influence of a polarizable solvent simulated by COSMO or IEFPCM plays only a minor role. The order of the excited states and related characters are determined by a distortion motion to the zwitterionic configuration, i.e. by intramolecular vibrations. It was also shown that a prediction of solvatochromic shifts based on cheaper methods like TD-HF is possible and trustworthy for many cases. Nevertheless, carefully characterizing the excited states nature might be recommended beforehand.

For the investigation of the spectral properties of crystalline PTCDA we applied different models and types of including the environment. Within all computations made the order of states found in gas phase calculations of various dimer configurations was confirmed. Indeed, the lowest excited state(s) seem(s) to be mostly of Frenkel type. The higher lying states posses CT character or mix with Frenkel type states. For an anisotropic environment we found within our QM/MM computations a stronger localization and a stronger mixing. Leaving the dimer ansatz and going to the explicit modeling of larger aggregates two effects were obtained. A strong coupling in H-aggregate like stacks versus a very weak coupling of J-aggregate orientations. It was shown that the spectra can be explained using simple models like exciton model or ZIndo(S) calculations if one takes also further degrees of freedom like vibrations into account.

Chapter 9

Summary

Two thematic complexes were addressed within this work. One part is related to improvements and new implementations into the CAST program package. Thereby the main focus laid on the delivery of a tool which can be used to characterize complex reactions and their mechanisms. But also within the new force field (FF) method (SAPT-FF) within the CAST program, several improvements were made. The second topic is related to the description of dye molecules and their spectral properties. The main focus within these studies was set on the influence of the environment on these properties.

In the first topic improvements of the local acting NEB (nudged elastic band) methods were included and the number of available methods was extended. The initial pathway generation was improved by implementing the IDPP (image dependent pair potential) method and a new method was implemented for describing temperature dependent pathways. Additionally, improvements have been made to the optimization routines (global NEB).

As a second part the Pathopt (PO) method was considerably improved. In the beginning of the work the original PO idea was used. In this approach one starts with a global optimization on one n-1 dimensional hyperplane which divides the reaction into two sub-areas for obtaining guesses of TSs (transition states). These found TS guesses were used to optimize to the "true" TS. Starting from the optimized ones a relaxation to the next connected minima is done. This idea has been automatically implemented and extended to several number of hyperplanes. In this manner a group of pathsegments is obtained which needs to be connected, but within this work it was realized that such a procedure might be not very efficient. Therefore, a new strategy was implemented which is founded on the same constrained global optimization scheme (MCM) for which the user defines the number of hyperplanes generated. The number of such generated hyperplanes should be large enough

to describe the space between the concerning reactants in a sufficient way. The found minima are directly used to built up the reaction pathway. For this purpose a RMSD (root mean square deviation) criterion is used to walk along ways of minimal change from one to another hyperplane. To prove the implementations various test calculations were carried out and extensions included to prove the capabilities of the new strategy. Related to these tests a new strategy for applying the move steps in MCM (Monte Carlo with minimization) was realized which is also related to the question of the coordinates representation. We were able to show that the hopping steps in MCM can be improved by applying Cartesian steps in combination of random dihedral moves with respect to the constraint. In this way it was possible to show that a large variety of systems can be treated.
An additional chapter shows the improvements of the SAPT-FF implementation and related test cases. It was possible to treat benzene dimer and cluster systems of different sizes consistently also in accordance with high level *ab initio* based approaches. Furthermore, we showed that the SAPT-FF with the right parameters outperforms the standard AMOEBA implementation which is the basis of the SAPT-FF implementation.
In the last three chapters deal with the description of perlyene-based dyes. In the first smaller chapter ground state chemistry description of macro cycles of PBI (perylene bisimide) derivatives were investigated. Therefore, AFM (atomic force microscopy) based pictures were explained within our study. The methods to explain aggregation behavior in dependency of the ring size were MD simulations and configuration studies.
The last two chapters deal with opto-electronic or photo-physical properties of PBI and PTCDA (perylene-3,4,9,10-tetracarboxylic dianhydride). In detail, we investigated the role of the environment and the aggregate or crystal surrounding by applying different models. In that way implicit and explicit solvation models, the size of aggregates and vibration motions were used. In the case of PBI the recent work is found on preliminary studies related to my bachelor thesis and extends it. It was shown that the direct influence of a polarizable surrounding, as well as explicit inclusion of solvent molecules on the overall description of the excitations and nature of the excited states is weaker as one might expect. However the inclusion of intra-molecular degrees of freedom showed a stronger influence on the state characteristics and can induce a change of the order of states within the dimer picture. For the PTCDA molecule the main focus was set on the description of the absorption spectrum of crystalline thin films. Related to this older works exist which already gave a description and assignment of the absorption band, but are based on different approaches compared to the one used in this work. We used the supermolecule ansatz, whereas the environment and different aggregate sizes were investigated. Within the dimer based approach we were

able to show that using continuum solvation (IEFPCM/COSMO) based description for the environment the relative order of states remains unchanged. Similar to the PBI calculations the influence of the vibrational motions /distortions is larger. The simulation of the crystal environment by using QM/MM (quantum mechanics/molecular mechanics) approaches delivered that an asymmetric charge distribution might induce a localization of the excitation and a stronger mixing of states. For obtaining further insights we go beyond the dimer picture and aggregates of different sizes were used, whereas the simulations up to the octadecamer mono- and even dual-layer stack were carried out. Within these calculations it was shown that the H-coupling is dominating over a weaker J-coupling between different stacks. Additionally the calculations based on DFT (density functional theory) and semi-empirics showed that the lowest state in terms of energy are mostly of Frenkel type, whereas the higher lying states are CT ones which mix with embedded Frenkel type states. The first band of the absorption spectrum was explained by inclusion of vibrational motions within the stacks which induce an intensity gain of the first excited state. This intensity was not explainable by using the undistorted stacks. Also relaxations at the crystal surface might play a role, but are experimentally not explainable.

9.1 Zusammenfassung

In der Arbeit wurden zwei große Themenkomplexe bearbeitet. Zum einen wurden Verbesserungen und neue Methoden in CAST, unserem Entwicklungstool, implementiert. Hierbei geht es vor allem darum ein Werkzeug bereit zu stellen, mit dem es möglich ist Reaktionen genauer zu charakterisieren. Aber auch neue Beschreibungen innerhalb der Kraftfeldmethoden (SAPT-FF) wurden bereitgestellt bzw. erweitert. Der zweite Themenkomplex behandelt die Beschreibung von Farbstoffmolekülen und ihrer spektralen Eigenschaften. Insbesondere liegt in dieser Studie der Fokus auf Umgebungseinflüsse.
Im ersten Abschnitt wurden Erweiterungen in den lokalen Methoden, die auf NEB (nudged elastic band) basieren, implementiert. Hier wurde zum einen das Spektrum an Methoden erweitert. So wurde der initiale Vorschlag für den Startpfad durch Implementierung der IDPP (image dependent pair potential) Methode verbessert. Des Weiteren wurde eine Methode zur temperaturabhängigen NEB Beschreibung integriert, die auf Maximierung des Fluxes beruht. Auch wurden Verbesserungen hinsichtlich der Optimierungsroutinen durchgeführt. Der wesentliche Teil im ersten Themenbereich beschäftigt sich mit der Verbesserung und Automatisierung von Pathopt (PO).

Zu Beginn der Arbeit wurde die ursprüngliche Idee aufgegriffen. Hierbei ermittelt man Vorschläge für Übergangszustände (ÜZ) durch eine globale Optimierung mit Nebendbedingungen auf einer n-1 dimensionalen Hyperfläche, die den Reaktionsraum teilt. Diese ÜZ bilden den Startpunkt, um mittels einer "*uphill*" Optimierung hin zum "wirklichen ÜZ" zu gelangen. Ausgehend von diesen wurde in die nächst verknüpften Minima relaxiert. Diese Idee wurde automatisiert und auf mehrere Hyperflächen ausgeweitet. So erhält man eine Schar an Pfadsegmenten, die verknüpft werden müssen. Im Laufe der Arbeit, stellte sich jedoch heraus, dass diese Vorgehensweise nicht sehr effizient ist und daher wurde eine neue Idee verwirklicht. Diese beruht wiederum auf der globalen Optimierung mittels Monte Carlo mit Minimierung und Nebenbedingungen auf einer vom Nutzer bestimmten Anzahl an n-1 dimensionalen Hyperflächen. Nun wählt man diese Anzahl entsprechend groß genug aus, um den Raum zwischen den Reaktanden zu beschreiben. Die so gefundenen Mininima auf den n-1 Hyperflächen werden für die direkte Pfaderzeugung genutzt. Dies geschieht mittels eines RMSD (root mean square deviation) Kriteriums, um so den Weg der geringsten Änderungen anhand der Hyperflächen zu wählen. Im Zuge der Implementierung der Methode wurden zahlreiche Testrechnungen und Methodenerweiterungen durchgeführt, um die Funktionalität zu überpüfen und zu verbessern. Diese Verbesserungen liegen zum Bsp. in den Sprungstrategien bzw. der Wahl des Koordinatensystems. Hier konnte gezeigt werden, dass eine Verbindung unterschiedlicher Strategien für die Durchführung des "Hüpfens" in Monte Carlo zu entscheidenden Verbesserungen führt. Diese Verbesserung besteht in der Verknüpfung von Kartesischen Schritten und zufälliger Veränderungen der Diederwinkel im Rahmen der Nebenbedingungen. Mit Hilfe dieser Verbesserungen konnte eine Vielzahl von Systemen behandelt werden.

Ein weiteres Kapitel beschreibt Verbesserungen zum SAPT-FF (FF=Kraftfeld). Testrechnungen zu strukturellen Eigenschaften von Benzol Clustern belegen die Genauigkeit der Ansätze. Auch wurde aufgezeigt, dass das SAPT-verbesserte AMOEBA Kraftfeld der Standard Para-metrisierung überlegen ist.

Die letzten drei Abschnitte dieser Arbeit behandeln Perylen-basierte Farbstoffe. In einem ersten kleinen Kapitel geht es um die Grundzustandseigenschaften von PBI (Perylenbisimide) Makrozyklen und Erklärung von AFM (Atomic Force Mycroscopy) Messungen. Hier konnten wir mittels MD-Simluation (Molekular Dynamik) und deren Analyse, sowie Beschreibungen unterschiedlicher Konfigurationen, das Aggregationsverhalten in Abhängigkeit der Ringgröße genauer beleuchten.

In den beiden letzten Kapiteln geht es um die optoelektronischen Eigenschaften bzw. die photophysikalische Beschreibung von PBI und PTCDA (Perylen-3,4,9,10-Tetracarboxyl Di-

anhydrid). Im Genaueren wurde die Rolle der Umgebung in Aggregat und Kristall durch unterschiedliche methodische Ansätze untersucht. So wurden implizite Solvensmodelle und explizite Solvatation, Aggregatgröße und vibronische Freiheitsgrade untersucht. In den Arbeiten zum PBI konnte gezeigt werden, dass ein direkter Einfluss durch die Beschreibung mittels impliziter Solvatation, als auch expliziter Solvensmoleküle, auf die Lage der Zustände auch in Hinsicht auf deren Charakterisik nicht auftritt. Berücksichtigt man intra-molekulare Freiheitsgrade, so wird die Lage der Zustände deutlich stärker beeinflusst und sogar ein Wechsel der Zustände wird induziert. Im Fall von PTCDA lag vor allem die Beschreibung und Erklärung der Absorptionsspektren von kristallinem PTCDA im Fokus. Hierzu gibt es ältere Arbeiten, die bestimmte Zurodnungen der Banden und ihrer Übergänge postuliert haben. In dieser Arbeit sollte diese Beschreibung im Rahmen eines Supermolekül Ansatzes geklärt und weiter beschrieben werden, wobei Umgebungseinflüsse und auch Eigenschaften verschiedener Aggregate untersucht wurden. Im Dimer Bild konnten wir zeigen, dass die Umgebung, beschrieben durch Continuums Ansätze (IEFPCM/COSMO) die Lage der Zustände nicht beeinflusst und im Wesentlichen nur Zustände mit großer Oszillatorstärke stabilisiert werden. Ähnlich wie im Falle des PBIs hat die Berücksichtigung vibronischer Freiheitsgrade einen wesentlich größeren Einfluss. Die Simulation der Kristallumgebung durch QM/MM-Ansätze (Quantenmechanik/Molekularmechanik) ergab, dass eine asymmetrische Ladungsverteilung zu einer Lokalisierung der Anregung und einem stärkeren Durchmischen der Zustände führt. Für eine noch weitergehende Beschreibung wurde das Dimer Bild verlassen und unterschiedliche Aggregate, bis hin zum Oktadekamer im mono- bzw zweifach-Lagen-Aggregat untersucht. Hier konnte gezeigt werden, dass die Kopplung im H-Aggregat die dominierende Rolle einnimmt und die J-Aggregat Kopplung vernachlässigt werden kann. Zudem zeigen die Rechnungen, die mittels DFT (Dichtefunktionaltheorie) und semi-empirischen Ansätzen durchgeführt wurden, dass die energetisch niedriger liegenden Zustände im wesentlichen Frenkel Charakter aufweisen während die energetisch höher liegenden Zustände CT (Charge Transfer) Charakter haben. Das Auftreten der ersten Bande im Absorptionsspektrum wurde zudem auf das Vorhandensein von möglichen Schwingungsanregungen (mehrere Moden) zurückgeführt, da diese zu einer Zunahme an Intensität des ersten angeregten Zustandes führen, die ohne Berücksichtigung nicht in diesem Maße erhalten wird. Auch könnten Oberflächenrelaxationen eine Rolle spielen, wobei diese experimentell nicht beobachtbar sind.

Chapter 10

Acknowledgment

Zu aller erst möchte ich mich bei meinem Doktorvater Prof. Dr. Bernd Engels bedanken, der es mir ermöglicht hat an zwei sehr interessanten Themen zu arbeiten, um so auf der einen Seite Programmentwicklung zu betreiben und auf der anderen Seite die Natur organischer Halbleiter zu untersuchen. Er stand mir immer mit Rat und Tat zur Seite, ermöglichte es mir eigenen Ideen nachzugehen und unterstützte dies immer. Auch über den Tellerrand der Arbeit hinaus war es ein unglaublich schönes Gefühl Mitglied eines so tollen Arbeitskreises zu sein.
Womit ich auch zum Dank an eben diesen wunderbaren Arbeistskreis Engels komme, in dem es an Zusammenhalt nie mangelte. So erhielt man das Gefühl, Teil einer wundervollen wissenschaftlichen Familie zu sein. Ganz speziell möchte ich hier auch Uschi danken, die wohl beste "Chefin" neben dem Chef und gute Seele des Hauses. Vielen Dank dafür, dass sie mir auch über die Arbeit hinaus mit Rat und Tat zur Seite stand.
Es gibt nur wenig sehr gute Freunde und nur einen Besten. Thien Anh möchte ich für Alles danken, für die Unterstützung, die freien Stunden und natürlich für die Korrekturarbeit.
Zum Schluss, möchte ich meiner Familie danken, die mich durch diese turbulente Zeit getragen hat. Meiner Mutter, meinem Vater, Peter und meiner Oma gilt der Dank, in nicht immer leichten Zeiten. Mit ihrem fürsorglichen Rat standen sie mir stets zur Seite. Natürlich gebührt vor Allem auch der Dank meiner geliebten Frau Veronika, die überaus geduldig war und die Anstrengungen der Jahre in Liebe verwandelt hat. Auch Sophie und Walter möchte ich für die großartige Unterstützung danken.

Chapter 11

Appendix and References

11.1 Appendix

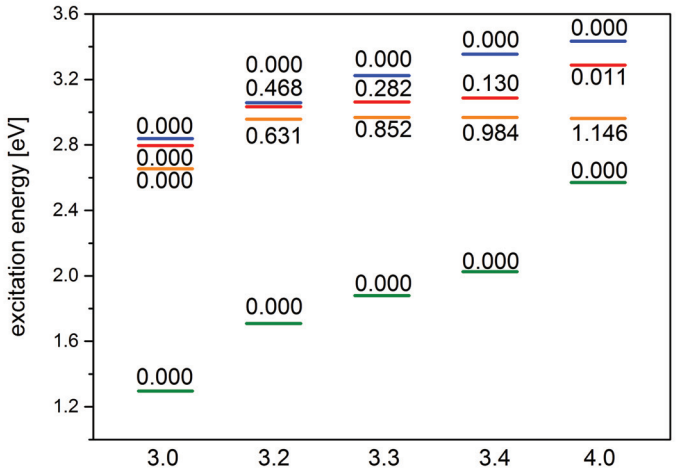

Figure 11.1.1: The excitation energies and related oscillator strengths are shown for various parallel stacked PTCDA dimer configuration. On the y-axis the numbers indicate parallel shifts along the stacking axis in Å. The calculations were carried out by using ωB97xd/6-31+G(d).

monomer *ωB97xd/TZVP* state	*ωB97xd/TZVP* *vacuum* exc. energy [eV]	osc.	*ωB97xd/TZVP* *small ESP* exc. energy [eV]	osc.	*SCS-ADC(2)/SVP* *vacuum* exc. energy [eV]	osc.	*TD-HF/TZVP* *vacuum* exc. energy [eV]	osc.	*TD-HF/TZVP* *small ESP* exc. energy [eV]	osc.
1	2.87	0.73	2.79	0.71	3.10	0.85	3.14	0.85	3.15	0.85
2	3.90	0.00	3.82	0.00	3.77	0.00	4.42	0.00	4.43	0.00
3	4.12	0.09	3.90	0.00	4.02	0.06	4.55	0.00	4.56	0.00
4	4.13	0.00	4.03	0.01	4.31	0.00	4.68	0.15	4.70	0.12

Table 11.1: The excitation energies in eV and oscillator strengths (osc.) are given for PTCDA monomers in different surroundings and for different QM approaches. The small EPS results refer to calculations by using a charge field obtained on the basis of ωB97xd/TZVP derived charges of the neutral monomer configuration. The underlying geometry was obtained by using ωB97xd/TZVP.

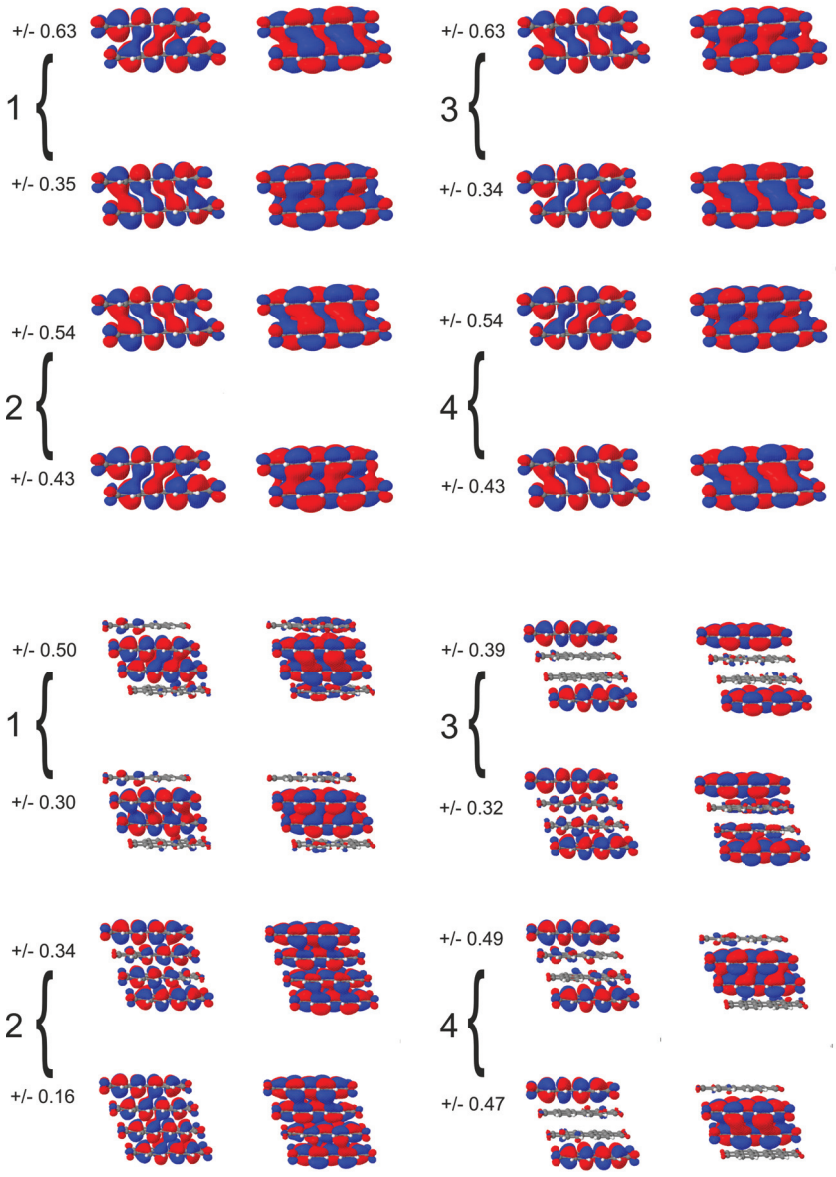

Figure 11.1.2: On top the NTOs of the FC dimer configuration are depicted. On the bottom the NTOs of the FC tetramer configuration are shown. On the right side of each pair the particle and on the right side the hole contribution is given. The λ values are assigned to each pair of contributions and the isovalue is set to 0.01. The calculations were carried out on TD-ωB97xd/6-31+G(d) level of theory by using the optimized ωB97xd/TZVP monomers.

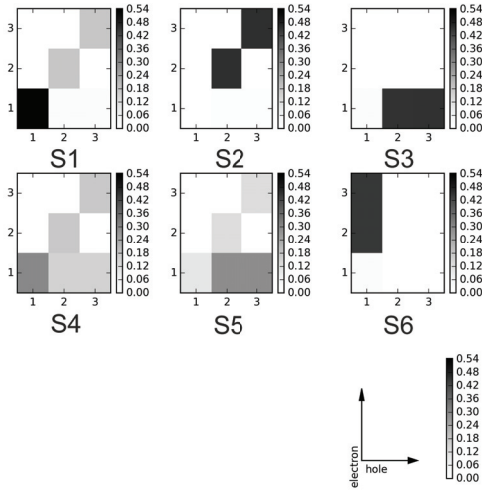

Figure 11.1.3: The electron-hole correlation plots of the Omega matrices for the first six singlet states are given. The results are obtained for the out-of-plane trimer stack calculated with TD-ωB97XD//6-31+G(d).

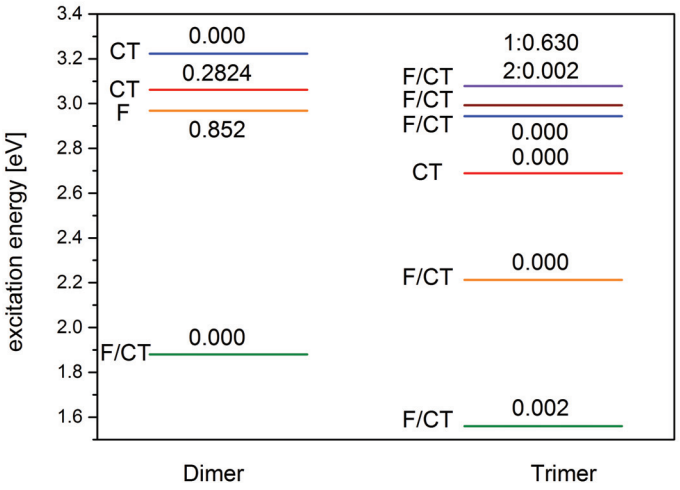

Figure 11.1.4: The vertical excitation energies in eV are given for the dimer and trimer of PTCDA. The systems are built by monomer units optimized on ωB97xd/TZVP level of theory and arranged in the parallel H-aggregate like form. The excitations were treated by using the TD-ωB97xd/6-31+G(d) approach

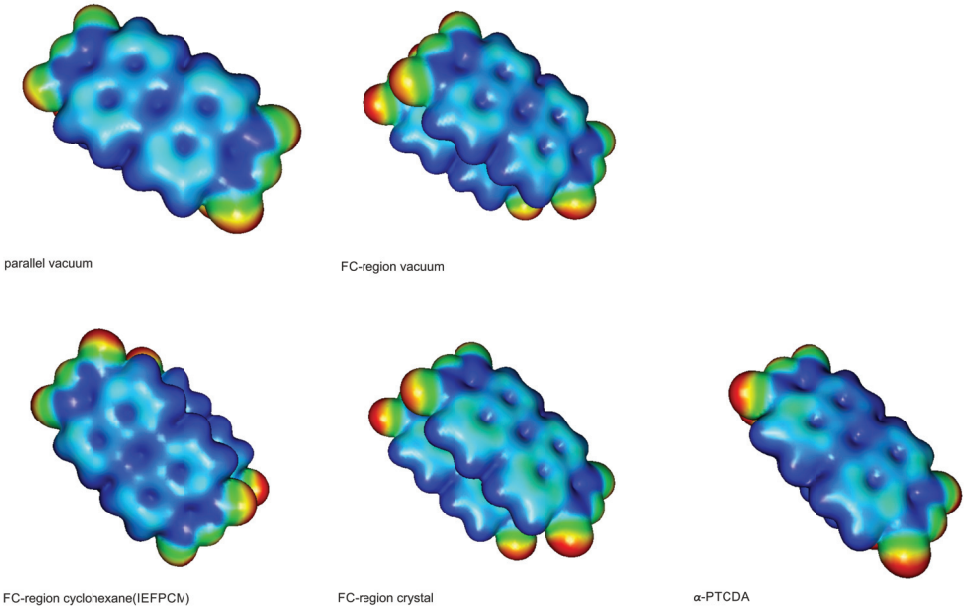

Figure 11.1.5: The charge densities for the PCTDA dimer arrangements in different configurations and environments are shown. The red color indicates negative and the blue one positive charge densities.

ZIndo(S)	*hexamer (small cell)*			*hexamer (small cell) relaxed*		
state	exc. energy [eV]	osc.	qCT	exc. energy [eV]	osc.	qCT
1	2.48	0.01	0.16	2.31	0.41	0.08
2	2.51	0.01	0.10	2.34	0.47	0.03
3	2.63	0.01	0.13	2.54	0.02	0.09
4	2.66	0.04	0.16	2.58	0.02	0.10
5	2.79	1.07	0.85	2.79	2.80	0.25
6	2.81	1.67	0.71	2.84	1.29	0.34
7	2.84	0.86	0.51	2.90	0.00	1.00
8	2.91	0.05	0.97	2.99	0.10	0.97
9	2.96	0.06	0.97	3.01	0.19	0.91
10	2.98	0.09	0.94	3.03	0.04	0.98
11	2.98	0.69	0.72	3.05	0.02	0.96
12	3.02	0.29	0.89	3.06	0.02	0.95
13	3.03	0.04	0.98	3.08	0.06	0.93
14	3.04	0.19	0.95	3.12	0.00	0.96
15	3.10	0.04	0.91	3.15	0.20	0.88
16	3.16	0.03	0.98	3.15	0.04	0.93

Table 11.2: The excitation energies in eV, oscillator strengths (osc.) and charge transfer numbers (qCT) of a hexamer taken from the crystal in comparison to a hexamer that includes surface relaxation are given. All values were obtained with ZIndo(S).

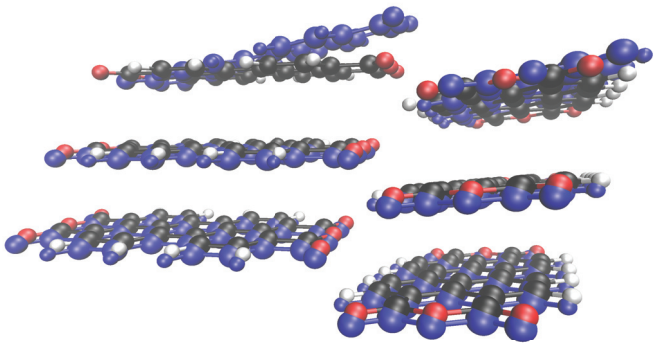

Figure 11.1.6: The hexamer cut out of the surface of the QM/MM cluster in which the upper two layers were allowed to relaxed is indicated by blue structures. The non-relaxed hexamer is given in black.

ZIndo(S)	*hexamer*			*heptamer*			*octamer*			*nonamer*		
state	exc. energy [eV]	osc.	qCT	exc. energy [eV]	osc.	qCT	exc. energy [eV]	osc.	qCT	exc. energy [eV]	osc.	qCT
1	2.476	0.000	0.139	2.474	0.002	0.138	2.473	0.000	0.149	2.472	0.001	0.179
2	2.509	0.011	0.114	2.498	0.000	0.115	2.491	0.004	0.136	2.486	0.000	0.191
3	2.576	0.000	0.113	2.545	0.019	0.122	2.525	0.000	0.139	2.513	0.007	0.212
4	2.682	0.130	0.152	2.620	0.000	0.162	2.580	0.029	0.209	2.554	0.000	0.256
5	2.810	0.000	0.488	2.725	0.180	0.188	2.659	0.000	0.192	2.614	0.040	0.199
6	2.848	0.252	0.930	2.826	0.000	0.766	2.759	0.236	0.240	2.693	0.000	0.271
7	2.867	0.000	0.735	2.847	0.195	0.972	2.833	0.000	0.929	2.785	0.299	0.405
8	2.930	1.832	0.692	2.874	0.000	0.624	2.847	0.144	0.959	2.836	0.000	0.917
9	2.960	0.000	0.936	2.930	1.820	0.712	2.884	0.000	0.516	2.849	0.098	0.936
10	2.967	1.479	0.644	2.948	0.000	0.909	2.930	1.603	0.798	2.893	0.000	0.465
11	2.990	0.000	0.912	2.965	1.400	0.748	2.948	0.000	0.923	2.930	1.554	0.818
12	3.042	0.103	0.916	2.983	0.540	0.899	2.959	1.629	0.799	2.946	0.000	0.955
13	3.076	0.000	0.881	2.994	0.000	0.892	2.976	0.000	0.959	2.959	2.062	0.749
14	3.093	0.853	0.733	3.034	0.000	0.917	2.986	0.945	0.822	2.974	0.000	0.949
15	3.179	0.000	0.863	3.061	0.132	0.889	3.003	0.000	0.885	2.975	0.169	0.961
16	3.181	0.222	0.839	3.085	0.000	0.890	3.028	0.001	0.920	2.992	0.798	0.823

Table 11.3: The excitation energies in eV, oscillator strengths and CT numbers are depicted for various out-of-plane stacks computed with ZIndo(S).

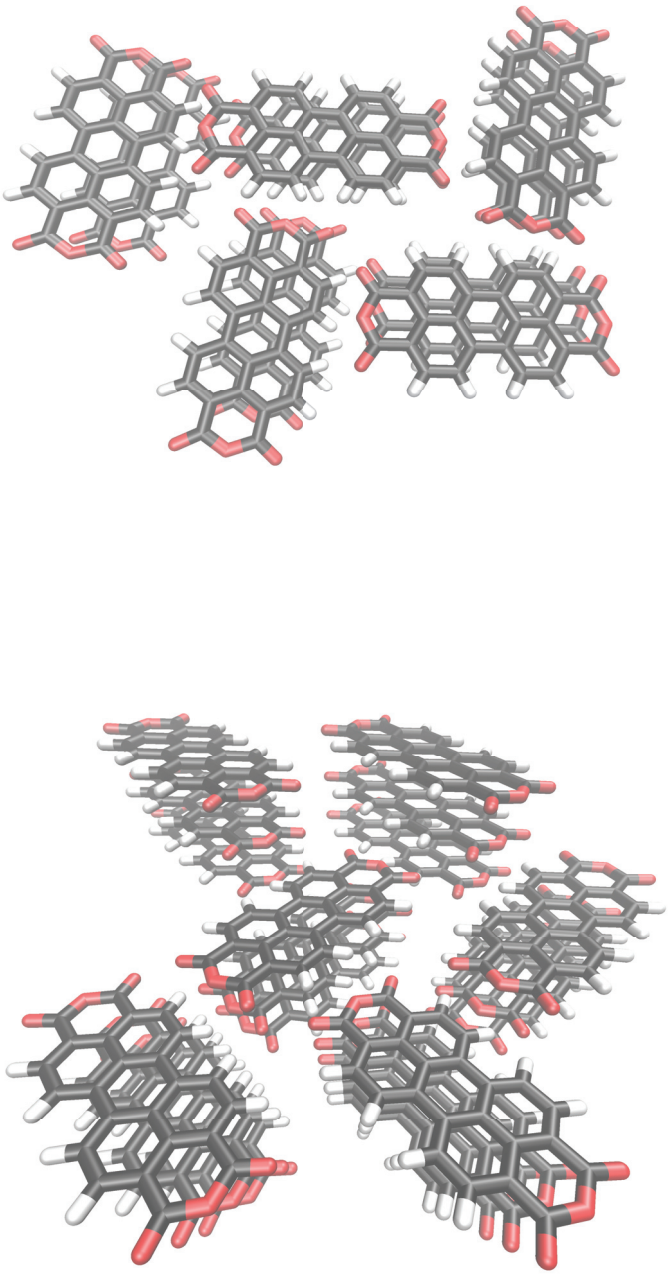

Figure 11.1.7: Top: The dual-layer pentamer consisting of momoners which are oriented as in a layer of the α-PTCDA crystal is given. Bottom: The octadecamer with three layer of the α-PTCDA crystal is given, whereas each contains six PTCDA units.

ZIndo(S)	*pentamer (one layer)*			*decamer (two pentamer layers)*			*octadecamer (three hexamer layers)*		
state	exc. energy [eV]	osc.	qCT	exc. energy [eV]	osc.	qCT	exc. energy [eV]	osc.	qCT
1	2.67	1.76	0.05	2.49	0.00	0.14	2.45	0.01	0.28
2	2.67	1.18	0.05	2.51	0.02	0.15	2.46	0.00	0.24
3	2.72	0.08	0.02	2.53	0.02	0.14	2.47	0.02	0.22
4	2.74	0.25	0.03	2.54	0.00	0.16	2.48	0.01	0.31
5	2.76	2.61	0.06	2.55	0.00	0.08	2.49	0.01	0.19
6	3.31	0.00	0.47	2.70	0.13	0.33	2.58	0.01	0.13
7	3.36	0.01	0.45	2.72	4.39	0.41	2.60	0.14	0.25
8	3.40	0.01	0.50	2.76	0.48	0.50	2.63	0.02	0.20
9	3.41	0.02	0.66	2.80	0.34	0.53	2.63	0.04	0.31
10	3.43	0.01	0.56	2.82	2.30	0.51	2.63	0.15	0.12
11	3.49	0.00	0.25	2.93	0.21	0.86	2.65	0.25	0.26
12	3.49	0.06	0.26	3.94	0.38	0.86	2.66	0.03	0.18
13	3.52	0.02	0.19	2.96	0.47	0.78	2.75	0.11	0.80
14	3.53	0.00	0.10	2.97	0.53	0.79	2.75	1.00	0.57
15	3.53	0.01	0.21	2.98	0.60	0.81	2.75	1.93	0.69
16	3.53	0.03	0.22	3.18	0.17	0.92	2.81	0.26	0.72
17	3.53	0.00	0.15	3.19	0.08	0.91	2.82	0.88	0.53
18							2.83	2.95	0.58
19							2.88	0.82	0.74
20							2.89	1.78	0.63
21							2.92	0.12	0.78
22							2.92	0.12	1.00
23							2.94	1.05	0.65
24							2.94	0.02	0.92

Table 11.4: The singlet vertical excitation energies in eV, the oscillator strengths (osc.) and CT numbers (qCT) of pentamer, decamer and octadecamer are depicted. All values were obtained by using the ZIndo(S) approach.

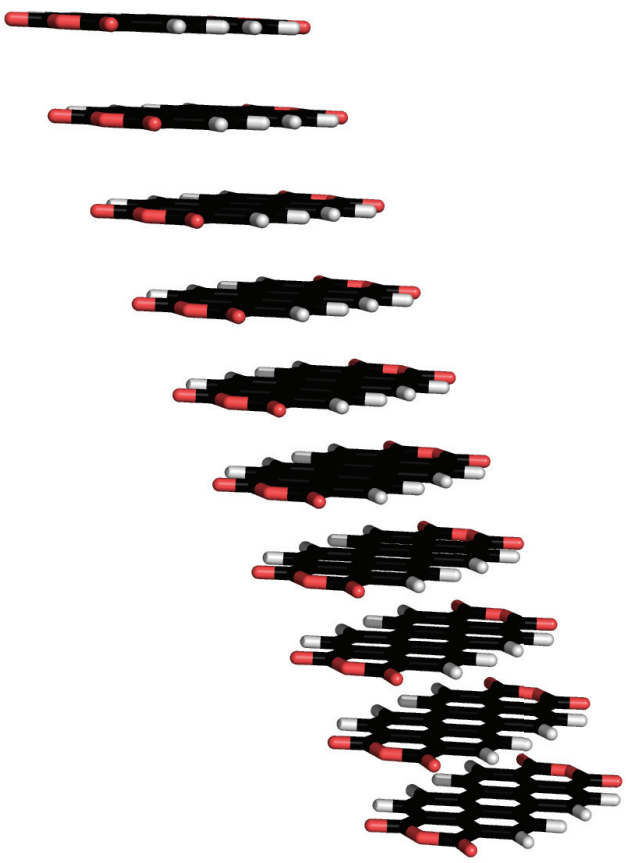

Figure 11.1.8: The structure of the decamer out-of-plane stack is shown which is built by monomers optimized on ωB97xd/TZVP level of theory.

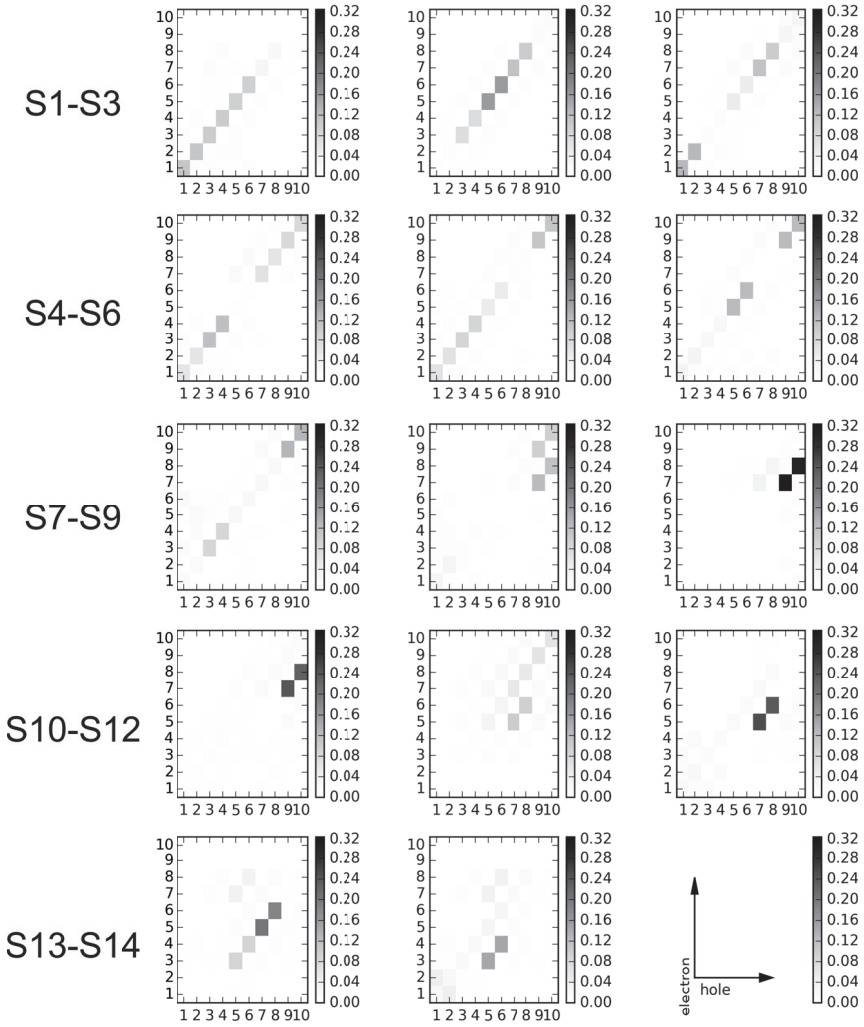

Figure 11.1.9: The electron-hole correlation plots of the Omega matrices for the first 14 singlet states are given. The results are obtained for the out-of-plane decamer stack calculated with ZIndo(S).

Bibliography

[1] C. Grebner, Ph.D. thesis, University of Wuerzburg, **2012**.

[2] Z. Li, H. A. Scheraga, *Proceedings of the National Academy of Sciences* **1987**, *84*, 6611–6615.

[3] R. Crehuet, M. J. Field, *Journal of Chemical Physics* **2003**, *118*, 9563–9571.

[4] S. Smidstrup, A. Pedersen, K. Stokbro, H. Jonsson, *Journal of Chemical Physics* **2014**, *140*, 214106.

[5] J. W. Ponder, C. Wu, P. Ren, V. S. Pande, J. D. Chodera, M. J. Schnieders, I. Haque, D. L. Mobley, D. S. Lambrecht, R. a. DiStasio, M. Head-Gordon, G. N. I. Clark, M. E. Johnson, T. Head-Gordon, *J. Phys. Chem. B* **2010**, *114*, 2549–64.

[6] Y. Shi, Z. Xia, J. Zhang, R. Best, C. Wu, J. W. Ponder, P. Ren, *Journal of Chemical Theory and Computation* **2013**, *9*, 4046–4063.

[7] D. Kaiser, Bachelor thesis, University of Wuerzburg, **2015**.

[8] D. J. Wales, H. A. Scheraga, *Science* **1999**, *285*, 1368–1372.

[9] D. Weber, D. Bellinger, B. Engels, *Methods in Enzymology* **2016**, *578*, 145–167.

[10] J. Zhang, M. Dolg, *Physical Chemistry Chemical Physics* **2016**, *18*, 3003–3010.

[11] J. B. Davis, S. L. Horswell, R. L. Johnston, *The Journal of Physical Chemistry C* **2016**, *120*, 3759–3765.

[12] L. Piela, J. Kostrowicki, H. A. Scheraga, *The Journal of Physical Chemistry* **1989**, *93*, 3339–3346.

[13] G. Henkelman, G. Jóhannesson, H. Jónsson in *Theoretical Methods in Condensed Phase Chemistry*, Springer, **2002**, pp. 269–302.

[14] R. Olsen, G. Kroes, G. Henkelman, A. Arnaldsson, H. Jónsson, *The Journal of chemical physics* **2004**, *121*, 9776–9792.

[15] A. Banerjee, N. Adams, J. Simons, R. Shepard, *Journal of Physical Chemistry* **1985**, *89*, 52–57.

[16] G. Henkelman, H. Jonsson, *Journal of Chemical Physics* **1999**, *111*, 7010–7022.

[17] R. Elber, M. Karplus, *Chemical Physics Letters* **1987**, *139*, 375–380.

[18] G. Henkelman, H. Jonsson, *Journal of Chemical Physics* **2000**, *113*, 9978–9985.

[19] I. F. Galvan, M. J. Field, *Journal of Computational Chemistry* **2008**, *29*, 139–143.

[20] W. Quapp, *Journal of Chemical Physics* **2005**, *122*.

[21] B. Peters, A. Heyden, A. T. Bell, A. Chakraborty, *Journal of Chemical Physics* **2004**, *120*, 7877–7886.

[22] D. J. Wales, *Molecular Physics* **2002**, *100*, 3285–3305.

[23] P. G. Bolhuis, D. Chandler, C. Dellago, P. L. Geissler, *Annual Review of Physical Chemistry* **2002**, *53*, 291–318.

[24] R. Czerminski, R. Elber, *Journal of Chemical Physics* **1990**, *92*, 5580–5601.

[25] J. K. W. Jonsson H., Mills G., *Nudged elastic band method for finding minimum energy paths of transitions. In Classical and Quantum Dynamics in Condensed Phase Simulations - Proceedings of the International School of Physics*, World Scientific Publishing Co. Pte. Ltd., Singapore, **1998**.

[26] J. Nocedal, *Mathematics of Computation* **1980**, *35*, 773–782.

[27] D. C. Liu, J. Nocedal, *Mathematical programming* **1989**, *45*, 503–528.

[28] D. F. Shanno, *Mathematics of computation* **1970**, *24*, 647–656.

[29] C. G. Broyden, *IMA Journal of Applied Mathematics* **1970**, *6*, 76–90.

[30] C. G. Broyden, *IMA Journal of Applied Mathematics* **1970**, *6*, 222–231.

[31] R. Fletcher, *The computer journal* **1970**, *13*, 317–322.

[32] D. Goldfarb, *Mathematics of computation* **1970**, *24*, 23–26.

[33] G. Henkelman, B. P. Uberuaga, H. Jonsson, *Journal of Chemical Physics* **2000**, *113*, 9901–9904.

[34] S. A. Trygubenko, D. J. Wales, *The Journal of Chemical Physics* **2004**, *120*, 7820–7820.

[35] S. A. Trygubenko, D. J. Wales, *The Journal of chemical physics* **2004**, *120*, 2082–2094.

[36] M. V. Smoluchowski, *Annalen der Physik* **1916**, *353*, 1103–1112.

[37] M. Berkowitz, J. Morgan, J. McCammon, S. Northrup, *The Journal of chemical physics* **1983**, *79*, 5563–5565.

[38] R. Crehuet, M. J. Field, *The Journal of chemical physics* **2003**, *118*, 9563–9571.

[39] W. Damm, A. Frontera, J. Tirado–Rives, W. L. Jorgensen, J. T. Rives, *Journal of Computational Chemistry* **1997**, *18*, 1955–1970.

[40] W. Damm, T. A. Halgren, R. B. Murphy, A. M. Smondyrev, R. A. Friesner, W. L. Jorgensen, *Abstr. Pap. Am. Chem. S.* **2002**, *224*, 009–COMP.

[41] J. Tiradorives, W. L. Jorgensen, *Abstr. Pap. Am. Chem. S.* **1992**, *204*, 43–COMP.

[42] W. L. Jorgensen, D. S. Maxwell, J. TiradoRives, *Journal of the American Chemical Society* **1996**, *118*, 11225–11236.

[43] C. Grebner, L. P. Pason, B. Engels, *Journal of Computational Chemistry* **2013**, *34*, 1810–1818.

[44] W. Kabsch, *Acta Crystallographica Section A* **1978**, *34*, 827–828.

[45] C. E. Kundrot, J. W. Ponder, F. M. Richards, *Journal of Computational Chemistry* **1991**, *12*, 402–409.

[46] R. V. Pappu, R. K. Hart, J. W. Ponder, *Journal of Physical Chemistry B* **1998**, *102*, 9725–9742.

[47] J. W. Ponder, F. M. Richards, *Journal of Computational Chemistry* **1987**, *8*, 1016–1024.

[48] P. Y. Ren, J. W. Ponder, *Journal of Physical Chemistry B* **2003**, *107*, 5933–5947.

[49] W. Humphrey, A. Dalke, K. Schulten, *Journal of Molecular Graphics & Modelling* **1996**, *14*, 33–38.

[50] J. J. P. Stewart, *MOPAC2012*, of *Stewart Computational Chemistry*, Colorado Springs, CO, USA, **2012**.

[51] M. J. S. Dewar, E. G. Zoebisch, E. F. Healy, J. J. P. Stewart, *Journal of the American Chemical Society* **1985**, *107*, 3902–3909.

[52] J. J. P. Stewart, *Journal of Molecular Modeling* **2007**, *13*, 1173–1213.

[53] J. Rezac, J. Fanfrlik, D. Salahub, P. Hobza, *Journal of Chemical Theory and Computation* **2009**, *5*, 1749–1760.

[54] M. Korth, M. Pitonak, J. Rezac, P. Hobza, *Journal of Chemical Theory and Computation* **2010**, *6*, 344–352.

[55] P. A. M. Dirac, *Proc. Royal Soc. A* **1929**, *123*, 714–733.

[56] J. C. Slater, *Physical Review* **1951**, *81*, 385–390.

[57] A. D. Becke, *Physical Review A* **1988**, *38*, 3098–3100.

[58] A. D. Becke, *Journal of Chemical Physics* **1993**, *98*, 5648–5652.

[59] C. T. Lee, W. T. Yang, R. G. Parr, *Physical Review B* **1988**, *37*, 785–789.

[60] A. Schafer, C. Huber, R. Ahlrichs, *Journal of Chemical Physics* **1994**, *100*, 5829–5835.

[61] R. Ahlrichs, M. Bar, M. Haser, H. Horn, C. Kolmel, *Chemical Physics Letters* **1989**, *162*, 165–169.

[62] S. Stepanenko, B. Engels, *Journal of Computational Chemistry* **2008**, *29*, 768–780.

[63] S. Stepanenko, B. Engels, *J. Phys. Chem. A* **2009**, *113*, 11699–705.

[64] C. Grebner, J. Becker, S. Stepanenko, B. Engels, *Journal of Computational Chemistry* **2011**, *32*, 2245–2253.

[65] C. Grebner, J. Kaestner, W. Thiel, B. Engels, *Journal of Chemical Theory and Computation* **2013**, *9*, 814–821.

[66] K. Fukui, *The Journal of Physical Chemistry* **1970**, *74*, 4161–4163.

[67] H. Abdi, L. J. Williams, *Wiley Interdisciplinary Reviews: Computational Statistics* **2010**, *2*, 433–459.

[68] J. Erdmannsdoerfer, Bachelor thesis, University of Wuerzburg, **2014**.

[69] M. A. Spackman, *Chemical Physics Letters* **2006**, *418*, 158–162.

[70] D. Bellinger, Master's thesis, University of Wuerzburg, **2012**.

[71] C. Grebner, J. Becker, D. Weber, D. Bellinger, M. Tafipolski, C. Brueckner, B. Engels, *Journal of Computational Chemistry* **2014**, *35*, 1801–1807.

[72] M. Tafipolsky, B. Engels, *Journal of Chemical Theory and Computation* **2011**, *7*, 1791–1803.

[73] H. Takeuchi, *Journal of Physical Chemistry A* **2012**, *116*, 10172–10181.

[74] H. Takeuchi, *Journal of Chemical Information and Modeling* **2007**, *47*, 104–109.

[75] S. Grimme, *Journal of Computational Chemistry* **2006**, *27*, 1787–1799.

[76] S. Grimme, S. Ehrlich, L. Goerigk, *Journal of Computational Chemistry* **2011**, *32*, 1456–1465.

[77] J. A. Pople, M. Headgordon, K. Raghavachari, *Journal of Chemical Physics* **1987**, *87*, 5968–5975.

[78] M. O. Sinnokrot, E. F. Valeev, C. D. Sherrill, *Journal of the American Chemical Society* **2002**, *124*, 10887–10893.

[79] M. O. Sinnokrot, C. D. Sherrill, *Journal of Physical Chemistry A* **2004**, *108*, 10200–10207.

[80] J. G. Hill, J. A. Platts, H.-J. Werner, *Physical Chemistry Chemical Physics* **2006**, *8*, 4072–4078.

[81] O. Bludsky, M. Rubes, P. Soldan, P. Nachtigall, *Journal of Chemical Physics* **2008**, *128*, 114102.

[82] J. P. Perdew, W. Yue, *Physical Review B* **1986**, *33*, 8800–8802.

[83] J. P. Perdew, K. Burke, M. Ernzerhof, *Physical Review Letters* **1996**, *77*, 3865–3868.

[84] J. P. Perdew, K. Burke, M. Ernzerhof, *Physical Review Letters* **1997**, *78*, 1396–1396.

[85] T. H. Dunning Jr, *The Journal of chemical physics* **1989**, *90*, 1007–1023.

[86] D. E. Woon, T. H. Dunning Jr, *The Journal of chemical physics* **1994**, *100*, 2975–2988.

[87] S. Nose, *Journal of Chemical Physics* **1984**, *81*, 511–519.

[88] T. P. Tauer, C. D. Sherrill, *Journal of Physical Chemistry A* **2005**, *109*, 10475–10478.

[89] T. Morimoto, H. Uno, H. Furuta, *Angewandte Chemie-international Edition* **2007**, *46*, 3672–3675.

[90] H. Uno, Y. Fumoto, K. Inoue, N. Ono, *Tetrahedron* **2003**, *59*, PII S0040–4020(02)01589–2.

[91] J. E. Lee, V. Stepanenko, J. Yang, H. Yoo, F. Schlosser, D. Bellinger, B. Engels, I. G. Scheblykin, F. Wrthner, D. Kim, *Acs Nano* **2013**, *7*, 5064–5076.

[92] M. M. Francl, W. J. Pietro, W. J. Hehre, J. S. Binkley, M. S. Gordon, D. J. Defrees, J. A. Pople, *Journal of Chemical Physics* **1982**, *77*, 3654–3665.

[93] W. J. Hehre, Ditchfie.R, J. A. Pople, *Journal of Chemical Physics* **1972**, *56*, 2257–&.

[94] M. S. Gordon, *Chemical Physics Letters* **1980**, *76*, 163–168.

[95] M. J. Frisch, J. A. Pople, J. S. Binkley, *Journal of Chemical Physics* **1984**, *80*, 3265–3269.

[96] N. L. Allinger, *Journal of the American Chemical Society* **1977**, *99*, 8127–8134.

[97] Hypercube Inc., Waterloo, Ontario, Canada, *HyperChem Manual*, **1994**.

[98] W. D. Cornell, P. Cieplak, C. I. Bayly, I. R. Gould, K. M. Merz, D. M. Ferguson, D. C. Spellmeyer, T. Fox, J. W. Caldwell, P. A. Kollman, *Journal of the American Chemical Society* **1995**, *117*, 5179–5197.

[99] H. Weinstein, R. Pauncz, M. Cohen, *Advances in atomic and molecular physics* **1971**, *7*, 97–140.

[100] A. Warshel, *Computer modelling of chemical reactions in enzymes and solutions*, Wiley, **2013**.

[101] M. Eichinger, P. Tavan, J. Hutter, M. Parrinello, *The Journal of chemical physics* **1999**, *110*, 10452–10467.

[102] U. F. Röhrig, I. Frank, J. Hutter, A. Laio, J. VandeVondele, U. Rothlisberger, *ChemPhysChem* **2003**, *4*, 1177–1182.

[103] H. Lin, D. G. Truhlar, *Theoretical Chemistry Accounts* **2007**, *117*, 185–199.

[104] K. Sneskov, E. Matito, J. Kongsted, O. Christiansen, *Journal of chemical theory and computation* **2010**, *6*, 839–850.

[105] J. Neugebauer, C. Curutchet, A. Munoz-Losa, B. Mennucci, *Journal of Chemical Theory and Computation* **2010**, *6*, 1843–1851.

[106] S. Miertuš, E. Scrocco, J. Tomasi, *Chemical Physics* **1981**, *55*, 117–129.

[107] C. J. Cramer, D. G. Truhlar, *Chemical Reviews* **1999**, *99*, 2161–2200.

[108] J. Tomasi, B. Mennucci, R. Cammi, *Chemical Reviews* **2005**, *105*, 2999–3093.

[109] J. Tomasi, *Wiley Interdisciplinary Reviews: Computational Molecular Science* **2011**, *1*, 855–867.

[110] A. Klamt, *Wiley Interdisciplinary Reviews: Computational Molecular Science* **2011**, *1*, 699–709.

[111] B. Lunkenheimer, A. Koehn, *Journal of Chemical Theory and Computation* **2013**, *9*, 977–994.

[112] M. Caricato, B. Mennucci, J. Tomasi, F. Ingrosso, R. Cammi, S. Corni, G. Scalmani, *The Journal of chemical physics* **2006**, *124*, 124520.

[113] A. Klamt, G. Schuurmann, *Journal of the Chemical Society-Perkin Transactions 2* **1993**, 799–805.

[114] A. Schaefer, A. Klamt, D. Sattel, J. C. W. Lohrenz, F. Eckert, *Physical Chemistry Chemical Physics* **2000**, *2*, 2187–2193.

[115] S. E. Shaheen, G. E. Jabbour, B. Kippelen, N. Peyghambarian, J. D. Anderson, S. R. Marder, N. R. Armstrong, E. Bellmann, R. H. Grubbs, *Applied Physics Letters* **1999**, *74*, 3212–3214.

[116] C. W. Tang, *Applied Physics Letters* **1986**, *48*, 183–185.

[117] Z. N. Bao, *Advanced Materials* **2000**, *12*, 227–230.

[118] A. Damjanovic, I. Kosztin, U. Kleinekathofer, K. Schulten, *Physical Review E* **2002**, *65*.

[119] J. Vura-Weis, M. A. Ratner, M. R. Wasielewski, *Journal of the American Chemical Society* **2010**, *132*, 1738–1739.

[120] R. F. Fink, J. Seibt, V. Engel, M. Renz, M. Kaupp, S. Lochbrunner, H. M. Zhao, J. Pfister, F. Würthner, B. Engels, *Journal of the American Chemical Society* **2008**, *130*, 12858–12859.

[121] H. M. Zhao, J. Pfister, V. Settels, M. Renz, M. Kaupp, V. C. Dehm, F. Würthner, R. F. Fink, B. Engels, *Journal of the American Chemical Society* **2009**, *131*, 15660–15668.

[122] J. Cornil, D. Beljonne, J. P. Calbert, J. L. Bredas, *Advanced Materials* **2001**, *13*, 1053–1067.

[123] C. Hippius, I. H. M. van Stokkum, E. Zangrando, R. M. Williams, M. Wykes, D. Beljonne, F. Würthner, *Journal of Physical Chemistry C* **2008**, *112*, 14626–14638.

[124] A. Burquel, V. Lemaur, D. Beljonne, R. Lazzaroni, J. Cornil, *Journal of Physical Chemistry A* **2006**, *110*, 3447–3453.

[125] A. Warshel, M. Karplus, *Journal of the American Chemical Society* **1972**, *94*, 5612–5625.

[126] A. Warshel, M. Levitt, *Journal of Molecular Biology* **1976**, *103*, 227 – 249.

[127] V. Bulovic, P. E. Burrows, S. R. Forrest, J. A. Cronin, M. E. Thompson, *Chemical Physics* **1996**, *210*, 1–12.

[128] S. R. Forrest, *Chemical Reviews* **1997**, *97*, 1793–1896.

[129] F. F. So, S. R. Forrest, *Physical Review Letters* **1991**, *66*, 2649–2652.

[130] R. Scholz, A. Y. Kobitski, I. Vragovic, H. P. Wagner, D. R. T. Zahn, *Organic Electronics* **2004**, *5*, 99–105.

[131] G. Mazur, P. Petelenz, M. Slawik, *Journal of Chemical Physics* **2003**, *118*, 1423–1432.

[132] Z. Shen, S. R. Forrest, *Physical Review B* **1997**, *55*, 10578.

[133] Z. G. Soos, M. H. Hennessy, G. Wen, *Chemical Physics* **1998**, *227*, 19–32.

[134] M. Andrzejak, G. Mazur, P. Petelenz, *Journal of Molecular Structure: THEOCHEM* **2000**, *527*, 91–102.

[135] M. H. Hennessy, Z. G. Soos, R. A. Pascal, A. Girlando, *Chemical Physics* **1999**, *245*, 199–212.

[136] D. Veldman, S. M. A. Chopin, S. C. J. Meskers, R. A. J. Janssen, *Journal of Physical Chemistry A* **2008**, *112*, 8617–8632.

[137] V. Settels, W. Liu, J. Pflaum, R. F. Fink, B. Engels, *Journal of Computational Chemistry* **2012**, *33*, 1544–1553.

[138] W. Liu, V. Settels, P. H. P. Harbach, A. Dreuw, R. F. Fink, B. Engels, *Journal of Computational Chemistry* **2011**, *32*, 1971–1981.

[139] H. Heinz, U. W. Suter, E. Leontidis, *Journal of the American Chemical Society* **2001**, *123*, 11229–11236.

[140] A. Davydov, *Theory of absorption spectra of molecular crystals*, Department of Chemistry, University of California, **1949**.

[141] J. D. Dill, J. A. Pople, *The Journal of Chemical Physics* **1975**, *62*, 2921–2923.

[142] V. A. Rassolov, J. A. Pople, M. A. Ratner, T. L. Windus, *The Journal of chemical physics* **1998**, *109*, 1223–1229.

[143] C. Curutchet, A. Munoz-Losa, S. Monti, J. Kongsted, G. D. Scholes, B. Mennucci, *Journal of Chemical Theory and Computation* **2009**, *5*, 1838–1848.

[144] J.-D. Chai, M. Head-Gordon, *Physical Chemistry Chemical Physics* **2008**, *10*, 6615–6620.

[145] C. Brueckner, B. Engels, *The Journal of Physical Chemistry A* **2015**, *119*, 12876–12891.

[146] O. Christiansen, H. Koch, P. Jørgensen, *Chemical Physics Letters* **1995**, *243*, 409 – 418.

[147] A. B. Trofimov, J. Schirmer, *Journal of Physics B-Atomic Molecular and Optical Physics* **1995**, *28*, 2299–2324.

[148] K. Andersson, P.-Å. Malmqvist, B. O. Roos, *The Journal of chemical physics* **1992**, *96*, 1218–1226.

[149] D. Bellinger, V. Settels, W. L. Liu, R. F. Fink, B. Engels, *Journal of Computational Chemistry* **2016**, *37*, 1601–1610.

[150] A. Schaefer, C. Huber, R. Ahlrichs, *Journal of Chemical Physics* **1994**, *100*, 5829–5835.

[151] K. Eichkorn, F. Weigend, O. Treutler, R. Ahlrichs, *Theoretical Chemistry Accounts* **1997**, *97*, 119–124.

[152] S. Grimme, *Journal of Computational Chemistry* **2004**, *25*, 1463–1473.

[153] A. Klamt, F. Eckert, *Fluid Phase Equilibria* **2000**, *172*, 43–72.

[154] S. Sinnecker, A. Rajendran, A. Klamt, M. Diedenhofen, F. Neese, *Journal of Physical Chemistry A* **2006**, *110*, 2235–2245.

[155] A. Klamt, *Wiley Interdisciplinary Reviews-Computational Molecular Science* **2011**, *1*, 699–709.

[156] B. Mennucci, R. Cammi, J. Tomasi, *Journal of Chemical Physics* **1998**, *109*, 2798–2807.

[157] E. Cances, B. Mennucci, J. Tomasi, *Journal of Chemical Physics* **1997**, *107*, 3032–3041.

[158] B. Mennucci, E. Cances, J. Tomasi, *Journal of Physical Chemistry B* **1997**, *101*, 10506–10517.

[159] G. Scalmani, M. J. Frisch, B. Mennucci, J. Tomasi, R. Cammi, V. Barone, *Journal of Chemical Physics* **2006**, *124*.

[160] F. Santoro, V. Barone, T. Gustavsson, R. Improta, *Journal of the American Chemical Society* **2006**, *128*, 16312–16322.

[161] K. Yesudas, G. K. Chaitanya, C. Prabhakar, K. Bhanuprakash, V. J. Rao, *Journal of Physical Chemistry A* **2006**, *110*, 11717–11729.

[162] C. E. Crespo-Hernandez, G. Burdzinski, R. Arce, *Journal of Physical Chemistry A* **2008**, *112*, 6313–6319.

[163] C. Curutchet, B. Mennucci, G. D. Scholes, D. Beljonne, *Journal of Physical Chemistry B* **2008**, *112*, 3759–3766.

[164] Y. Liang, R. Zhang, F. Jiang, *Journal of Molecular Structure-Theochem* **2008**, *848*, 1–8.

[165] M. Alvarado-Gonzalez, N. Flores-Holguin, M. Gallo, E. Orrantia-Borunda, D. Glossman-Mitnik, *Journal of Molecular Structure-Theochem* **2010**, *945*, 101–103.

[166] A. Frisch, *Gaussian 03*, Gaussian, **2004**.

[167] A. Schaefer, H. Horn, R. Ahlrichs, *Journal of Chemical Physics* **1992**, *97*, 2571–2577.

[168] N. S. Bayliss, *Journal of Chemical Physics* **1950**, *18*, 292–296.

[169] N. Q. Chako, *J Chem Phys* **1934**, *2*, 644.

[170] A. Schubert, V. Settels, W. Liu, F. Wuerthner, C. Meier, R. F. Fink, S. Schindlbeck, S. Lochbrunner, B. Engels, V. Engel, *Journal of Physical Chemistry Letters* **2013**, *4*, 792–796.

[171] F. Plasser, H. Lischka, *Journal of Chemical Theory and Computation* **2012**, *8*, 2777–2789.

[172] F. Plasser, S. A. Bäppler, M. Wormit, A. Dreuw, *The Journal of Chemical Physics* **2014**, *141*, 024107.

[173] F. Plasser, M. Wormit, A. Dreuw, *The Journal of Chemical Physics* **2014**, *141*, 024106.

[174] V. Settels, A. Schubert, M. Tafipolsky, W. Liu, V. Stehr, A. K. Topczak, J. Pflaum, C. Deibel, V. Engel, R. F. Fink, B. Engels, *Journal of the American Chemical Society* **2012**, *136*, 9327–9337.

[175] J. Lagarias, *Bulletin of the American Mathematical Society* **2013**, *50*, 527–628.

[176] K. Tojo, J. Mizuguchi, *Zeitschrift für Kristallographie-New Crystal Structures* **2002**, *217*, 253–254.

[177] S. Metz, J. Kästner, A. A. Sokol, T. W. Keal, P. Sherwood, *Wiley Interdisciplinary Reviews: Computational Molecular Science* **2014**, *4*, 101–110.

[178] *ChemShell, a Computational Chemistry Shell*. `www.chemshell.org`.

[179] P. Sherwood, A. H. de Vries, M. F. Guest, G. Schreckenbach, C. R. A. Catlow, S. A. French, A. A. Sokol, S. T. Bromley, W. Thiel, A. J. Turner, et al., *Journal of Molecular Structure: THEOCHEM* **2003**, *632*, 1–28.

[180] W. Smith, I. T. Todorov, *Molecular Simulation* **2006**, *32*, 935–943.

[181] J. M. Wang, R. M. Wolf, J. W. Caldwell, P. A. Kollman, D. A. Case, *Journal of Computational Chemistry* **2004**, *25*, 1157–1174.

[182] J. Wang, W. Wang, P. A. Kollman, D. A. Case, *Journal of molecular graphics and modelling* **2006**, *25*, 247–260.

[183] P. M. Gill, B. G. Johnson, J. A. Pople, M. J. Frisch, *Chemical Physics Letters* **1992**, *197*, 499–505.

[184] P. C. Hariharan, J. A. Pople, *Theoretica chimica acta* **1973**, *28*, 213–222.

[185] J. Ridley, M. Zerner, *Theoretica chimica acta* **1973**, *32*, 111–134.

[186] M. C. Zerner, G. H. Loew, R. F. Kirchner, U. T. Mueller-Westerhoff, *Journal of the American Chemical Society* **1980**, *102*, 589–599.

[187] A. D. Bacon, M. C. Zerner, *Theoretica chimica acta* **1979**, *53*, 21–54.

[188] M. A. Thompson, M. C. Zerner, *Journal of the American Chemical Society* **1991**, *113*, 8210–8215.

[189] W. P. Anderson, W. D. Edwards, M. C. Zerner, *Inorganic chemistry* **1986**, *25*, 2728–2732.

[190] P. C. De Mello, M. Hehenberger, M. Zernert, *International Journal of Quantum Chemistry* **1982**, *21*, 251–258.

[191] L. K. Hanson, J. Fajer, M. A. Thompson, M. C. Zerner, *Journal of the American Chemical Society* **1987**, *109*, 4728–4730.

[192] M. C. Zerner, *Reviews in computational chemistry* **1991**, *2*, 313–365.

[193] J. E. Ridley, M. C. Zerner, *Theoretica chimica acta* **1976**, *42*, 223–236.

[194] K. Hannewald, V. Stojanović, J. Schellekens, P. Bobbert, G. Kresse, J. Hafner, *Physical Review B* **2004**, *69*, 075211.

[195] G. Nan, X. Yang, L. Wang, Z. Shuai, Y. Zhao, *Physical Review B* **2009**, *79*, 115203.

[196] L. Gisslen, R. Scholz, *Physical Review B* **2009**, *80*, 115309.

[197] M. Hoffmann, K. Schmidt, T. Fritz, T. Hasche, V. M. Agranovich, K. Leo, *Chemical Physics* **2000**, *258*, 73–96.

[198] R. Scholz, A. Y. Kobitski, D. R. T. Zahn, M. Schreiber, *Physical Review B* **2005**, *72*, 245208.

[199] H. Yamagata, J. Norton, E. Hontz, Y. Olivier, D. Beljonne, J.-L. Brédas, R. Silbey, F. Spano, *The Journal of chemical physics* **2011**, *134*, 204703.

[200] V. Gangilenka, L. Titova, L. Smith, H. Wagner, L. DeSilva, L. Gisslén, R. Scholz, *Physical Review B* **2010**, *81*, 155208.

[201] F. C. Spano, H. Yamagata, *The Journal of Physical Chemistry B* **2010**, *115*, 5133–5143.

[202] C. J. Cramer, *Essentials of computational chemistry: theories and models*, John Wiley & Sons, **2013**.

[203] F. C. Spano, *The Journal of chemical physics* **2005**, *122*, 234701.

[204] F. C. Spano, *Chemical physics* **2006**, *325*, 22–35.

[205] C. Didraga, J. A. Klugkist, J. Knoester, *The Journal of Physical Chemistry B* **2002**, *106*, 11474–11486.

[206] C. Brüning, K. Renziehausen, V. Engel, *The Journal of chemical physics* **2013**, *139*, 054303.

[207] M. Alonso, M. Garriga, N. Karl, J. Ossó, F. Schreiber, *Organic electronics* **2002**, *3*, 23–31.

[208] E. Engel, M. Koschorreck, K. Leo, M. Hoffmann, *Physical review letters* **2005**, *95*, 157403.

[209] G. Karlsson, M. C. Zerner, *International Journal of Quantum Chemistry* **1973**, *7*, 35–49.

[210] J. D. Da Motta Neto, M. C. Zerner, *International Journal of Quantum Chemistry* **2001**, *81*, 187–201.